

MULTISCALE COMPUTATIONAL ANALYSIS AND MODELING OF
THERMOCHEMICAL NONEQUILIBRIUM FLOW

A Dissertation

Submitted to the Faculty

of

Purdue University

by

Han Luo

In Partial Fulfillment of the

Requirements for the Degree

of

Doctor of Philosophy

August 2020

Purdue University

West Lafayette, Indiana

**THE PURDUE UNIVERSITY GRADUATE SCHOOL
STATEMENT OF DISSERTATION APPROVAL**

Dr. Alina Alexeenko, Co-chair

School of Aeronautics and Astronautics

Dr. Sergey O. Macheret, Co-chair

School of Aeronautics and Astronautics

Dr. Jonathan Poggie

School of Aeronautics and Astronautics

Dr. Sally P. Bane

School of Aeronautics and Astronautics

Approved by:

Dr. Gregory A. Blaisdell

Thesis Form Head of the School Graduate Program

Dedicated to my beloved parents Chen, Guimei, Luo, Hongwei and my families for their silent love, endless support, and sacrifices for my growth.

ACKNOWLEDGMENTS

Many people have contributed directly or indirectly to this thesis. First and foremost, I would like to acknowledge my advisors, Prof. Alina Alexeenko and Prof. Sergey Macheret. Prof. Alexeenko introduced me to the field of particle-based simulation methods and rarefied gas dynamics. She gave me the opportunity to join her group and tried her best to find funding support. The freedom she gave me on the selection of research topics allowed me to have an enjoyable academic life. The academic experiences she shared greatly strengthened my abilities in team working and big picture thinking. Prof. Macheret taught me a lot about thermal nonequilibrium gas dynamics and plasma physics. Without his initial idea of modeling nonequilibrium dissociation reactions, this thesis would not exist today. I was always amazed by his wisdom when discussing problems with him. I greatly appreciate his continuous encouragement and guidance on my academic and professional life. I thank my committee members, Prof. Jonathan Poggie and Prof. Sally Bane for their insightful suggestions and comments on my work. I am also grateful to my friends and colleagues at Purdue. Throughout my pursue of Ph.D. degree, I have obtained help from: Aaron Pikus, Aizhan Ibrayeva, Andrei Khomenko, Andrew Weaver, Andrew Strongrich, Anthony Cofer, Arunkumar Chinnappan, Bill O'Neill, Cem Pekardan, Devon Parkos, Gayathri Shivkumar, Israel Sebastião, Kate Fowee, Marat Kulakmetov, Nadia Numa, Nirajan Adhikari , Sashank Jaiswal, Siva Tholeti, Petr Kazarin, Tianfang Xie, Tong Zhu, Tugba Piskin, Vladlen Podolsky and Yanwen Chen. I would deliberately express my appreciation to Marat Kulakmetov, Israel Sebastião, and Devon Parkos for their support and help to my research and life.

I owe my deepest thanks to my parents and families. It is their silent love and countless support that made me today and got me the opportunity to be educated at Purdue.

TABLE OF CONTENTS

	Page
LIST OF TABLES	vii
LIST OF FIGURES	viii
SYMBOLS	xii
ABBREVIATIONS	xiv
ABSTRACT	xv
1 INTRODUCTION	1
1.1 Thermochemical Nonequilibrium	1
1.2 State of the Art Study	3
1.3 Open Questions and Challenges	10
1.4 Goals and Objectives of the Dissertation	13
2 THERMAL NONEQUILIBRIUM TRANSPORT PROPERTIES	15
2.1 Introduction	15
2.2 Transport Properties with Thermal Nonequilibrium	17
2.3 First-Principle Calculations of Transport Properties	25
2.3.1 Quasi-classical Trajectory Method	25
2.3.2 Method of Computing Transport Properties	27
2.3.3 Collision Integrals for N ₂ -O	33
2.3.4 Scattering Law for N ₂ -O	41
2.4 Summary	45
3 DEVELOPMENT OF NONEQUILIBRIUM DISSOCIATION MODEL	47
3.1 Motivation and Background	47
3.2 Macheret-Fridman Theory of Dissociation	49
3.3 Macheret-Fridman Model for CFD	56
3.3.1 Derivation of the Model	56
3.3.2 Validation of the Model	60
3.3.3 Simulation of O ₂ Reacting Shock	68
3.3.4 Summary	71
3.4 Macheret-Fridman Model for DSMC	74
3.4.1 Introduction	74
3.4.2 Validation of the Model	75
3.4.2.1 Vibrational State-Specific Rates	77
3.4.2.2 Nonequilibrium Factors	80

	Page
3.4.2.3	Vibrational Energy Consumption in Dissociation . . . 88
3.4.2.4	Equilibrium Dissociation Rates 91
3.4.3	Improved Modeling of Total Collision Cross Sections 95
3.4.3.1	QCT-Based Collision Model 97
3.4.3.2	Collision Model Based on Exponential Potential . . . 100
3.4.4	Improved Modeling of Vibrational Phase Angle 104
3.4.5	Validation of the Improved Model 107
3.4.5.1	Vibrational State-Specific Rates 108
3.4.5.2	Equilibrium Dissociation Rates 110
3.4.6	Simulation of O ₂ Reacting Shock 113
3.4.7	Summary 121
3.5	Summary 123
4	CONCLUSIONS 124
4.1	Concluding Remarks 124
4.2	Future Work 125
REFERENCES 130
VITA 141

LIST OF TABLES

Table	Page
1.1 Summary of <i>ab initio</i> PES calculations for N ₂ O	9
1.2 Existing QCT calculation results	10
3.1 Equilibrium chemical reaction rates	61
3.2 Freestream conditions of O ₂ reacting shock	69
3.3 Summary of simulation parameters	69
3.4 VHS parameters with $T_{ref} = 273$ K	76
3.5 References of equilibrium dissociation rates	92
3.6 Parameters of exponential potential	101
3.7 Parameters of Morse potential	106
3.8 Freestream conditions of O ₂ reacting shock	114
4.1 Comparison of numerical parameters used in DS1V and SPARTA	127

LIST OF FIGURES

Figure	Page
1.1 Comparison of total integral cross sections for $\text{H} + \text{HeH}^+(v=0, j=0) \rightarrow \text{He} + \text{H}_2^+$ reaction obtained with different dynamical methods. In the inset, a comparison between QCT and QM-CC normalized computational cost estimations is given [42]	7
1.2 Convergence of different post Hartree-Fock methods	8
1.3 N_2O schematic correlation diagram, energies are in electron volt [64]	11
1.4 Comparison of adiabatic QCT calculated VT relaxation time for N_2+O with experimental measurements	12
2.1 Comparison of simulation domains between DSMC and CFD	18
2.2 Knudsen number calculated from CFD	19
2.3 Horizontal velocity profiles at different locations near the wall; u_e is the velocity of external flow.	19
2.4 Normalized translational temperature profiles at different locations near the wall; T_w is the wall temperature and T_e is the free stream temperature.	20
2.5 Comparison of pressure coefficient between DSMC and CFD	21
2.6 Comparison of Stanton number between DSMC and CFD	21
2.7 Translational and vibrational temperature calculated by DSMC	22
2.8 Viscosity and temperature profiles calculated by DSMC	23
2.9 Comparison of viscosity between DSMC and CFD	24
2.10 Coordinate system for an atom-diatom collision	26
2.11 One dimensional cut of PESs ($\angle\text{NNO} = 180^\circ$) with different distance between N_2 and O . $r(\text{N-N})$ is fixed at different distance, (a) $r(\text{N-N}) = r_e = 1.0977 \text{ \AA}$; (b) $r(\text{N-N}) = 2 \text{ \AA}$	31
2.12 Examples of trajectories for atomic oxygen colliding with nitrogen molecule with different initial vibrational level on $1^3\text{A}''$ PES	33
2.13 Diffusion and viscosity type collision integrals for $1^3\text{A}''$ state	35
2.14 Diffusion and viscosity type collision integrals for $1^3\text{A}'$ state	35

Figure	Page
2.15 Diffusion and viscosity type collision integrals for $1^1A'$ state	36
2.16 Collision integrals at different vibrational temperature for $1^3A''$ state. The error bar is smaller than the size of symbols.	37
2.17 Collision integrals at different vibrational temperature for $1^3A'$ state. The error bar is smaller than the size of symbols.	37
2.18 Collision integrals at different vibrational temperature for $1^1A'$ state. The error bar is smaller than the size of symbols.	38
2.19 Comparison of the mean collision integral for different models	40
2.20 Comparison of the scattering angles χ predicted by different collision models	43
2.21 Normalized probability density function of scattering angles	44
2.22 Comparison of the scattering law between QCT data (symbols) and the fitted model (lines)	44
2.23 Comparison of collision integrals calculated with the proposed model to QCT results	45
3.1 Qualitative description of energy distribution function $f(E)$ and reaction cross sections $\sigma(E)$	50
3.2 Collision geometries: (a) diatom-atom; (b) diatom-diatom.	51
3.3 Model potential energy curve	54
3.4 Nonequilibrium factor for $N_2 + O \rightarrow N + N + O$	63
3.5 Nonequilibrium factor for $N_2 + N \rightarrow N + N + N$	64
3.6 Nonequilibrium factor for $O_2 + O \rightarrow O + O + O$	65
3.7 Nonequilibrium factor for $N_2 + N_2 \rightarrow N + N + N_2$	66
3.8 Nonequilibrium factor for $O_2 + O_2 \rightarrow O + O + O_2$	67
3.9 Chemical reaction rates for reactions in pure O_2	70
3.10 Vibrational-translational relaxation time of O_2 -O and O_2 - O_2	70
3.11 Properties of gas behind the shock front for shock with Mach 13.4	72
3.12 Temperature profile for shock with Mach 11.9	73
3.13 Comparison of vibrational state-specific rates calculated by QCT method and MF-DSMC model for atom-diatom collision. MF-DSMC rates for N_2+N and O_2+O are scaled.	79

Figure	Page
3.14 Comparison of vibrational state-specific rates calculated by QCT method and MF-DSMC model for diatom-diatom collisions. MF-DSMC rates for O_2+O_2 are scaled.	80
3.15 Probability density functions of internuclear distance for N_2 molecule at different values of vibrational energy	81
3.16 Nonequilibrium factor for $N_2 + N \rightarrow N + N + N$	82
3.17 Nonequilibrium factor for $O_2 + O \rightarrow O + O + O$	83
3.18 Nonequilibrium factor for $N_2 + O \rightarrow N + N + O$	84
3.19 Nonequilibrium factor for $N_2 + N_2 \rightarrow N + N + N_2$	85
3.20 Nonequilibrium factor for $O_2 + O_2 \rightarrow O + O + O_2$	86
3.21 Nonequilibrium factor for $O_2 + N_2 \rightarrow O + O + N_2$	87
3.22 Nonequilibrium factor for $N_2 + O_2 \rightarrow N + N + O_2$	88
3.23 Comparison of the average vibrational energy removed by dissociation reactions for atom-diatom collisions. Red lines for thermally equilibrium conditions $T = T_v$; other lines for vibrationally nonequilibrium conditions $T \neq T_v$	90
3.24 Comparison of the average vibrational energy removed by dissociation reactions for diatom-diatom collisions. Red lines for thermally equilibrium conditions $T = T_v$; other lines for vibrationally nonequilibrium conditions $T \neq T_v$	91
3.25 Comparison of diatom-diatom equilibrium dissociation rates	93
3.26 Comparison of diatom-atom equilibrium dissociation rates (QCT and DMS calculated rates for O_2+O_2 are not multiplied by the electronic degeneracy factor $\eta = 16/3$)	94
3.27 Comparison of QCT calculated total cross sections for different vibrational states and rotational states	97
3.28 Comparison of fitted total cross sections and QCT data	98
3.29 Comparison of equilibrium dissociation rates for N_2 dissociation in collisions with atomic oxygen predicted by MF-DSMC model with VHS or QCT-based collision model	99
3.30 Comparison of scattering angles calculated with different approaches for N_2 -O collisions. QCT results of N_2 ground vibrational and rotational state are shown.	103

Figure	Page
3.31 Time variation of vibrational phase angle during the period of vibration for O ₂ molecule	107
3.32 Comparison of vibrational state-specific rates calculated by QCT method and MF-DSMC model for N ₂ +N, N ₂ +O, O ₂ +N ₂ , N ₂ +O ₂ , and NO+N ₂ dissociations. MF-DSMC rates for N ₂ +N and N ₂ +O are scaled.	109
3.33 Comparison of diatom-atom equilibrium dissociation rates for N ₂ +N, O ₂ +O, and N ₂ +O colliding pairs.	112
3.34 Comparison of diatom-diatom equilibrium dissociation rates for N ₂ +N ₂ , O ₂ +O ₂ , O ₂ +N ₂ and N ₂ +O ₂ , and NO+N ₂ colliding pairs. The first molecular symbol indicates the dissociating molecule.	113
3.35 Collision procedure of the DSMC code	114
3.36 Comparison of equilibrium dissociation rate for O ₂ -O predicted by MF-DSMC-AHO model combined with calibrated total cross sections with experimental data and QCT calculations	115
3.37 Comparison of the temperature profile for the two cases; Solid lines for translational temperature; dashed lines for vibrational temperature . . .	117
3.38 Comparison of the density profile for the two cases	118
3.39 Comparison of the O ₂ mass fraction for the two cases	118
3.40 Vibrational energy populations of O ₂ molecules at different locations across the shock wave for the two cases. Boltzmann distributions characterized by local T_v are shown as dashed lines for MF-DSMC model and solid lines for MF-DSMC-AHO model.	119
4.1 Simulation of the Mach=13.5 O ₂ reacting shock with MF-DSMC-AHO model in SPARTA	127
4.2 Comparison of the shock profile predicted by SPARTA and DS1V for the Mach=13.5 O ₂ reacting shock	128
4.3 Temperatures and mole fractions of 14 km/s O ₂ reacting shock	129

SYMBOLS

b	Impact parameter
$c(O_2)$	Mass fraction of O_2
d_{ref}	Reference diameter
χ	Scattering angle
E_r	Rotational energy
E_{rv}	Rovibrational energy
E_v	Vibrational energy
$E_{v,rem}$	Average vibrational energy removed by dissociation
f	Distribution function
g	Degeneracy
\hbar	Reduced Planck constant
H	Hamiltonian
J	Rotational level
k_b	Boltzmann constant
k_{eq}	Equilibrium reaction rate
$k(T, E_v)$	Vibrational state-specific reaction rate
$k(T, T_v)$	Two-temperature reaction rate
$k(T, T_r, T_v)$	Three-temperature reaction rate
Kn	Knudsen number
Ma	Mach number
m_r	Reduced mass
$\Omega^{(1,1)*}$	Reduced collision integrals of diffusivity
$\Omega^{(2,2)*}$	Reduced collision integrals of viscosity
$\Omega^{(1,1)}$	Collision integrals of diffusivity
$\Omega^{(2,2)}$	Collision integrals of viscosity

ψ	Total wave function
$\psi_{el}, \psi_{vib}, \psi_{rot}$	Electronic, vibrational, and rotational wave function
$Q^{(1)}$	Momentum cross sections
$Q^{(2)}$	Viscous cross sections
σ_{coll}, σ_T	Total collision cross sections
τ_{coll}	Mean collision time
τ_{reac}	Characteristic time of reaction
τ_{rot}	Rotational relaxation time
τ_{vib}	Vibrational relaxation time
T	Temperature
T_r	Rotational temperature
T_t	Translational temperature
T_v	Vibrational temperature
v	Vibrational level
V_r	Relative velocity of collision
Z_R	Rotational relaxation number
Z_V	Vibrational relaxation number
Z	Nonequilibrium factor

ABBREVIATIONS

CFD	Computational fluid dynamics
DSMC	Direct simulation Monte Carlo
LB	Larsen-Borgnakke model
L-J	Lennard-Jones
MF	Macheret-Fridman
PEC	Potential energy curve
PES	Potential energy surface
QCT	Quasi-classical trajectory
QK	Quantum kinetics model
QM-CC	Quantum mechanical closed-coupling scattering
RT	Rotational-translational
TCE	Total collision energy model
VE	Vibrational-electronic
VFD	Vibrationally-favored dissociation model
VHS	Variable hard sphere model
VT	Vibrational-translational
VSS	Variable soft sphere model
VV	Vibrational-vibrational

ABSTRACT

Luo, Han Ph.D., Purdue University, August 2020. Multiscale Computational Analysis and Modeling of Thermochemical Nonequilibrium Flow. Major Professors: Alina Alexeenko and Sergey O. Macheret.

Thermochemical nonequilibrium widely exists in supersonic combustion, cold plasma and hypersonic flight. The effect can influence heat transfer, surface ablation and aerodynamic loads. One distinct feature of it is the coupling between internal energy excitation and chemical reactions, particularly the vibration-dissociation coupling. The widely used models are empirical and calibrated based on limited experimental data. Advances in theories and computational power have made the first-principle calculation of thermal nonequilibrium reaction rates by methods like quasi-classical trajectory (QCT) almost a routine today. However, the approach is limited by the uncertainties and availability of potential energy surfaces. To the best of our knowledge, there is no study of thermal nonequilibrium transport properties with this approach. Most importantly, non-trivial effort is required to process the QCT data and implement it in flow simulation methods. In this context, the first part of this work establishes the approach to compute transport properties by the QCT method and studies the influence of thermal nonequilibrium on transport properties for N_2 -O molecules. The preponderance of the work is the second part, a comprehensive study of the development of a new thermal nonequilibrium reaction model based on reasonable assumptions and approximations. The new model is as convenient as empirical models. By validating against recent QCT data and experimental results, we found the new model can predict nonequilibrium characteristics of dissociation reactions with nearly the same accuracy as QCT calculations do. In general, the results show the potential of the new model to be used as the standard dissociation model for the simulation of thermochemical nonequilibrium flows.

1. INTRODUCTION

1.1 Thermochemical Nonequilibrium

In the view of classical mechanics, the energy of a diatomic or polyatomic molecule can be separated into translational, rotational, vibrational, and electronic modes. They correspond to the translational motion of the molecule, internuclear rotation, internuclear vibration, and the interaction between electrons and nuclei. In quantum mechanics, similar separation can be achieved by invoking the Born–Oppenheimer approximation and decoupling the rotational and vibrational energy operators. Thus the total wave function of a molecule ψ becomes the product of electronic wave function ψ_{el} , vibrational wave function ψ_{vib} and rotational wave function ψ_{rot} . The independence of the wave functions allows solving the eigenenergies separately. For a dilute gaseous medium composed by a large number of molecules, we can use energy distribution functions to describe the state of the system. Its most probable macrostate, i.e. thermal equilibrium state, corresponds to the one with the largest number of possible microstates. Statistical thermodynamics have found the energy distribution functions of different modes in thermal equilibrium follow Maxwell-Boltzmann distribution and they are characterized by the same parameter, the macroscopically measured temperature [1]. Thermal nonequilibrium arises when the energy distribution functions deviate from Maxwell-Boltzmann distribution or the distribution functions of different modes are characterized by temperatures with different values.

The phenomenon widely exists in supersonic combustion [2], glow and corona discharge [3], micro-electro-mechanical systems [4] and most importantly, hypersonic flight like Earth’s and Martian atmospheric entry of spacecrafts and meteorite bombardment. The root reason for the formation of thermal nonequilibrium is the lack of energy exchange between particles or between different molecular modes. For exam-

ple, the glow discharge in the fluorescent lamp has cold neutrals but electrons with temperature up to tens of thousands Kelvin because the rate of energy exchange is proportional to the ratio of particles' weights, which is very small for electrons and neutrals. Hypersonic thermal nonequilibrium flow is a typical example of thermal nonequilibrium caused by the inefficient energy exchange between different modes. Hypersonic flow is always energetic and characterized by high temperatures. For regions like shock layer or boundary layer, the flow is brought to rest rapidly and the kinetic energy is converted to the "thermal" energy of molecules. Taking Stardust sample return vehicle as an example, it reentered earth at an altitude of 80 km with a speed of 12 km/s. The stagnation temperature in the shock layer can reach up to 25,000 K [5], which is more than 100 times greater than the ambient air temperature. The extremely high temperature is large enough to cause chemical reactions and excitation of the internal modes. However, these processes occur at finite rates. For instance, the relaxation of molecules' vibrational energy usually takes thousands of collisions. When these finite-rate processes coupled with the large convection speeds within the shock layer, a state of thermochemical nonequilibrium is established. Moreover, certain types of reactions like the dissociation, by consuming vibrational energy, further delay the relaxation of vibrational mode. Such effect, the so-called vibration-chemistry coupling, becomes more critical for temperatures higher than a certain value when the reaction rates become comparable to thermal relaxation rates. In such a condition, the gas could never reach thermal equilibrium until the reactants are consumed or temperature drops.

Thermochemical nonequilibrium can have different kinds of influences on hypersonic flights. The level of chemical reactions, especially dissociation, has a direct impact on the shock standoff distance of hypersonic flow around blunt bodies. The increased density across the bow shock reduces the shock standoff distance and changes the pressure distribution and aerodynamic performance of the vehicles. CFD simulations of the entries to Mars by Mars Pathfinder [6], MER [7], Phoenix [8] and Insight [9] commonly found static instability is established near the continuum/non-

continuum boundary and the vehicle is trimmed to a non-zero angle of attack. When combined with the 180° bank angle, this translates into a “lift-down” flight profile, contributing to a short timeline and uptrack landing location relative to prediction.

Thermochemical nonequilibrium is also closely related to heat transfer. The conductive heat transfer due to vibrational excitation increases the total heating rate of the surface [10]. The vibrational and electronic excitation of the gas and the concentration of highly radiative species have a large influence on the radiative emission from the shock layer. The radiative cooling of the flow not only changes the shock structure [11] but also heats up the surface. For example, the radiative heat transfer to the vehicle can constitute over 30% of the total heat transfer rate for the reentry from the moon [12]. Besides, thermal relaxation was found closely related to the laminar-turbulent transition by adsorbing energy from the second-mode instability to delay the transition [13].

1.2 State of the Art Study

To study thermochemical nonequilibrium flow, there are several physical properties needed, including the thermal relaxation time for rotational and vibrational mode (τ_{rot}, τ_{vib}), chemical reaction rates in thermal nonequilibrium condition $k(T, T_r, T_v)$, chemistry-internal energy coupling, transport properties and thermodynamic properties of different species. The spectra of high-temperature, chemically reacting hypersonic flows provides the most powerful tool to obtain these quantities experimentally [14].

Flight experiments, such as the Bow Shock Ultraviolet Flight Experiment (BSUV) [11] and Stardust make it possible to identify the condition for the formation of thermal nonequilibrium and study its impact. The high sensitivity of dissociation rates to the vibrational temperature T_v in vibrationally cold conditions was found to strongly affect the formation and emission of atomic oxygen and nitric oxide for vehicles re-entering at a speed above 8 km/s [15]. CN produced by surface ablation

was detected in the shock layer, which was in vibrationally cold condition [16]. Flight experiments provide the most realistic data for engineering applications, but they are costly and take a long period for planning, design and launching. Moreover, the obtained data are more appropriate for the validation of the whole modeling system as it is not possible to isolate a single physical process.

Alternatively, ground tests provide another way to study thermochemical nonequilibrium flow. The experiments are usually conducted in shock tubes. Techniques like electronic beam scattering [17], ultraviolet, visible light/infrared absorption spectroscopy [18, 19] and x-ray densitometry [20] are used to measure gas concentrations and temperatures. Compared to flight tests, ground-based experiments can measure the radiation of the gas across the shock, whereas flight tests couldn't provide data with spatial resolution and the measured values only represent integration along a line-of-sight passing through the shock layer [16]. Due to such advantages, there have been a number of shock tubes built and experiments carried out from the 1960s to 1990s. Typical studies include Byron et al.'s measurements of O_2 dissociation [21], Wray and Teare's measurements of reactions involving NO [18], Appleton et al.'s measurements of N_2 dissociation [22] and others [23–26]. Several reviews summarized those data and recommended appropriate ones for numerical simulations [27–30]. However, there are some root issues with these historical shock tube measurements. First, although the radiance is the data measured in experiments, the number density profile was inferred from the intensity and used to derive reaction rates. There is no direct comparison of radiance. Second, the measured values were analyzed with the quasi-equilibrium approximation (i.e. $\tau_{vib} \ll \tau_{reac}$) [21, 22]. The degree of vibrational nonequilibrium was only qualitatively analyzed by conducting calculations with both vibrationally frozen and vibrationally equilibrium assumptions, but not quantitatively examined. Moreover, since reactions like dissociation occur at high temperatures and it is difficult if not impossible to isolate vibrational-vibrational (VV) or vibrational-translational (VT) energy exchange from chemical reactions, direct measurements of nonequilibrium reaction rates are hard to perform. The first two

problems were addressed in recent shock tube experiments conducted in the NASA Ames Electric Arc Shock Tube [31]. The new experiments first obtained the spectrum for 190 nm to 1450 nm radiation along the shock wave. Then, flow simulations and radiation calculations were conducted and directly compared to the experimental data to validate reaction rates, radiation model and other key components [31].

Once the properties are obtained, it comes to the modeling and numerical simulations of thermochemical nonequilibrium flow. Computational fluid dynamics (CFD) and direct simulation Monte Carlo (DSMC) are the two principal methods to simulate such type of flow. The CFD method numerically solves Navier-Stokes equations. The internal modes of the gas are modeled by the multi-temperature model, i.e. conservation equations of internal energy and total energy are formulated separately. The widely used two-temperature model solves the following vibrational energy conservation equation in addition to the conservation of total energy,

$$\frac{\partial \rho e_v}{\partial t} + \frac{\partial}{\partial x_j} (\rho e_v u_j) = -\frac{\partial q_{vj}}{\partial x_j} - \sum_s \frac{\partial q'_{vj,s}}{\partial x_j} + \sum_s Q_{T-v,s} + \sum_s Q_{e-v,s} + \sum_s \dot{w}_s D_{vs}, \quad (1.1)$$

where ρ is the mass density, e_v is the average vibrational energy per unit mass, u_j is the convective velocity, q_{vj} is the conductive heat flux of vibrational energy due to the gradient of vibrational temperature and $q'_{vj,s}$ is the diffusion flux due to molecular concentration gradients. The three source terms $Q_{T-v,s}$, $Q_{e-v,s}$ and $\dot{w}_s D_{vs}$ represent vibrational-translational (VT), vibrational-electronic (VE) and vibrational-chemical energy exchange of a species s . The multi-temperature model assumes the energy distribution functions of each mode to be Boltzmann equilibrium distribution. In this context, the Landau-Teller vibrational relaxation model [32] is commonly used in CFD for VT and VE energy exchange. The model describes the change of vibrational energy for a specie s due to VT relaxation as,

$$Q_{T-v,s} = \frac{de_{v,s}}{dt} = \frac{e_{v,s}^*(T) - e_{v,s}}{\tau_{VT,s}}, \quad (1.2)$$

where $e_{v,s}^*(T)$ is the equilibrium vibrational energy at translational temperature T , and $\tau_{VT,s}$ is the VT relaxation time. In regard to chemical reactions, there are different empirical or semi-empirical models to calculate thermal nonequilibrium reaction

rates, including Park's model [33], Marrone-Treanor (MT) model [34] and Knab's model [35]. CFD method with Park's model has been calibrated against some experimental data and has successfully reproduced most flight test radiation data available for reentry velocities up to 10 km/s [27,33]. However, the computational cost increases with the number of species and the method doesn't reveal the detailed non-Boltzmann distribution of internal energies, which can be significant for strong thermochemical nonequilibrium flow. Moreover, those empirical models only estimate the coupling between chemical reactions and vibrational excitation. DSMC method [36], which simulates stochastic molecular collisions, overcomes some difficulties of CFD although at a computational cost. Phenomenological models like variable hard sphere (VHS) and variable soft sphere (VSS) [36] are often used to describe collisions. Once collision occurs, chemical reactions and thermal relaxation happen with a probability depending on the corresponding models. Thus there is no need for the closure of chemistry-internal energy coupling. In particular, there are phenomenological models like total collision energy (TCE) model [36], vibrational favored dissociation (VFD) model [37], vibrational biased models [38,39] and the quantum kinetics (QK) model [40] for the modeling of chemical reactions. Except for QK model, all other models have calibration constants that are adjusted to reproduce experimentally measured reaction rates. The widely-used TCE reaction model can reproduce the same reaction rates in thermal equilibrium condition by inverse Laplace transform. However, the TCE model does not address the roles and the well-established different efficiency of vibrational, rotational, and translational modes in chemical reactions; thus, TCE model can be viewed as semi-empirical.

However, it should be noted that the models for both CFD and DSMC methods are adjusted to reproduce experimentally measured properties near thermal equilibrium conditions. They are limited by the availability of experimentally measured data in thermal nonequilibrium conditions. Whether the models are reliable or not in strong nonequilibrium condition is questionable. A complicated trial-and-error study is needed to find the best model parameters to reproduce a single experiment [41].

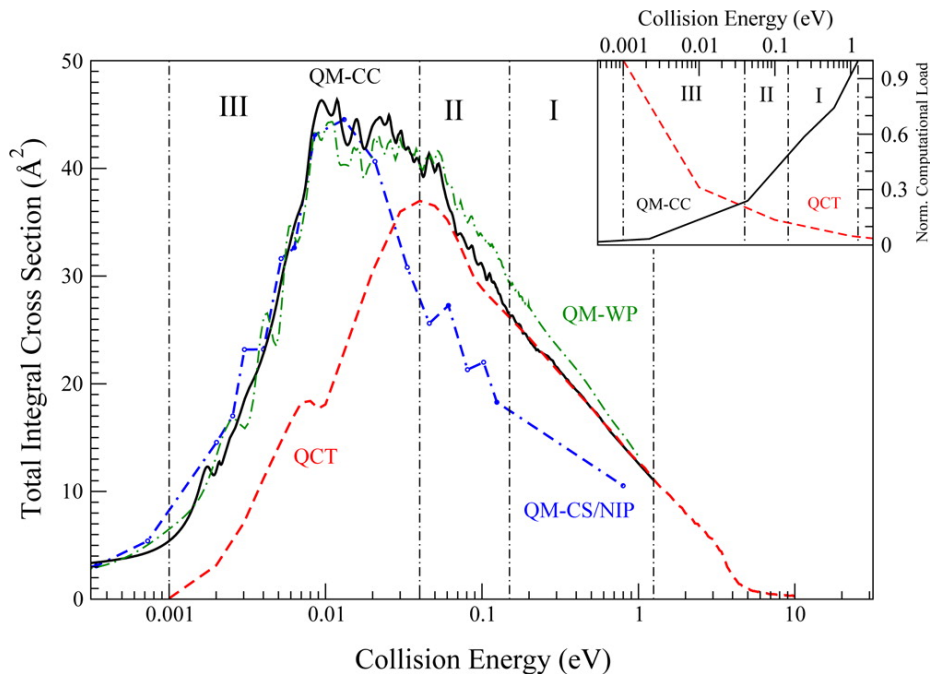


Figure 1.1. Comparison of total integral cross sections for $\text{H} + \text{HeH}^+(v=0, j=0) \rightarrow \text{He} + \text{H}_2^+$ reaction obtained with different dynamical methods. In the inset, a comparison between QCT and QM-CC normalized computational cost estimations is given [42]

Quasi-classical trajectory (QCT) [43,44] and quantum mechanical closed-coupling scattering (QM-CC) [44] are the two theoretical methods used to study molecular collisions and calculate reaction and thermal relaxation rates based on the potential energy surface (PES), which describes the interactions between particles. QCT method, which solves classical mechanics instead of quantum mechanics, can provide identical results to QM-CC approach for high-energy collisions but has a much lower computational cost, as shown in Fig 1.1. Such feature makes it promising for the computation of high-temperature reaction rates and properties. In addition, benefiting from the growth of computational power, it has become feasible to generate *ab initio* PESs for the most species in the atmosphere of Earth and Mars like N_2 , O_2 , NO , CO and CO_2 with larger basis sets and advanced post Hartree-Fock methods, which can resolve most configuration interactions that are important for chemical reactions.

The convergence of different post Hartree-Fock methods is shown in Fig. 1.2. The multireference configuration interaction (MRCI) method has almost become standard today. Table 1.1 summarizes the progress of the PES calculation for N_2O molecule in the recent 40 years.

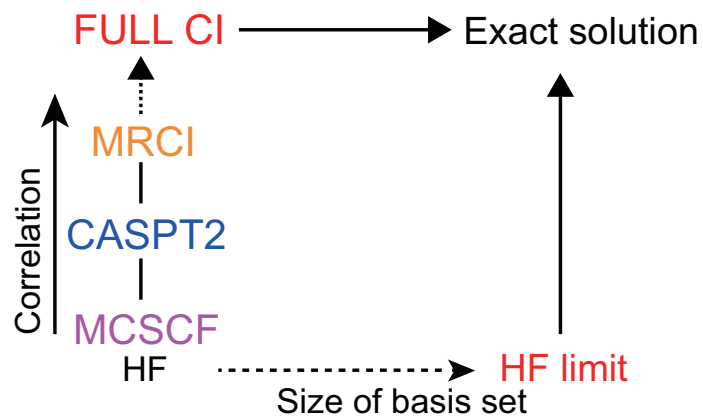


Figure 1.2. Convergence of different post Hartree-Fock methods

Table 1.1.: Summary of *ab initio* PES calculations for N₂O

Electronic state	Year	post Hartree-Fock method	Basis set	Reference
$1^1A'$, $1^3A''$, $1^3A'$	1984	MCSCF	STO-3G	[45]
$1^3A''$, $1^3A'$	1987	CASSCF[10,8]+MRCI	6-311G(2d)	[46]
$1^1A'$, $1^3A''$, $1^3A'$, SOC	1999	CASSCF[16,12]+MCQDPT	cc-pVTZ	[47]
$1^1A'$	2000	CASSCF[16,12]+CASPT2	6-311G(2d)	[48]
$1^3A''$, $1^3A'$	2003	CASSCF[10,9] G2+CASPT2	cc-pVTZ	[49]
$1^3A''$, $1^3A'$	2016	SA-CASSCF[10,9] + MRCI	maug-cc-pVTZ	[50]

SOC: spin-orbital coupling

Table 1.2.: Existing QCT calculation results

Chemical reaction	QCT
$\text{N}_2 + \text{N} \rightarrow 3\text{N}$	51, 52
$\text{O}_2 + \text{O} \rightarrow 3\text{O}$	53–55
$\text{N}_2 + \text{O} \rightarrow 2\text{N} + \text{O}$	56, 57
$\text{N}_2 + \text{N}_2 \rightarrow 2\text{N} + \text{N}_2$	58
$\text{O}_2 + \text{O}_2 \rightarrow 2\text{O} + \text{O}_2$	59–61
$\text{O}_2 + \text{N}_2 \rightarrow 2\text{O} + \text{N}_2$	60–62
$\text{N}_2 + \text{O}_2 \rightarrow 2\text{N} + \text{O}_2$	60–62
$\text{NO} + \text{N}_2 \rightarrow \text{N} + \text{O} + \text{N}_2$	63

The availability of accurate PESs makes QCT method almost a routine for the study of chemical reactions and energy exchange at hyperthermal conditions. QCT calculations have been carried out for many systems as summarized in Table 1.2. The method not only yields statistically averaged reaction rates and relaxation time but provides state-specific reaction cross sections, state-to-state energy exchange cross sections, and elastic scattering cross sections. These detailed data make state-specific modeling possible in CFD and DSMC methods.

1.3 Open Questions and Challenges

Although the knowledge of thermochemical nonequilibrium flow has been dramatically improved in the last decade with the help of QCT method, more work is still needed to improve the predictive capabilities of CFD and DSMC methods in highly nonequilibrium conditions. The challenges are mainly from three aspects: the applicability of QCT method, the accuracy of QCT results and the method of implementing QCT data in CFD and DSMC.

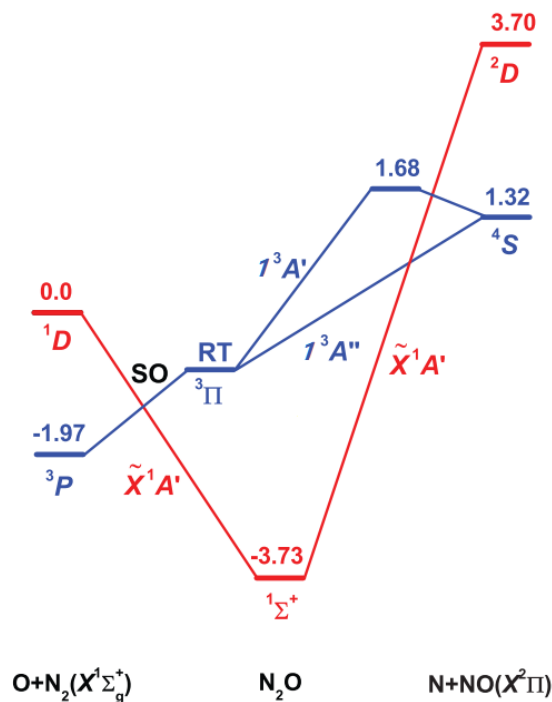


Figure 1.3. N₂O schematic correlation diagram, energies are in electron volt [64]

The QCT calculations require PESs for the colliding pair of interest. For a specific system, there usually exist several electronic states and each state might be correlated with many degenerated states due to the spin-orbit coupling. The PESs are not always available, which leads to the issue for the applicability of QCT method. Figure 1.3 shows the correlation diagram of N₂O system. The ground state N₂(X¹Σ_g⁺) and atomic oxygen correlate to three degenerated states 1³A'', 1³A' and 2³A'' (not shown in the figure). Even with assumption of adiabatic collision by neglecting transition between electronic states, three individual QCT calculations need to be conducted. Figure 1.4 presents a previous calculation of VT relaxation time for N₂+O system [65]. Clearly, the average relaxation time obtained by QCT method based on 1³A'' and 1³A' states is significantly higher than experimental measurements. Except for the neglect of 2³A'' PES, electronically nonadiabatic transition between the singlet and triplet states can also give rise to such overprediction. For N₂O, the PESs of singlet

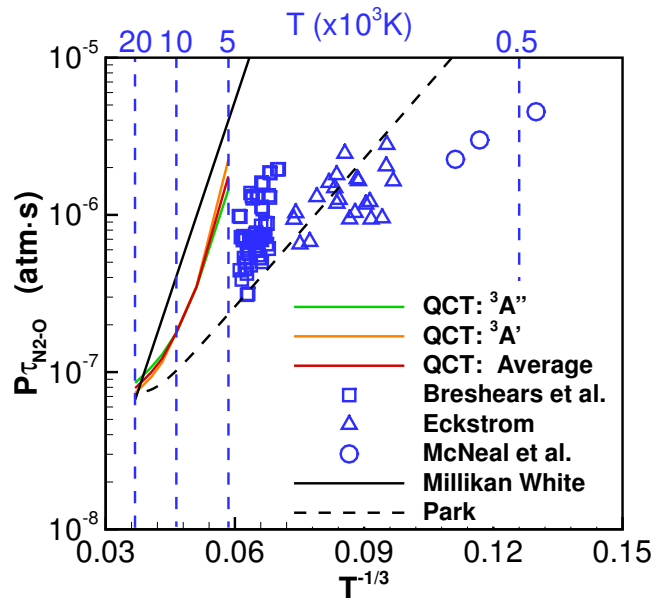


Figure 1.4. Comparison of adiabatic QCT calculated VT relaxation time for N_2+O with experimental measurements

and triplet states cross at certain geometry and nonadiabatic vibrational relaxation could occur at intermediate temperatures. For diatom-diatom system like O_2+O_2 , the situation becomes more complicated. If only the ground state is considered, 9 states arise for O_2+O_2 system because $O_2(X^3\Sigma_g^-)$ is an open-shell molecule and valence electrons are not fully paired. By neglecting spin-orbit coupling, we can reduce the 9 states to 3 states with only different electronic spins, namely singlet, triplet and quintet states [66]. However, it is still a tough task to generate PESs for all of them and carry out the corresponding QCT calculations. The absence of PES for complex systems makes the applicability of QCT method limited.

Even with the complete PESs for a system, QCT method is still not perfect. The first issue is the uncertainties and errors inherent in QCT, including the numerical error of *ab initio* electronic structure calculations of potential energy, the fitting error of the PES, statistical error of QCT calculations, etc. These errors are accumulated together but they are seldom reported with the QCT results, which makes it im-

possible to quantify the uncertainties of QCT data and their influence to CFD and DSMC simulations. Second and the most important, QCT calculations produce massive data and non-trivial effort is required to process the data and implement them in CFD and DSMC [54, 56, 67]. Taking $\text{N}_2\text{-O}$ as an example, the 9751 different rovibrational states of N_2 make the database of state-specific dissociation rates more than a single Arrhenius equation. Although the fit of two-temperature reaction rates is possible [67], the underlying physics is lost and it can become very tedious in order to find an appropriate mathematical formula.

All the challenges mentioned above lead to our thinking of finding a third way to model thermal nonequilibrium reactions based on appropriate assumptions and simplified physics. The model is expected to be as convenient as empirical models but also predict nonequilibrium characteristics nearly as accurate as QCT does. Besides, we also notice there is no direct QCT calculations of thermal nonequilibrium transport properties yet. The transport properties used in CFD or modeled by DSMC were calculated based on simplified two-body potential energy curve [68]. The accuracy of the transport properties is unknown especially for high temperatures. Moreover, the contributions of inelastic collisions to transport properties are definitely not accounted in these simple two-body potentials.

1.4 Goals and Objectives of the Dissertation

The main goal of this work is to find solutions to the challenges summarized in Sec. 1.3 and improve the fidelity of modeling thermochemical nonequilibrium flow in both CFD and DSMC methods. The specific objectives include the study of thermal nonequilibrium transport properties and the development of the thermal nonequilibrium reaction model. The detailed goals are listed as follows:

- **Study of thermal nonequilibrium transport properties**

- 1) Examine the influence of thermal nonequilibrium on transport properties;

2) Study the dependency of transport properties on the degree of thermal nonequilibrium with first-principle methods;

- **Development of nonequilibrium reaction models based on simplified physics**

1) Develop consistent thermochemical nonequilibrium dissociation reaction models based on appropriate assumptions and approximations for both CFD and DSMC methods;

2) Validate the models by comparing nonequilibrium characteristics such as nonequilibrium reaction rates and chemistry-internal energy coupling predicted by the models with QCT data and experimental measurements;

3) Implement the models in CFD and DSMC code and validate the models by simulating 1D shock tube experiment;

In Chapters 2 and 3, the two goals are fulfilled. Concluding remarks and recommendations for future work are made in Chapter 4.

2. THERMAL NONEQUILIBRIUM TRANSPORT PROPERTIES

2.1 Introduction

Accurate values of transport coefficients of high-temperature gases are required for computational fluid dynamics (CFD) modeling of hypersonic reentry and thermal plasma. An uncertainty analysis of NASA’s Crew Exploration Vehicle LEO re-entry shows that, at the peak heating trajectory point, the uncertainty of collision integrals for N_2 -N, N_2 -O and N-O account for almost 90% of the overall stagnation point heating rate uncertainty. At the off-peak heating trajectory point, collision integrals for N_2 -O alone contribute to 81% of the uncertainty [69]. The uncertainty will further increase if the error in predictions of gas concentration is accounted. The analysis of NASA Ames Electric Arc Shock Tube test shows that simulations with the widely-used chemical reaction and radiation model significantly underpredict radiation features attributed to both N_2 and NO [41]. Thus, the accurate modeling of transport properties is of the same importance compared to chemical reactions and gas radiation for the safety of missions. Different from chemical reactions and gas radiation, there are very few measurements of transport coefficients [70, 71] and the temperature range is usually less than 3,000 K. A large amount of effort has been made to calculate the coefficients from Chapman-Enskog theory based on collision integrals [68, 72–75]. Those collision integrals are usually calculated with effective intermolecular potential energy curve (PEC), like Lennard-Jones (L-J) potential for low temperatures and exponential potential for high temperatures. Thus, it is implicitly assumed that molecules don’t have internal structure and collisions are elastic. Mason and Monchick have argued that the assumption is valid as long as the change of internal energy ΔE_{int} is much smaller than $k_b T$ [76]. The argument has been verified

by recent quasi-classical [77] and semiclassical [78] calculations for temperature up to 3,000 K. However, for higher temperatures, the error associated with the assumption has not been quantified. It is unknown how the vibrational excitation of colliding molecules influences the collision integrals.

Tabulated collision integrals or transport coefficients [68, 72, 74] have been widely implemented in modern CFD code for simulations of hypersonic flow. In DSMC method, the transport of mass, momentum and energy are directly controlled by the collision model. There are phenomenological models like VHS [36] and VSS [79]. VHS model takes the following expressions for the scattering angles and total collision cross sections,

$$\chi = 2 \cos^{-1}\{b/d\} \quad (2.1)$$

$$\sigma_{coll} = \pi d^2 = \pi d_{ref}^2 \left(\frac{k_b T_{ref}}{E_t} \right)^{\omega-1} \frac{1}{\Gamma[5/2 - \omega]}, \quad (2.2)$$

where χ is the scattering angle, b is the impact parameter, d is the molecular diameter, d_{ref} is the reference collisional diameter at reference temperature T_{ref} , E_t is the collisional energy and ω is the viscosity index. Closed-form multi-parameter expressions of viscosity, coefficient of diffusion and thermal conductivity can be derived from this. The expressions can be fitted to CFD transport coefficients to predict consistent macroscopic properties. However, those expressions are derived based on quasi-elastic collision approximation but the collisions in DSMC can be inelastic. Besides, VHS and VSS may not predict correct scattering law at hyperthermal conditions. Early classical trajectory calculations with L-J potential discovers the linear dependence of scattering angle on impact parameter [80]. With the popularity of QCT method, there are efforts made to correct total collision cross sections [81, 82]. However, to the best of our knowledge, there is no study of the scattering law and patterns.

In this context, the main goal of this chapter is to investigate thermal nonequilibrium transport properties as well as the scattering law. More accurate values of collision integrals and physically realistic scattering laws are provided to CFD and

DSMC methods. The remaining of this chapter is organized as follows. The influence of thermal nonequilibrium to transport properties is first tested with DSMC method and presented in Sec. 2.2. Next, QCT method is employed for the calculation of collision integrals and scattering angle. The method of calculations and the results are presented in Sec. 2.3. The proposed models are also presented. Finally, concluding remarks are made in the last section.

2.2 Transport Properties with Thermal Nonequilibrium

To get an insight of thermal nonequilibrium's influence to transport properties, CFD and DSMC simulations were first conducted for the same case to analyze the difference of flow properties. The case selected here has a similar free stream condition to the double-cone shock experiment conducted at Calspan University of Buffalo Research Center (CUBRC) [83]. To simplify the problem, a flat plate with zero angle of attack was simulated here. The free stream has a temperature T_∞ of 138.9 K and velocity $V_\infty = 2.712$ km/s. The gas is pure N_2 with chemical reactions frozen and its density ρ_∞ is of 0.522 g/m³. The plate has a constant temperature of 296 K. The DSMC simulation was carried out with SPARTA Direct Simulation Monte Carlo Simulator [84] and CFD simulation was conducted with US3D [85]. Due to the higher computational cost of DSMC, a smaller domain ($L = 0.05m$) was used in DSMC compared as it is highlighted Fig. 2.1. A convergence study was conducted to ensure the simulation result is independent of domain size. The first grid normal to the wall in CFD was also set to ensure $y^+ < 1$.

The free stream condition gives a Mach number of 11.3 and a mean free path of 0.11 mm. The flow is expected to have certain region breaking the continuum flow assumption. Knudsen number is calculated as $Kn = \frac{\nabla \rho}{\rho} \lambda$ based on CFD results. ρ is the mass density and λ is the mean free path. The result is presented in Fig. 2.2. The contour is cutoff at $Kn = 0.05$. It can be found that the flow is close to rarefied gas in the shockwave and near the wall. It is likely that the simulation results of CFD

in regions 1, 3 and 5 are less reliable. Figure 2.3 and 2.4 further present the velocity and translational temperature profiles at different locations. We can clearly see the existence of velocity slip and temperature slip based on DSMC results. The largest slip velocity is found at the leading edge of the plate, which is about 250 m/s. In addition, DSMC predicts higher gradient of velocity at the wall. It is expected that both shear stress and heat flux will be higher if the temperature is the same.

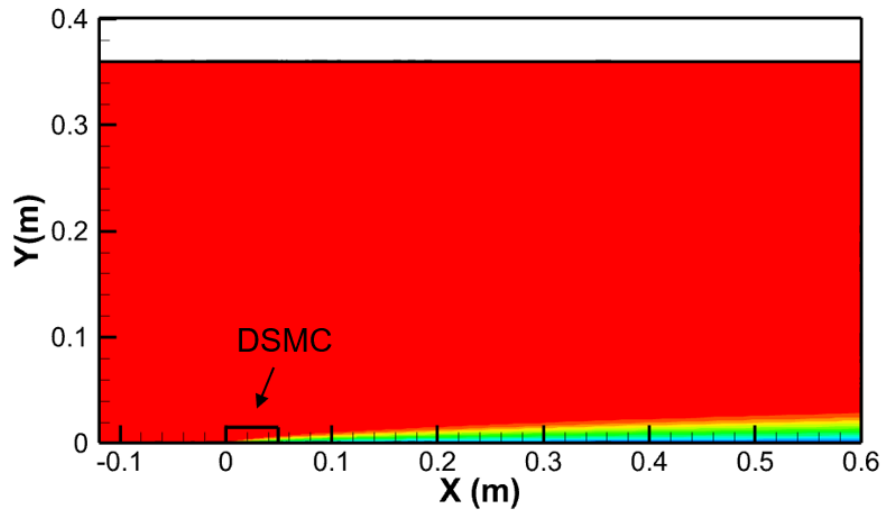


Figure 2.1. Comparison of simulation domains between DSMC and CFD

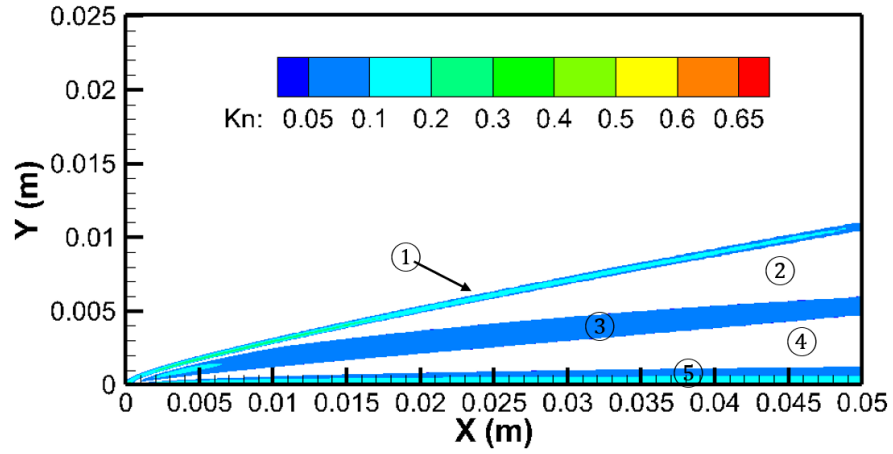


Figure 2.2. Knudsen number calculated from CFD

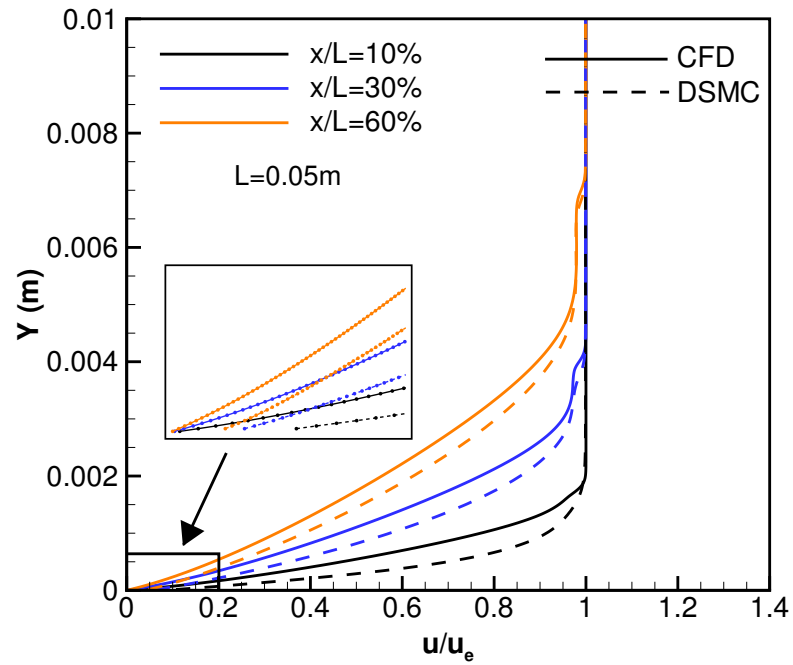


Figure 2.3. Horizontal velocity profiles at different locations near the wall; u_e is the velocity of external flow.

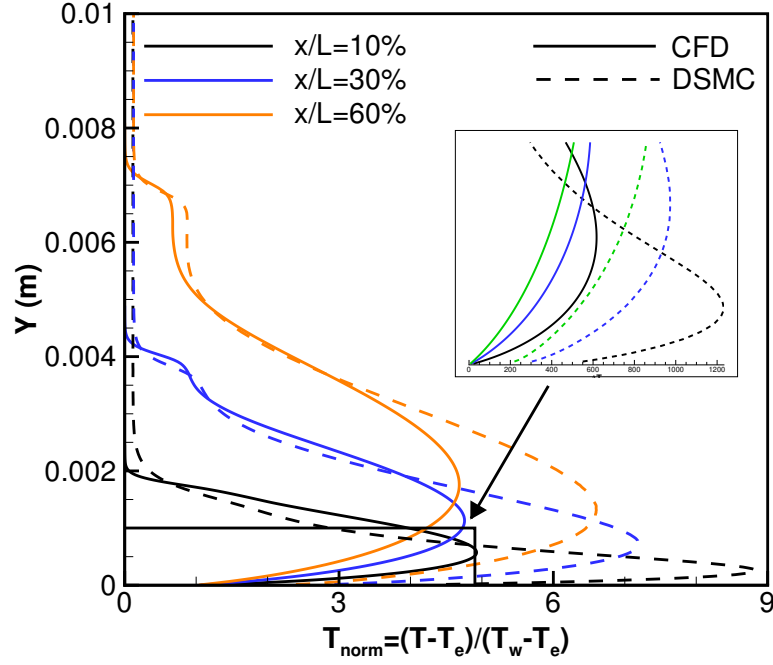


Figure 2.4. Normalized translational temperature profiles at different locations near the wall; T_w is the wall temperature and T_e is the free stream temperature.

The pressure coefficients $c_p = \frac{p - p_\infty}{1/2 \cdot \rho_\infty u_\infty^2}$ and friction coefficients $c_f = \frac{\tau_w}{1/2 \cdot \rho_\infty u_\infty^2}$ are compared in Fig. 2.5. DSMC overpredicts the coefficients by about 10% due to the higher gradient of velocity. For DSMC, the dramatic increase of force coefficients at the leading edge is likely due to the vicinity of a buffer zone in front of the leading edge. Figure 2.6 compares the Stanton number,

$$C_H = \frac{q_w}{\rho_e u_e (h_{aw} - h_w)}. \quad (2.3)$$

where q_w is the local heat-transfer rate, h_{aw} is the adiabatic wall enthalpy and h_w is the enthalpy of the flow. It can be found that DSMC overpredicts the Stanton number by at most 28% near the leading edge. The values of C_H/c_f is also shown here. The Reynolds analogy is still held here as the deviation from the approximation is within 10% for $x > 0.01\text{m}$.

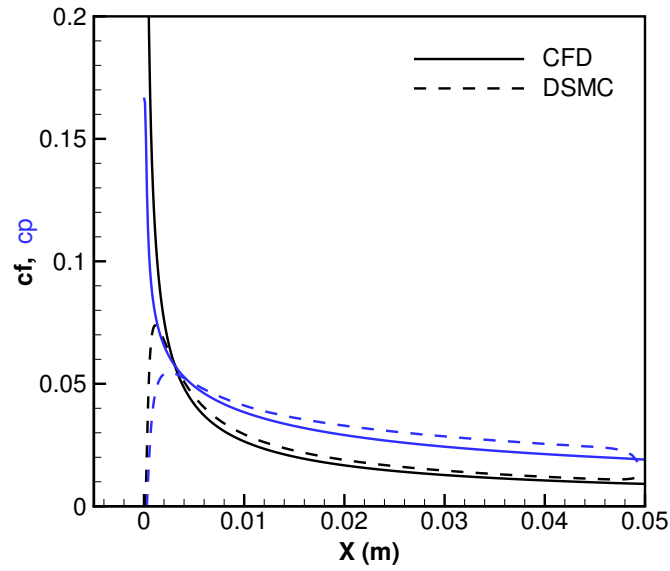


Figure 2.5. Comparison of pressure coefficient between DSMC and CFD

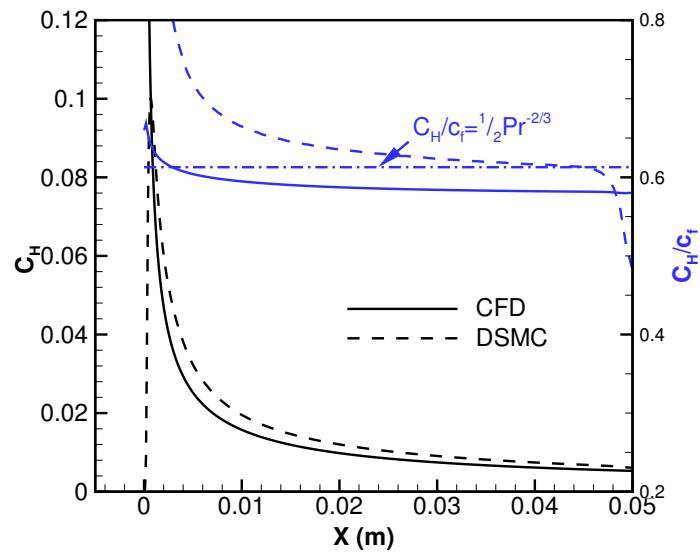


Figure 2.6. Comparison of Stanton number between DSMC and CFD

The translational and vibrational temperatures calculated with DSMC is shown in Fig. 2.7. The flow is clearly vibrationally cold for the whole simulation region.

The vibrational temperature is lowest in the external flow and gradually recovers to the wall temperature on the plate. The translational temperature is highest after the shock and gradually drops when it is closer to the wall.

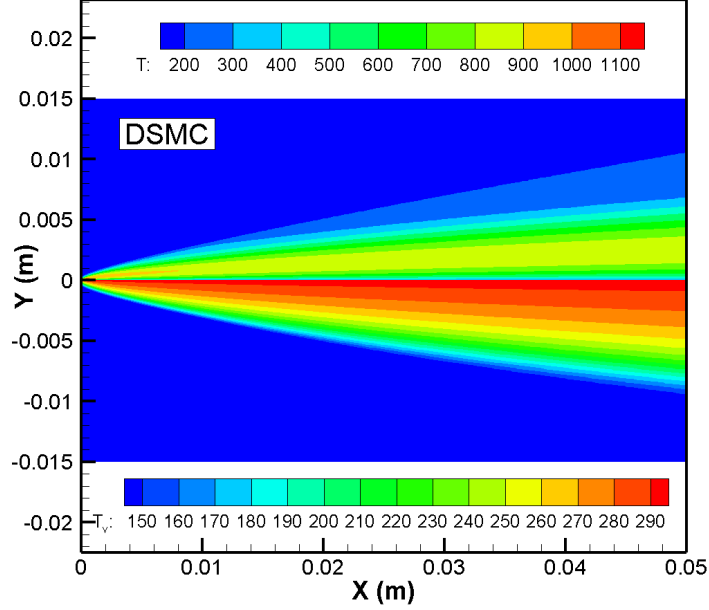


Figure 2.7. Translational and vibrational temperature calculated by DSMC

To infer viscosities from DSMC results, the off diagonal term of the pressure tensor, $\overline{\rho(u - u_0)(v - v_0)}$, is first extracted from the simulation results and then the effective viscosity is calculated as,

$$\mu = -\frac{\overline{\rho(u - u_0)(v - v_0)}}{\frac{du_0}{dy} + \frac{dv_0}{dx}}, \quad (2.4)$$

where u and v are the velocities of a single molecule and u_0 , v_0 are the flow velocities. An example of the viscosity and temperature profiles at $x=0.03$ m is shown in Fig. 2.8. The two blue points denote two locations with the same translational temperature but the top one has a lower vibrational temperature. It can be found that although translational temperatures are the same, the viscosities differ by a factor of 1.24.

This is clearly a result of vibrational nonequilibrium, which will also be supported by theoretical derivations later.

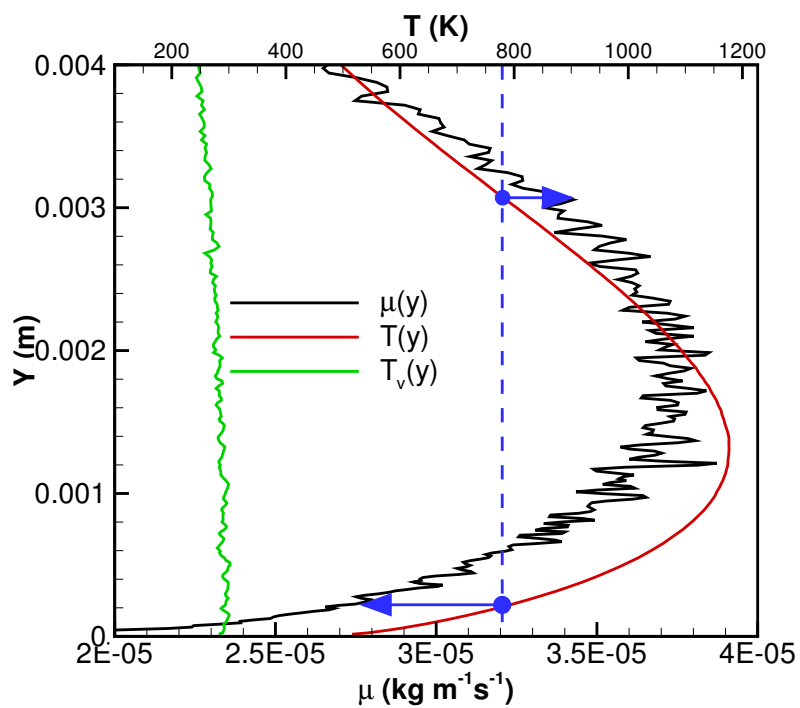


Figure 2.8. Viscosity and temperature profiles calculated by DSMC

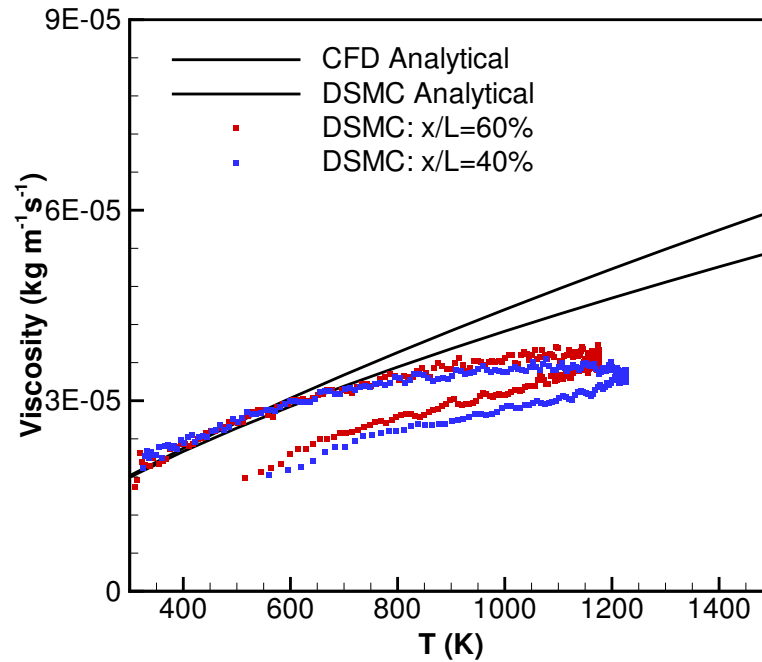


Figure 2.9. Comparison of viscosity between DSMC and CFD

Figure 2.9 shows the comparison of viscosity from different sources as a function of temperature. The analytical values of CFD and DSMC are obtained by directly evaluating the corresponding expressions as functions of temperature. The DSMC analytical values solely depend on the parameters of VHS model and the effect of thermal nonequilibrium and inelastic collision are not taken into account. The “DSMC calculation” are the effective viscosities calculated based on the method mentioned above. The viscosity was calculated along two lines normal to the wall: $x/L=40\%$, and $x/L=60\%$. They both deviate from the DSMC analytical values as the temperature increases when the thermal nonequilibrium is more pronounced. This test case confirms the influence of thermal nonequilibrium to transport properties.

2.3 First-Principle Calculations of Transport Properties

As it has been discussed in Chapter 1, QCT method is mainly used for the calculations of thermal relaxation time and chemical reaction rates. The transport properties and collision dynamics of high-temperature gas were not widely studied. The test case in Sec. 2.2 indicates the potential influence of thermal nonequilibrium to the transport properties. However, the collisional model used in the study is the phenomenological VHS collision model, which doesn't predict physically realistic scattering law especially at hyperthermal conditions. In this section, QCT method is employed first to calculate the collisional integrals for vibrational nonequilibrium conditions. The results are compared with published results based on simplified exponential potential. Then the scattering law is derived from QCT results and the reason for the influence of thermal nonequilibrium on transport properties is explained.

2.3.1 Quasi-classical Trajectory Method

QCT method is a kind of classical description of nuclear collisional mechanism. It takes the Born–Oppenheimer approximation and treats the motion of atomic nuclei separately from the electrons'. The interaction between nuclei is described as a PES, which is calculated by quantum chemistry approach. In general, the method is valid when the wave nature of the internuclear motion can be neglected. Mathematically, QCT solves the following equations to obtain the nuclear motions,

$$\begin{aligned} \frac{dq_i}{dt} &= \frac{\partial H}{\partial p_i}, \\ \frac{dp_i}{dt} &= -\frac{\partial H}{\partial q_i} = -\frac{\partial V}{\partial q_i}, \end{aligned} \tag{2.5}$$

where q_i and p_i are the general coordinates and momenta of molecules, V is the PES parametrically depending on q_i , and H is the Hamiltonian of the system.

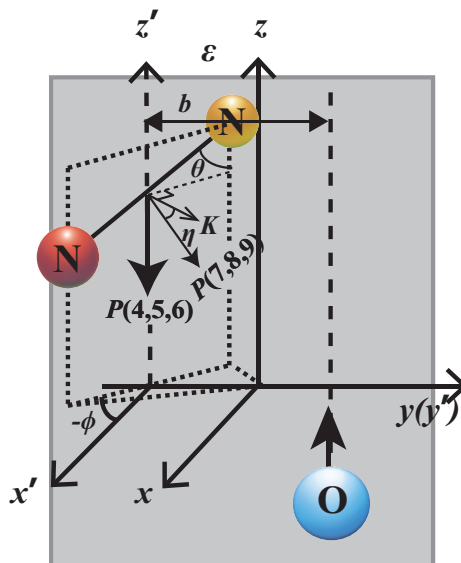


Figure 2.10. Coordinate system for an atom-diatom collision

All QCT calculations start with the sampling of different collisional geometries for specific initial rovibrational states (v, J) and collisional velocity V_r . A typical set up of coordinate system for an atom-diatom collision is shown in Fig. 2.10. Plane ε is the collisional plane, which contains free atom A and the center of mass for BC molecule. Without losing generality, the plane is set as $y - z$ plane and the initial collisional velocity is set parallel to axis z . b is the impact parameter of the collision. θ and ϕ are azimuth and polar angle of molecule BC. η is the reference angle for the molecular momentum.

Millions of collisional trajectories are then propagated. If there are N trajectories with event r happening N_r times, the state-resolved cross sections for the event r will be:

$$\sigma_r(V_r, v, J) = \pi b_{max}^2 \frac{N_r(V_r, v, J)}{N}, \quad (2.6)$$

where b_{max} is the maximum impact parameter for the sampling. The state-resolved rates could also be calculated directly from QCT by averaging the product of cross sections $\sigma_v(V_r, v, J)$ and relative velocities V_r over the spectrum of V_r :

$$k(T, v, J) = \int_0^\infty \sigma_r(V_r, v, J) V_r f(V_r, T) dV_r = \sqrt{\frac{8\pi kT}{m_r}} b_{max}^2 \frac{N_r(T, v, J)}{N}, \quad (2.7)$$

where $f(V_r, T)$ is the Boltzmann distribution of collisional velocity V_r at temperature T and $N_r(T, v, J)$ is the count of event r happening. Besides, QCT can also be used to find scattering law by analyzing the distribution function of scattering angles. A crucial factor influences the accuracy of the QCT results is the number of trajectories propagated. *Monte Carlo* integration converges as $1/\sqrt{N}$. If the sampling error is defined as one standard deviation, the uncertainty of the calculations can be estimated as the following when the number of samples is large enough.

$$\Delta\sigma_r(V_r, v, J) = \pi b_{max}^2 \frac{N_r}{N} \sqrt{\frac{N - N_r}{NN_r}}, \quad \Delta k_r(T, v, J) = \sqrt{\frac{8\pi kT}{m_r}} b_{max}^2 \frac{N_r}{N} \sqrt{\frac{N - N_r}{NN_r}}. \quad (2.8)$$

The QCT code used in the present work is Adiabatic and Nonadiabatic Trajectories (ANT) developed by Truhlar's research group [86]. Modifications were made to the sampling of vibrational phase angles. Instead of assuming that diatomic molecules are harmonic oscillators with equal spacing between adjacent vibrational levels, the rovibrational ladder is first solved with WKB approximation,

$$\frac{1}{\hbar} \int_{r_-}^{r_+} \left[2\mu(E_{rv}(v, J) - V(r)) - \frac{\hbar^2 J(J+1)}{r^2} \right]^{1/2} dr = (v + \frac{1}{2})\pi, \quad (2.9)$$

where v and J are the vibrational and rotational quantum, $V(r)$ is the diatomic potential energy curve, r_- and r_+ are the inner and outer turning points, μ is the reduced mass and E_{rv} is the quantized rovibrational energy. Then the vibrational phase angle distribution function is solved numerically with the classical mechanics description of oscillator,

$$\frac{1}{2}\mu \left(\frac{dr}{dt} \right)^2 + \frac{J(J+1)\hbar^2}{2\mu r^2} + V(r) = E_{rv}(v, J) \quad (2.10)$$

2.3.2 Method of Computing Transport Properties

The formal, bimolecular results for the transport coefficients obtained in the Chapman-Enskog theory have been discussed in Ref. 87. In this work, we used the

same notations as Hirschfelder et al. used [87]. The viscosity and diffusion coefficient of a binary mixture can be calculated from collision integrals as:

$$\mu = \frac{5}{16} \frac{\sqrt{2\pi m_r k_b T}}{\pi \sigma^2 \Omega^{(2,2)*}}, \quad (2.11)$$

$$D = \frac{3}{16} \frac{\sqrt{2\pi k_b^3 T^3 / m_r}}{p \pi \sigma^2 \Omega^{(1,1)*}}, \quad (2.12)$$

where $\Omega^{(1,1)*}$ and $\Omega^{(2,2)*}$ are reduced collision integrals of diffusivity D and viscosity μ , m_r is the reduced mass of the binary mixture, $\pi \sigma^2$ is the reference collision cross sections of the corresponding rigid sphere molecules and T is the temperature. To solve the collision integrals $\Omega^{(i,j)}$, one can follow Chapman-Enskog procedure and use Sonine polynomial expansion to solve Boltzmann equations. However, the classical kinetic theory neglects internal structure of molecules [76]. Wang Chang and Uhlenbeck [88] developed a theory for semiclassical case and took inelastic collisions into consideration. The collision integrals for A + B collisions, where A and B are molecules with internal structure. are calculated as the following for a given temperature T ,

$$\Omega^{(1,1)} = \sqrt{\frac{k_b T}{2\pi m_r}} \cdot \pi \sigma^2 \Omega^{(1,1)*} = \sqrt{\frac{k_b T}{2\pi m_r}} \int_0^\infty \sum_{i,j} \left(\frac{e^{-\varepsilon_i} e^{-\varepsilon_j} \sum_{k,l} Q^{(1)kl}_{ij}(\gamma)}{Z_A Z_B} \right) \gamma^2 \times e^{-\gamma^2} \gamma^3 d\gamma, \quad (2.13)$$

$$\Omega^{(2,2)} = \sqrt{\frac{2k_b T}{\pi m_r}} \cdot \pi \sigma^2 \Omega^{(2,2)*} = \sqrt{\frac{k_b T}{2\pi m_r}} \int_0^\infty \sum_{i,j} \left(\frac{e^{-\varepsilon_i} e^{-\varepsilon_j} \sum_{kl} Q^{(2)kl}_{ij}(\gamma)}{Z_A Z_B} \right) \gamma^4 \times e^{-\gamma^2} \gamma^3 d\gamma. \quad (2.14)$$

where indices i and j label the initial (pre-collision) internal states of the molecule A and B, and indices k and l label the final (post-collision) internal states. The internal energy of molecule A and B before collision is E_i and E_j . The energies are nondimensionalized by the temperature T as $\varepsilon_i = E_i/k_b T$ and $\varepsilon_j = E_j/k_b T$. Z_A and Z_B are the internal energy partition functions for the colliding pair and m_r is the reduced mass. γ^2 is the reduce collisional energy of A + B, i.e. $\gamma^2 = \varepsilon =$

E/k_bT . Different from classical kinetic theory, the expressions here not only contain an integration over collision energy but also a thermally average over distribution functions of internal energy. Thus, the results are expected to be different if thermal nonequilibrium exists. $Q^{(1)}$ and $Q^{(2)}$ are the momentum cross sections and viscous cross sections. The superscript indicates the post-collision states and subscript indicates the pre-collision states. The momentum cross sections $Q^{(1)}$ and viscous cross sections $Q^{(2)}$ are evaluated as:

$$Q^{(1)kl}_{ij}(\gamma) = \int_{b,\mathbf{\Omega}} \left[1 - \frac{\gamma'}{\gamma} \cos \chi \right] P^{kl}_{ij}(\gamma, b, \mathbf{\Omega}) \times 2\pi b db d\mathbf{\Omega}, \quad (2.15)$$

$$Q^{(2)kl}_{ij}(\gamma) = \int_{b,\mathbf{\Omega}} \left[\sin^2 \chi + \frac{\Delta\varepsilon^2}{\gamma^4} \left(\frac{1}{3} - \frac{1}{2} \sin^2 \chi \right) \right] P^{kl}_{ij}(\gamma, b, \mathbf{\Omega}) \times 2\pi b db d\mathbf{\Omega}, \quad (2.16)$$

where $\gamma'^2 = E'/k_bT$ is the post-collision reduced energy of the colliding pair, χ are scattering angles, b is the impact parameter, $\mathbf{\Omega}$ is the solid angle and P^{kl}_{ij} is the probability of a collision experiencing internal energy transition from (i, j) to (k, l) with a scattering angle χ . $\Delta\varepsilon$ is the change of reduced collision energy, which is calculated as the following:

$$\Delta\varepsilon = \gamma^2 - \gamma'^2 = \varepsilon_k + \varepsilon_l - \varepsilon_i - \varepsilon_j. \quad (2.17)$$

It is seen from Eq. 2.15-2.17 that if $\Delta\varepsilon \ll \gamma^2$, the expressions for momentum cross sections and viscous cross sections will recover to the ones widely used in CFD community, which is a result of quasi-elastic assumption [76]. It should be noted that, Wang-Chang-Uhlenbeck's theory doesn't account the contributions to transport properties by chemical reactions.

To calculate transport cross sections $Q^{(l)}$, one can use either QM-CC [70] or QCT method [77]. Although QM-CC has the highest accuracy, QCT approach was proved to have good agreements with QM-CC starting from $E_t \sim 0.1$ eV but at a lower computational cost [42]. Since we are mainly concerned with high-temperature transport coefficients, QCT approach is selected to calculate the cross sections. The modified version of ANT [86] was used to calculate transport cross sections and collisional integrals. The details of QCT method and the code have been well explained in the

previous section. A major change we made here is the introduction of the importance sampling function,

$$h(b) = 3(1 - b/b_{max}), \quad (2.18)$$

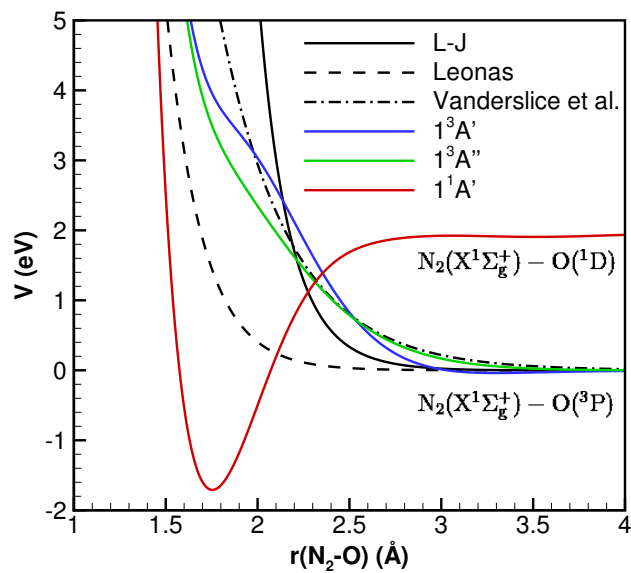
where b_{max} is the maximum impact parameter sampled in the calculations. The reason for using importance sampling is that the small-impact-parameter collisions contribute most to the collision integrals. The technique helps to reduce variance and accelerate convergence. With the importance sampling function, the unbiased estimators of the standard variance of collision integrals are given by:

$$\hat{\sigma}(\Omega^{(l,l)}) = \sqrt{\frac{k_b T}{2\pi m_r}} \cdot \frac{\pi b_{max}^2}{2} \left\{ \frac{1}{N-1} \left[\overline{\left(\frac{g^{(l)}}{h}\right)^2} - \frac{\overline{g^{(l)}}^2}{h} \right] \right\}^{1/2}, \quad l = 1, 2 \quad (2.19)$$

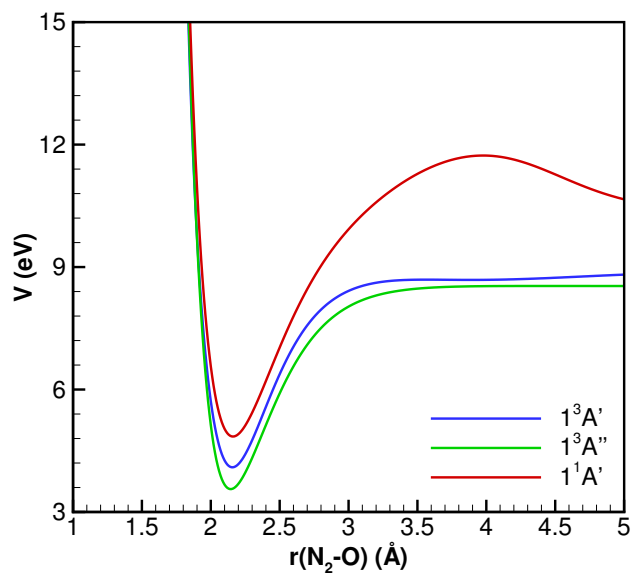
$$g^{(1)} = \gamma^2 - \gamma\gamma' \cos \chi, \quad (2.20)$$

$$g^{(2)} = \gamma^4 \sin^2 \chi + (\gamma^2 - \gamma'^2)^2 \left(\frac{1}{3} - \frac{1}{2} \sin^2 \chi \right), \quad (2.21)$$

where N is the number of non-reactive trajectories. It should be noted that, to calculate collision integrals with quasi-elastic assumption, one only needs to replace γ' by γ in Eq. 2.20 and 2.21 here.



(a)



(b)

Figure 2.11. One dimensional cut of PESs ($\angle\text{NNO} = 180^\circ$) with different distance between N_2 and O. $r(\text{N-N})$ is fixed at different distance, (a) $r(\text{N-N}) = r_e = 1.0977 \text{ \AA}$; (b) $r(\text{N-N}) = 2 \text{ \AA}$

In the present work, two systems, $\text{N}_2(\text{X}^1\Sigma_g^+) - \text{O}(^3\text{P})$ and $\text{N}_2(\text{X}^1\Sigma_g^+) - \text{O}(^1\text{D})$ are investigated. The previous one asymptotically correlates to the ground state nitrogen and atomic oxygen. Their interaction can occur via three PESs in C_s symmetry, namely $1^3\text{A}'$, $1^3\text{A}''$ and $2^3\text{A}''$. Since there is no complete PES for $2^3\text{A}''$ state, only $1^3\text{A}'$ and $1^3\text{A}''$ states are studied here and *ab initio* PESs calculated by Gamallo et al. [49] are used. It should be noted that the $2^3\text{A}''$ state has a more repulsive potential compared to the other two [89]. Thus, it is expected that the overall average collision integrals will be larger when the state is taken into account. We also conduct study for $\text{N}_2(\text{X}^1\Sigma_g^+) - \text{O}(^1\text{D})$ asymptotes because it adiabatically correlates with the ground state $\text{N}_2\text{O}(\text{X}^1\Sigma)$ via $1^1\text{A}'$ PES in C_s geometry and has a potential well in $C_{\infty v}$ geometry, although the state only takes a weight of 1/5 in all possible interactions. The one-dimensional cuts of *ab initio* PESs for $1^3\text{A}'$, $1^3\text{A}''$ and $1^1\text{A}'$ state are shown in Fig. 2.11. A L-J potential obtained by fitting experimentally measured total elastic collision cross sections [90] and two exponential potentials (Leonas [91] and Vanderslice [92]) are also shown in the same figure. It is seen that Yun and Mason's potential gives best agreements to the *ab initio* PESs of $1^3\text{A}'$ and $1^3\text{A}''$ states. Both L-J potential and Leonas's potential are more repulsive than *ab initio* PESs. Thus, the collision integrals are expected to be larger due to the increased scattering angle. For vibrationally frozen N_2 (shown in Fig. 2.11a), except $1^1\text{A}'$ state, all other PESs are repulsive. However, once the vibration mode of N_2 molecule is excited, three-body interactions make the PESs have a deep well as it is shown in Fig. 2.11b, which indicates the possibility of scattering with $\chi < 0^\circ$. In order to obtain the mean collision integrals $\bar{\Omega}^{(l,l)}(T)$, the values of each state are combined together according to their electronic degeneracy as the following:

$$\bar{\Omega}^{(l,l)}(T) = \frac{9/2 \times \Omega_{1^3\text{A}'}^{(l,l)}(T) + 9/2 \times \Omega_{1^3\text{A}''}^{(l,l)}(T) + 5 \times \Omega_{1^1\text{A}'}^{(l,l)}(T) \exp(-22,830 \text{ K}/T)}{9 + 5 \cdot \exp(-22,830 \text{ K}/T)} \quad (2.22)$$

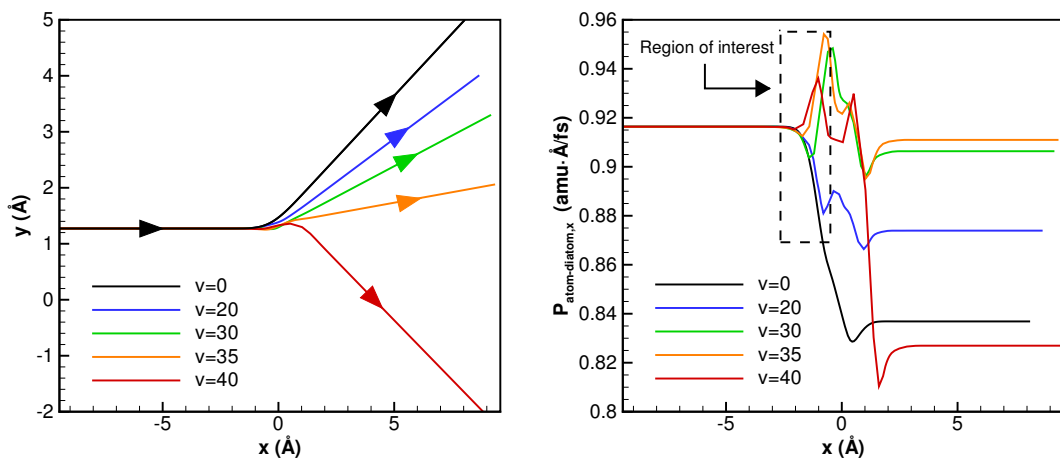
2.3.3 Collision Integrals for N₂-O

Our investigations start with the analysis of vibrational state-specific collision integrals for the three PESs. The vibrational state-specific collision integrals are defined as the following in the present work,

$$\Omega^{(l,l)}(v, T) = \sqrt{\frac{k_b T}{2\pi m_r}} \left[\sum_{J(v)} \frac{(2J+1) \exp(-(E_{rv}(v, J) - E_{rv}(0, J))/k_b T)}{Z(v, T)} \cdot \int_0^\infty Q_{v,J}^{(l)}(\gamma) \gamma^{2l+3} e^{-\gamma^2} d\gamma \right], l = 1, 2 \quad (2.23)$$

where E_{rv} is the rovibrational energy of N₂ molecule with rovibrational state (v, J) , $Q_{v,J}^{(l)}$ are the corresponding collision cross sections defined in Eq. 2.15 and 2.16, and $Z(v, T)$ is the partition function of N₂ molecule with vibrational state v and rotational temperature T ,

$$Z(v, T) = \sum_J (2J+1) \exp(-(E_{rv}(v, J) - E_{rv}(0, J))/k_b T) \quad (2.24)$$



(a) Trajectories of atomic oxygen

(b) Component of N₂-O relative momentum in x direction

Figure 2.12. Examples of trajectories for atomic oxygen colliding with nitrogen molecule with different initial vibrational level on $1^3A''$ PES

The diffusion and viscosity type collision integrals ($\sigma^2\Omega^{(1,1)*}$, $\sigma^2\Omega^{(2,2)*}$) of different temperatures and vibrational levels are reported in Fig. 2.13 to 2.15. The error bar gives a confidence interval of 95%. In general, it is found that the collision integrals decrease as temperature increases, which is a result of “smaller” molecule for higher temperature. There is also a correlation between the vibrational level of N_2 molecule and the collision integrals. An analysis of intermolecular collisions at impulsive limit shows that, vibrational energy contributes to dissociation reaction by its component along the direction of collision [93]. As vibrational energy increases, the component of relative momentum in the direction of collision increases. Thus, the scattering angle, as well as collision integrals should decrease. This is confirmed by comparing specific trajectories with different initial N_2 vibrational level. In Fig. 2.12, five trajectories of atomic oxygen are presented. These collisions have the same impact parameter of 2\AA and collisional velocity of 9 km/s . Both N_2 molecule and atomic oxygen are located in the $x - y$ plane, and the N_2 molecule is orientated such that the N-N bond is parallel to x axis. It is seen from Fig. 2.12a that the scattering angle indeed decreases with N_2 vibrational level increased. The increase of relative momentum in the direction of collision can be also found from Fig. 2.12b. It is also noticed that the scattering angle becomes negative for very high vibrational level on $1^3A'$ and $1^3A''$ PES. As it is explained in Sec. 2.3.2, this is due to the potential well coming with the stronger three-body interaction. The attractive force makes the molecules scattered with negative angles, which is one reason for the increase of collision integrals at $v > 30$. For $1^1A'$ state, since the potential well always exists, collision integrals almost monotonically increase with vibrational level.

In Fig. 2.13, the collision integrals calculated with quasi-elastic approximation are also presented with dashed lines. A satisfactory agreement to the ones following Wang-Chang and Uhlenbeck’s theory is found for low vibrational levels. For higher vibrational levels, we can clearly see the contributions from inelastic collisions. The two effects, i.e. negative scattering angle and inelastic collision, results in the difference collisional integrals for high vibrational levels by up to 50%. However, it should

be noted that, due to the low population of vibrationally excited molecules at thermal equilibrium conditions, such difference might have a negligible influence on the mean collision integrals.

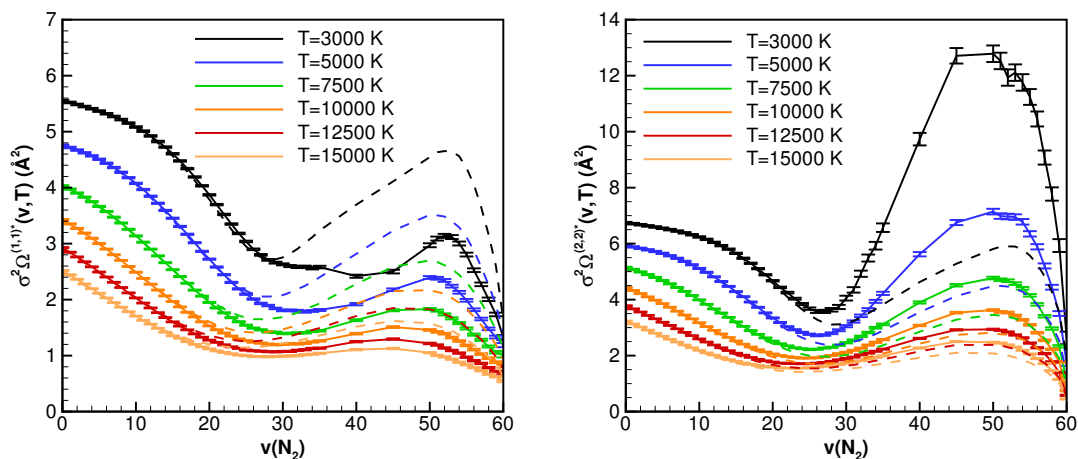


Figure 2.13. Diffusion and viscosity type collision integrals for $1^3A''$ state

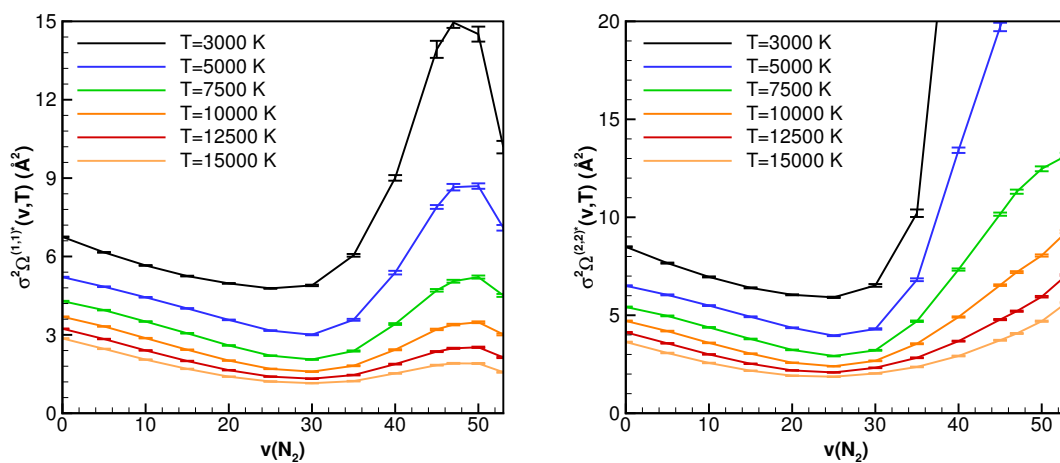


Figure 2.14. Diffusion and viscosity type collision integrals for $1^3A'$ state

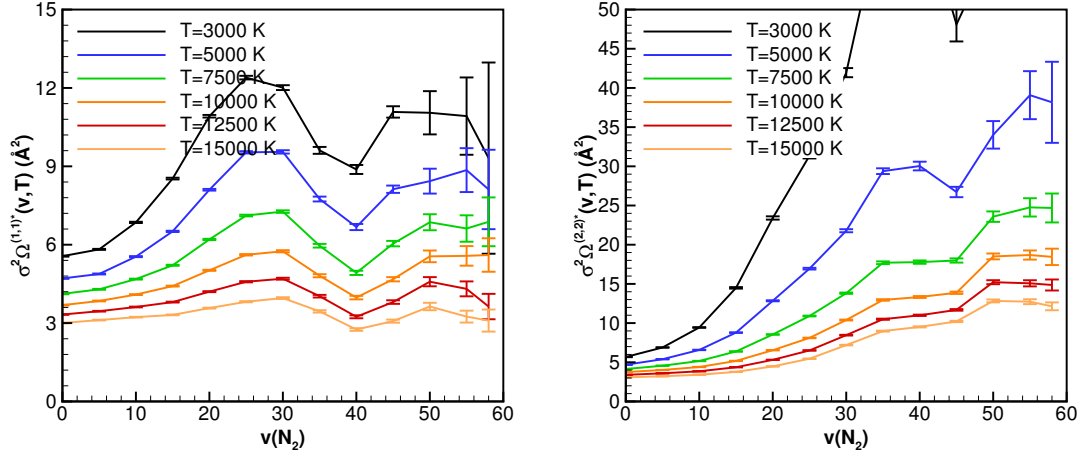


Figure 2.15. Diffusion and viscosity type collision integrals for $1^1A'$ state

Once the vibrational state-specific collision integrals are obtained, the calculations of thermally averaged collision integrals are straightforward,

$$\Omega^{(l,l)}(T, T_v) = \sum_v \frac{\exp(-E_{rv}(v, J=0)/k_b T_v)}{Z_v(T_v)} \Omega^{(l,l)}(v, T), \quad l = 1, 2. \quad (2.25)$$

Here, the distribution function of vibrational energy is set as Boltzmann distribution in order to keep consistency with CFD method. $Z_v(T_v)$ is the partition function of vibrational energy. The results are presented in Fig. 2.16 to 2.18 for different electronic states.

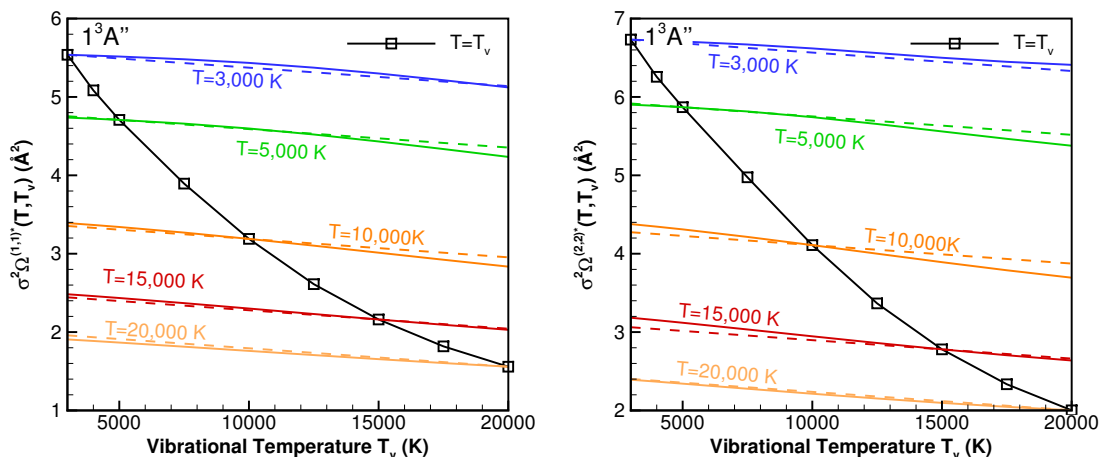


Figure 2.16. Collision integrals at different vibrational temperature for $1^3A''$ state. The error bar is smaller than the size of symbols.

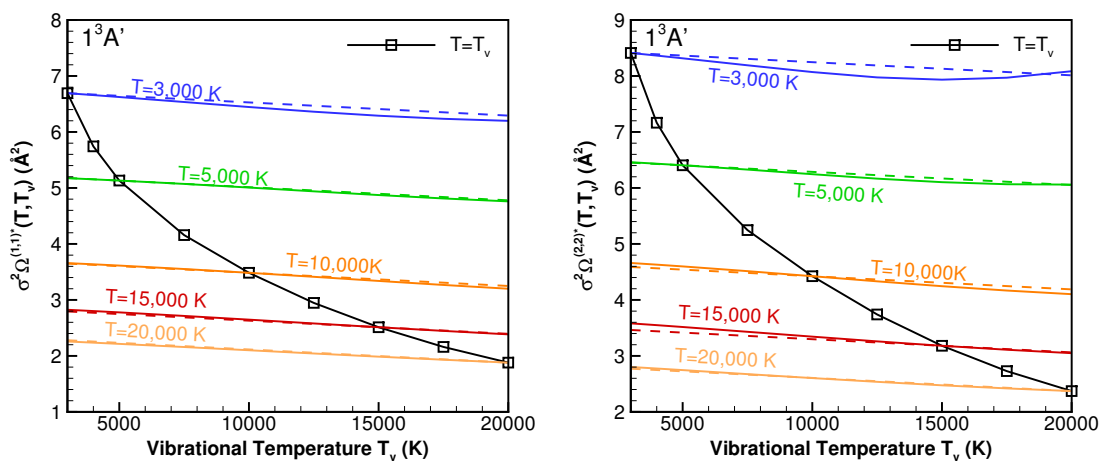


Figure 2.17. Collision integrals at different vibrational temperature for $1^3A'$ state. The error bar is smaller than the size of symbols.

For $1^3A'$ and $1^3A''$ state, linear dependence is found between collision integrals and vibrational temperature as shown in Figs. 2.16 and 2.17. Since $\Omega^{(l,l)}(v, T)$ are of the same orders of magnitude for different vibrational levels, the collision integrals are mainly controlled by the low level non-excited molecules and the values

decrease monotonically with vibrational temperature. $\sigma^2\Omega^{(l,l)*}(T, T_v)$ can be fitted to the following expression with residue less than 0.2 \AA^2 ,

$$\sigma^2\Omega^{(l,l)*}(T, T_v) = \sigma^2\Omega^{(l,l)*}(T) - \frac{T_v - T}{42,500 \text{ K} \cdot \text{\AA}^{-2}}, \quad l = 1, 2. \quad (2.26)$$

The fitted results are shown as dashed lines in Fig. 2.16 and 2.17. With the fitting, we can expand transport coefficients in Eq. 2.11 and 2.12 as a function of temperature deviation from thermal equilibrium (i.e. $T_v - T$). A first order expansion tells,

$$\Delta\mu(T, T_v)/\eta(T) \approx \frac{1}{42500 \cdot \sigma^2\Omega^{(2,2)*}(T)}(T_v - T), \quad (2.27)$$

$$\Delta D(T, T_v)/D(T) \approx \frac{1}{42500 \cdot \sigma^2\Omega^{(1,1)*}(T)}(T_v - T). \quad (2.28)$$

It can be found that the difference is proportional to $T_v - T$ and inversely proportional to the mean collision integrals. Since the mean collisional integrals decrease as temperature increases, it is expected vibrational nonequilibrium has greater influence to transport coefficients at high temperature vibrationally cold conditions. For $1^3A'$ and $1^3A''$ state, the maximum deviation of transport coefficients from their values at thermal equilibrium conditions is found up to 15% for the condition with $T = 20,000 \text{ K}$ and $T_v = 3,000 \text{ K}$, which corresponds to a difference of 20% for collision integrals. For $|T - T_v| \leq 5,000 \text{ K}$, the deviation is less than 5%.

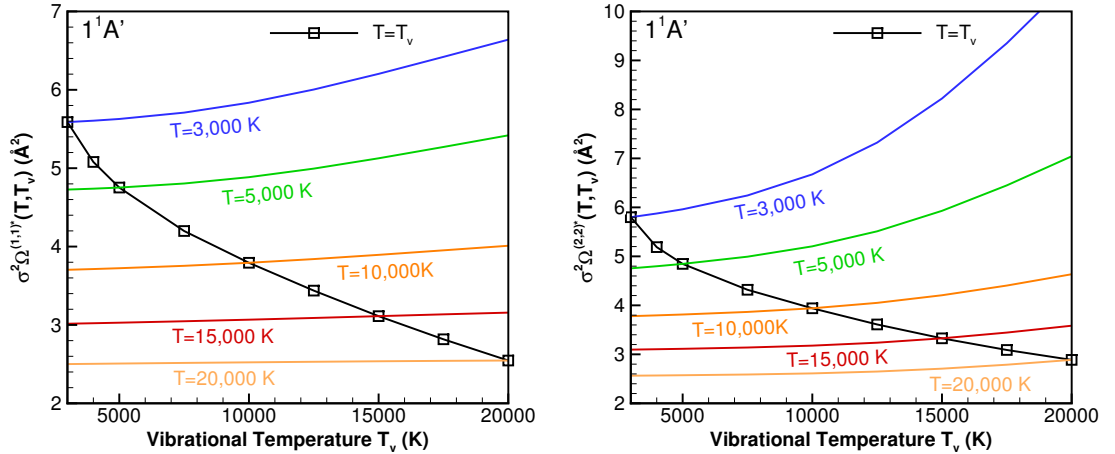


Figure 2.18. Collision integrals at different vibrational temperature for $1^1A'$ state. The error bar is smaller than the size of symbols.

For $1^1A'$ state, since collisions are mainly controlled by attractive force, and $\Omega^{(l,l)}(v, T)$ increases rapidly with vibrational level, the thermally averaged collision integrals increase with vibrational temperature and the deviation of their values from the ones at equilibrium conditions is about 20~60% as shown in Fig. 2.18. However, it should be noted that the singlet state takes less weight than the triplet states and its contributions to mean collision integrals are small.

In summary, we did find collision integrals, as well as transport coefficients change when vibrational nonequilibrium exists. However, the values change by less than 5% for $|T - T_v| \leq 5,000$ K for the two triplet states. The collision integrals can be approximately described by a single translational temperature. For the singlet state, stronger dependency on vibrational temperature is found.

Finally, the mean collision integrals calculated with Eq. 2.22 are compared with other published data in Fig. 2.19. The two-body potential used in those data were already summarized in Sec. 2.3.2. Capitelli et al. [74] used the L-J potential for $T < 1,000$ K and Leonas's exponential potential for higher temperature. Yun and Mason [94] used Vanderslice et al.'s exponential potential and conducted calculations for temperature ranging from 1,000 K to 15,000 K. Gupta et al. [68] fitted Yun and Mason's results and extrapolated to up to 30,000 K. Wright et al. [72] summarized Murphy's [95] calculations, which used the L-J potential. All these results were obtained based on classical mechanics and Chapman-Enskog procedure. Since there is no experimental data for the species investigated here, it is hard to comment which results are more accurate. However, our results are in between the upper bound given by Gupta et al. [68] and the lower bound given by Capitelli et al. [74] for $T \leq 10,000$ K. There is a good agreement compared to Yun and Mason's data for low temperature due to similarity of PES. For higher temperatures, the uncertainty is about 30~50% in diffusion and viscosity type collision integrals, which gives rise to an uncertainty up to 26% for coefficients of diffusion and 20% for viscosity. For implementation of

the collision integrals calculated in this work, the results are fitted to the following expressions, which are valid from 3,000 K to 20,000 K,

$$\begin{aligned}\sigma^2\bar{\Omega}^{(1,1)*} &= \exp(-0.4355) \times T^{-0.0927 \log T + 1.0281}, \\ \sigma^2\bar{\Omega}^{(2,2)*} &= \exp(-1.0067) \times T^{-0.1024 \log T + 1.2042}.\end{aligned}\tag{2.29}$$

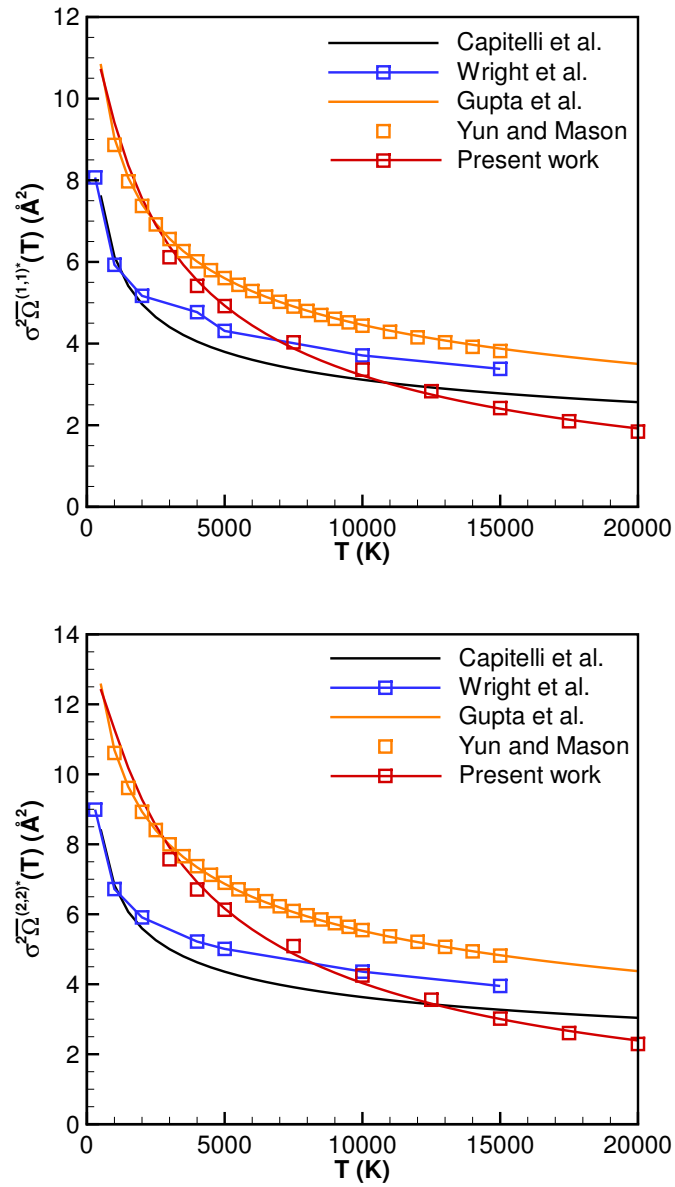


Figure 2.19. Comparison of the mean collision integral for different models

2.3.4 Scattering Law for N₂-O

In DSMC method, collision model is the only factor determining transport properties. With the improvement of computational power, there are efforts using QCT method to calculate total collision cross sections [81] or calibrate VSS model [82]. To the best of our knowledge, there is no study of the scattering law by QCT method. In the present work, scattering angles for different initial conditions of collision are calculated and a new scattering law is proposed. The calculations was only conducted for 1³A'' state due to the similarity between the two triplet states and the lower statistical weight of the singlet state.

The QCT calculated average scattering angles are compared with VSS and M1 model [80] in Fig. 2.22. The M1 model is a modification of the VHS model that addresses the linear dependency of scattering angle on impact parameters for repulsive molecular potential. The scattering angles are calculated as

$$\chi(b) = \pi[1 - b/d_{M1}(V_r)], \quad b < d_{M1}(V_r) \quad (2.30)$$

where d_{M1} is the reference diameter. It can be found that VSS model overpredicts the scattering angle and doesn't capture the linear dependency of scattering angle on impact parameter. M1 model, on the other hand, shows better agreements. It should be noted that, VSS model is a phenomenological model in nature. It only aims at predicting power-law type transport coefficients. In order to resolve the mathematical singularity of calculating collision integrals, it has a cut-off of maximum impact parameter. Whereas QCT calculations are based on realistic intermolecular interactions. As the impact parameter goes to infinity, most collisions become glancing collisions and the mean scattering angle gets closer to zero. Fig. 2.21 presents the probability density function of scattering angles. In contrast to VHS model where χ is isotropic and peaks at $\chi = 90^\circ$, QCT shows strong non-isotropic behavior. The most probable scattering angle is zero. Neither VSS nor M1 model is able to capture such behavior. In addition, a separate comparison of hyperthermal collisions with collisional velocity V_r higher than 9 km/s in Fig. 2.20b shows that, the average scat-

tering angle has a bimodal behavior. Although the scattering angle is still linearly dependent on impact parameter, the function $\chi(b)$ has a larger slope for small-impact-parameter collisions ($b < 1\text{\AA}$) than large-impact-parameter collisions ($b > 1\text{\AA}$). It can be also noticed that small-impact-parameter collisions have similar scattering angles for different collisional velocity.

For implementation of the law of scattering in DSMC, the average scattering angle is fitted to the following expression,

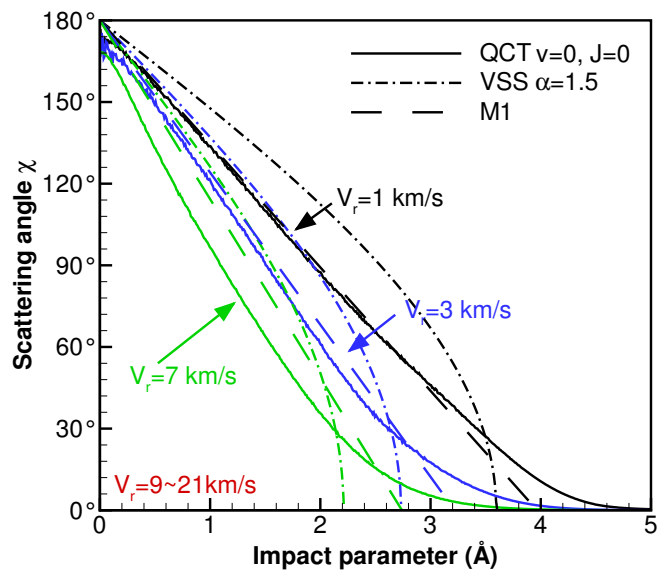
$$\chi(b, V_r) = (a_1 + a_2 V_r) \left[1 - \frac{1}{c + \log(2)} \cdot (b - \log(\cosh(b - c))) \right],$$

$$a_1 = 1.783072, a_2 = 0.016980, \tag{2.31}$$

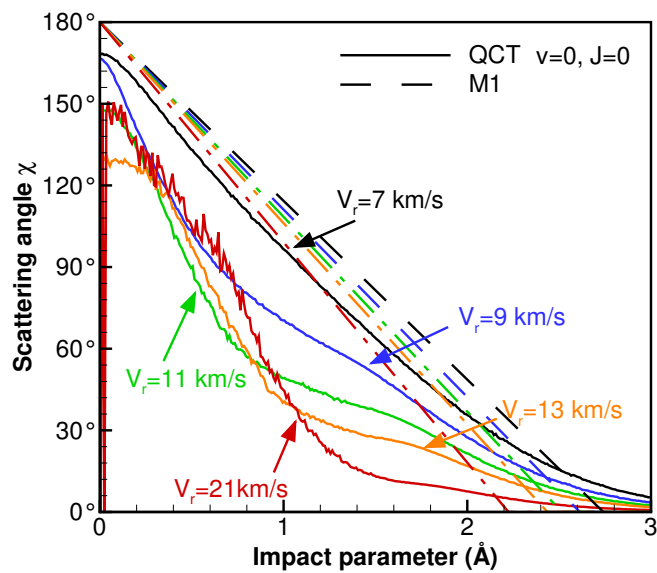
$$c = c_1 \exp(-c_2 V_r) + c_3 \exp(-c_4 b),$$

$$c_1 = 2.846003, c_3 = 2.189955, c_2 = 0.294963, c_4 = 0.078702,$$

where V_r is collisional velocity in kilometer per second and b is the impact parameter in angstrom. Scattering angles calculated for collisions with initial conditions $V_r = 1 \sim 9$ km/s, $v(\text{N}_2) = 0$ and $J(\text{N}_2) = 0$ are used in the fitting. Those trajectories with initially vibrationally excited N_2 are neglected due to their lower weights. As it is shown in Fig. 2.22, a satisfactory agreement is found between the fitted model and original data. Maximum deviation is less than 5° . In Fig. 2.23, collision integrals calculated with the model are compared with QCT results presented in Sec. 2.3.3. Due to the inaccurate modeling of high velocity collision, the discrepancies become larger as temperature increases.



(a)



(b)

Figure 2.20. Comparison of the scattering angles χ predicted by different collision models

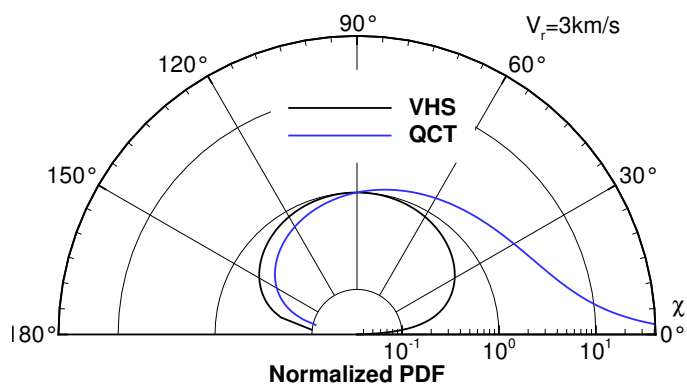


Figure 2.21. Normalized probability density function of scattering angles

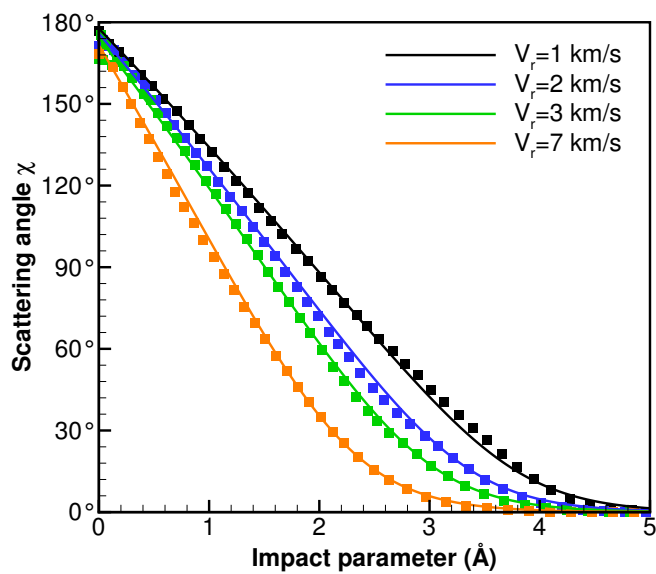


Figure 2.22. Comparison of the scattering law between QCT data (symbols) and the fitted model (lines)

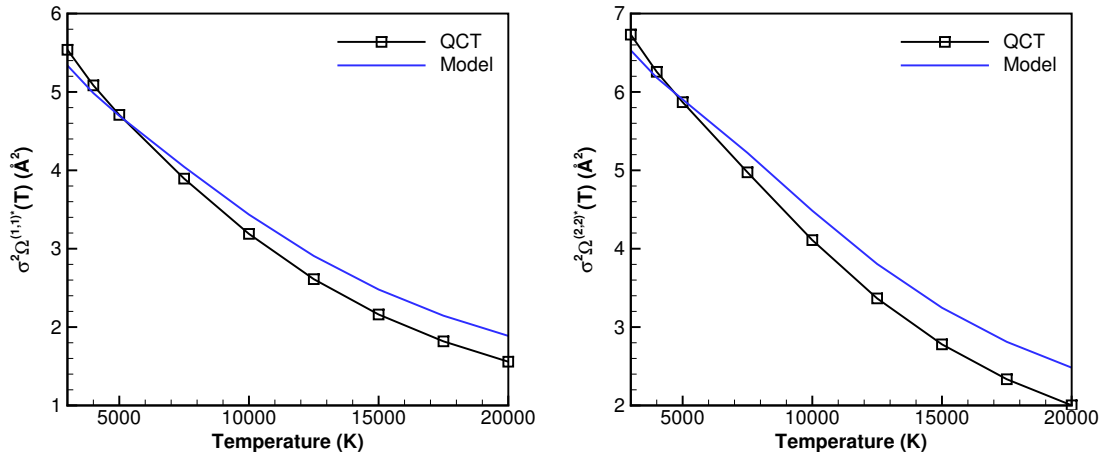


Figure 2.23. Comparison of collision integrals calculated with the proposed model to QCT results

2.4 Summary

First-principle calculations of collision integrals $\Omega^{(1,1)}$ and $\Omega^{(2,2)}$ are conducted in this work with QCT method. *Ab initio* PESs for three electronic states of N₂-O system, namely $1^1A'$, $1^3A'$ and $1^3A''$ are used. By analyzing the vibrational state-specific collisional integrals calculated for the triplet states, it is found that vibrational excitation has different effects on the scattering for different degree of excitation. When the vibrational mode is moderately excited, additional momentum is provided in the direction of collision, which makes the relative collisional velocity larger and scattering angle smaller. This results in a decrease of collision integrals. As the vibrational excitation gets stronger, three-body interactions become comparable to two-body interactions since the molecular bond is stretched. The existence of potential well, as well as strong attractive force, makes scattering angles become more negative. The inelastic collision also starts to play a role. The overall result is an increase of collision integrals.

At strong thermal nonequilibrium conditions, it is found that vibrational nonequilibrium can make the values of collision integrals deviate from those at thermal equi-

librium conditions by up to 20% for the two triplet states and 50% for $1^1A'$ state, which corresponds to 15% and 50% change of transport coefficients accordingly. For weak nonequilibrium conditions with $|T - T_v| \leq 5,000$ K, the collision integrals, as well as transport coefficients, change by less than 5% since $\Omega(v, T)^{(l,l)}$ are of the same orders of magnitude for different vibrational levels. The approximation of quasi-elastic collisions and using a single translational temperature to model collision integrals are valid as long as the conditions are not highly vibrationally hot or cold. Comparing QCT results to the ones calculated with L-J or exponential potential, an uncertainty of 30~50% is found in collision integrals. The more repulsive wall of empirical PESs contributes to its larger values. The QCT calculated mean collision integrals are fitted and can be directly implemented in CFD. In addition, the separate calculations conducted for scattering angles suggest that the physically realistic scattering angles are highly non-isotropic. VHS model tends to overpredict the values for collisions with large impact parameters and M1 model is a better choice. To conclude, we believe that with the popularity of QCT method, the method should not only be used to calculate chemical reaction rates and internal energy relaxation time, but also implemented in the studies of transport properties when accurate PESs are available.

3. DEVELOPMENT OF NONEQUILIBRIUM DISSOCIATION MODEL

3.1 Motivation and Background

The coupling of vibrational energy relaxation to molecular dissociation reaction is recognized as an important physical phenomenon that needs to be modeled for thermochemical nonequilibrium flow around high-speed missiles and re-entering vehicles. The high speed of the vehicles results in high enthalpy and high temperature in shock and boundary layers. Because VT relaxation time τ_{VT} scales approximately as $\tau_{VT} \sim \exp(T^{-1/3})$ while the characteristic reaction time τ_{reac} is approximately $\tau_{reac} \sim \exp(T)$, the depletion of vibrational energy due to dissociation is faster than the compensation from VT relaxation when translational temperature T is above a certain value T_0 . Thus vibration-dissociation coupling always exists in such high-temperature conditions. The high sensitivity of dissociation rates to the vibrational temperature T_v in vibrationally cold conditions was found to strongly affect the formation and emission of atomic oxygen and nitric oxide for vehicles re-entering at a speed above 8 km/s [96]. In plasma chemistry, the opposite regime is realized: the dissociation reaction can occur at room temperature due to the presence of vibrationally hot molecules produced in collisions with electrons [97]. Due to the importance of nonequilibrium dissociation reaction in practical applications, accurate modeling of this process is needed.

To model thermal nonequilibrium dissociation, two key components are needed, including the chemical reaction rates or probabilities in thermal nonequilibrium conditions, and chemistry-internal energy coupling. Flight experiments, such as the Bow Shock Ultraviolet Flight Experiment (BSUV) [11] and Flight Investigation of Reentry Environment [98], or ground-based shock tube experiments [31, 99, 100] provide the

measurement of high-temperature gas radiation intensity and make it possible to verify empirical thermal nonequilibrium chemical reaction models. The simple empirical two-temperature model proposed by Park [33] has successfully reproduced a number of experimental data available for velocities up to 10 km/s. However, the model is empirical and thus cannot be expected to give reliable predictions outside the range of conditions for which it has been calibrated. Additionally, Park’s model implicitly assumes that the internal energy obeys the Boltzmann distribution. Direct simulation Monte Carlo (DSMC) [36] eliminates the assumption by simulating stochastic molecular collisions. The widely-used total collision energy (TCE) reaction model can reproduce the same reaction rates in thermal equilibrium condition by inverse Laplace transform. However, the TCE model was recognized to overpredict the dissociation rates at vibrationally cold condition but underpredict the rates at vibrationally hot condition [56].

Recently, several *ab initio* PESs have become available for first-principle calculations of chemical reaction rates. Together with the rapidly growing computational power, QCT simulations are becoming almost routine. This enables the calculation of reaction rates and probabilities for conditions of interest. However, QCT method is not perfect. Indeed, uncertainties or errors inherent in QCT include the uncertainties of *ab initio* electronic structure calculations, fitting error of the PES, statistical error of QCT calculations etc. Quantifying all such uncertainties is a difficult task. The sensitivity of the results to the details of PES was also not studied in detail. In addition, QCT data cannot be directly used in CFD and DSMC methods due to the massive database, and non-trivial effort required to process the QCT data in order to generate appropriate model [54, 56, 67].

In addition to empirical models and QCT-based approximations, there is a third approach: physical models based on reasonable assumptions and approximations. The models are not limited by the availability *ab initio* PES while maintain the most important physics. Such a model can be based on the theory of nonequilibrium dissociation at high temperature utilizing the assumption of classical impulsive

collisions, developed by Macheret et al. in the early 1990s [101–104]. The so-called Macheret-Fridman (MF) theory was originally used to derive closed-form formula for two-temperature reaction rates used in CFD. In the present work, the CFD model was first re-examined and some minor corrections are made to the earlier derived formulas. The modified model was compared with the old one and validated by QCT data and experimental data. Next, a new DSMC dissociation model, i.e. MF-DSMC model, was proposed based on the MF theory. The new model was gradually improved by incorporating more physics. The different versions of the model are compared and validated by experimental or QCT data. Consistent collision models are also proposed. Finally, the simulations of O_2 reacting shock with the MF-DSMC models are compared with experimental measurements.

3.2 Macheret-Fridman Theory of Dissociation

First, we consider the fundamental theory of MF model [101]. The theory simplifies the mechanism of dissociation at high temperatures with a few important assumptions. Like QCT calculations, it assumes that translational, rotational, and vibrational motion can be described by classical mechanics. Next, because of the high velocity required for dissociation especially from low vibrational states, the Massey parameter $\xi = \frac{\Delta U R}{\hbar V}$ is much smaller than one, where ΔU is the energy transferred into the vibrational mode, R is the characteristic radius of interaction, V is the relative velocity of the colliding particles, and \hbar is the reduced Planck's constant. Therefore, the collision can be viewed as instantaneous, i.e. close to the impulsive limit. The details of PES are not important in such an approximation; additionally, the molecules do not experience three-body interactions before and after the collision. The last approximation is that the reaction rates are only determined by the energy threshold and the behavior of the cross sections just above the threshold. The dependency of the energy distribution function $f(E)$ and reaction cross sections $\sigma(E)$ on collisional energy is qualitatively shown in Fig. 3.1. It can be found that due to the exponential

dependence of the distribution function on energy, the reaction rates, which equals to the integration of $f(E)\sigma(E)$ over the whole energy spectrum, only depend on the behavior of cross sections in the vicinity of the threshold.

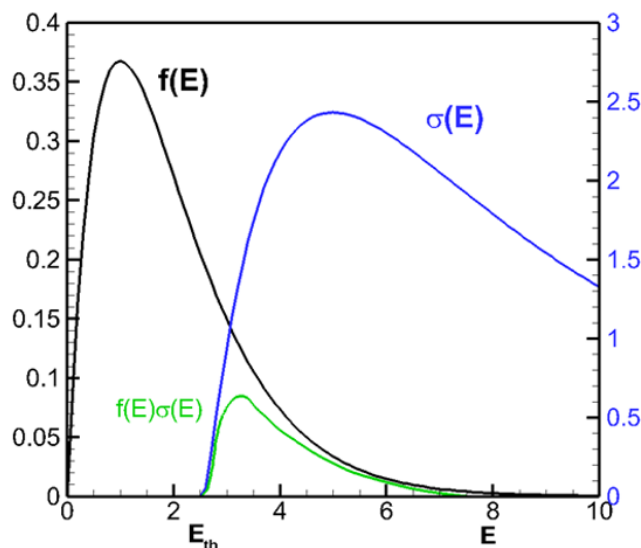


Figure 3.1. Qualitative description of energy distribution function $f(E)$ and reaction cross sections $\sigma(E)$

The central idea of MF theory is the concept of threshold energy, i.e. the minimum collision energy for the dissociation of the molecule. In the original MF theory, only the threshold energy of homonuclear molecules was derived. In the present work, the theory is extended by also considering heteronuclear molecules. This makes the model able to describe the dissociation of species like CO and NO, which can be important for Martian entry.

The collision geometries for diatom-atom and diatom-diatom collisions are shown in Fig. 3.2. Molecule AB is the dissociating molecule and CD is the colliding partner. A right-handed coordinate system is defined in a following manner: atom A, B and C form the xy plane and y axis is in the direction of BC. In the center of mass frame, the velocities of molecule AB and BC are v and u accordingly. The angles γ_1 and γ_2

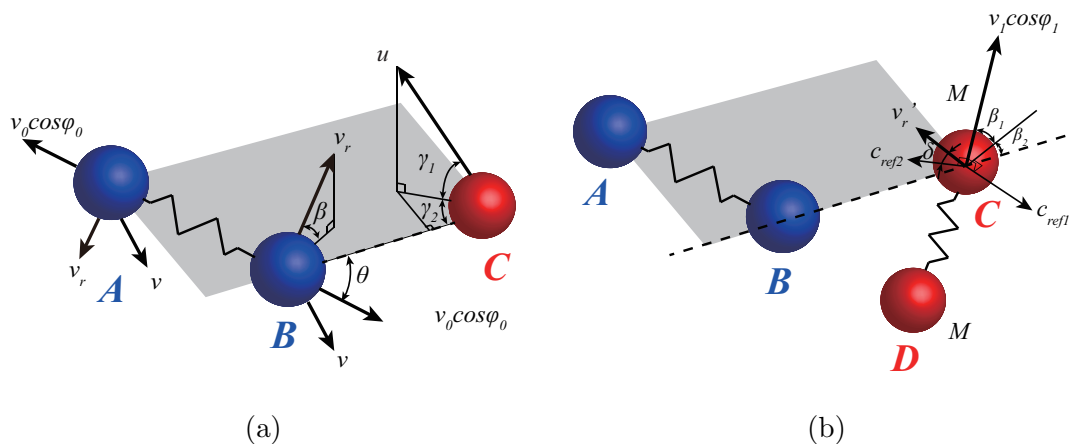


Figure 3.2. Collision geometries: (a) diatom-atom; (b) diatom-diatom.

are the polar and azimuthal angles for velocity u . To simplify reaction probability calculations, we first assume that molecular vibrational motion is harmonic. This means that the phase angles of vibration φ_0 and φ_1 are distributed uniformly between 0 and 2π , and the maximum velocities of vibration v_0 and v_1 can be calculated from the corresponding vibrational energy as they would be for a harmonic oscillator. As will be shown later, little error is introduced by the harmonic oscillator assumptions for low-lying vibrational states. For higher vibrational levels, a more precise way of modeling is to first calculate the distribution of phase angle with the actual potential energy curve and then sample the phase angle based on the distribution. Such approach is addressed later in Sec. 3.4.4.

The magnitudes of vibrational velocities for the specific phase angles are $v_0 \cos \varphi_0$ and $v_1 \cos \varphi_1$. The direction of AB vibrational velocity is determined by the angle θ . The polar and azimuthal angles of CD vibrational velocity are β_1 and β_2 . v_r is the rotational velocity of molecule AB. Its direction is perpendicular to the vibrational velocity of molecule AB with a polar angle β . To define the direction of rotational velocity v'_r for molecule CD, two reference vectors \vec{c}_{ref1} and \vec{c}_{ref2} are introduced. \vec{c}_{ref1} is in xy plane and perpendicular to the vibrational velocity v_1 . \vec{c}_{ref2} is perpendicular to both \vec{c}_{ref1} and v_1 . Then, the direction of rotational velocity v'_r is uniquely determined

by the angle δ between v'_r and \vec{c}_{ref2} and it must be in the plane formed by \vec{c}_{ref1} and \vec{c}_{ref2} .

Denote the mass of atom A, B, C and D as m_A , m_B , m_C and m_D , the reduced mass of molecule AB and BC become $\mu_{AB} = m_A m_B / (m_A + m_B)$ and $\mu_{CD} = m_C m_D / (m_C + m_D)$. For the case of diatom-atom collision, μ_{CD} is equal to the mass of atom C. We can also calculate the reduced mass of the whole system:

$$\mu = \begin{cases} (m_A + m_B)m_C / (m_A + m_B + m_C), & \text{for diatom-atom} \\ (m_A + m_B)(m_C + m_D) / (m_A + m_B + m_C + m_D), & \text{for diatom-diatom} \end{cases} \quad (3.1)$$

The relations between velocities and energies become:

$$\begin{aligned} E_v &= 2\mu_{AB}v_0^2, & E'_v &= 2\mu_{CD}v_1^2, & E_r &= 2\mu_{AB}v_r^2 \\ E'_r &= 2\mu_{CD}v_r'^2, & E_t &= \frac{(m_A + m_B)^2 v^2}{2\mu} \end{aligned} \quad (3.2)$$

where E_v , E'_v are the vibrational energy of molecule AB and CD, E_r , E'_r are the rotational energy of each molecule and E_t is the collisional energy.

The energy and momentum transfer are only allowed in the direction of collision. By projecting the vibrational and rotational velocities of each molecule on the direction of collision, we can get the pre-collision velocities of atom B and C as the following,

$$\begin{aligned} \vec{v}_B &= \begin{bmatrix} -\cos\beta\cos\theta & \sin\theta & \cos\gamma_1\sin\gamma_2 \\ \cos\beta\sin\theta & \cos\theta & \cos\gamma_1\cos\gamma_2 \\ \sin\beta & 0 & -\sin\gamma_1 \end{bmatrix} \begin{bmatrix} v_r \frac{2\mu_{AB}}{m_B} \\ v_v \frac{2\mu_{AB}}{m_B} \\ v \end{bmatrix} = M_B \cdot X_B \quad (3.3) \\ \vec{v}_C &= \begin{bmatrix} -\cos\beta_2\sin\delta + \sin\beta_1\sin\beta_2\cos\delta & -\cos\beta_1\sin\beta_2 & -\cos\gamma_1\sin\gamma_2 \\ -\sin\beta_2\sin\delta - \sin\beta_1\cos\beta_2\cos\delta & \cos\beta_1\cos\beta_2 & -\cos\gamma_1\cos\gamma_2 \\ \cos\beta_1\cos\delta & \sin\beta_1 & \sin\gamma_1 \end{bmatrix} \begin{bmatrix} v'_r \frac{2\mu_{CD}}{m_C} \\ v'_v \frac{2\mu_{CD}}{m_C} \\ v \frac{m_A + m_B}{m_C + m_D} \end{bmatrix} \\ &= M_C \cdot Y_C \quad (3.4) \end{aligned}$$

Two-body problem is solved for the elastic collision between atom B and C while atom A and D maintain their original velocities. Once the post-collision velocities \vec{v}_A' , \vec{v}_B' , \vec{v}_C' and \vec{v}_D' are known, the new vibrational energy of the dissociating molecule AB can be obtained,

$$\hat{E}_v = 2\mu_{AB}v_0^2 \sin^2 \varphi_0 + \frac{1}{2}\mu_{AB} \left[-(\vec{v}_A'^{iT} - \vec{v}_B'^{iT}) \cdot \begin{bmatrix} \sin \theta \\ \cos \theta \end{bmatrix} \right]^2 \quad (3.5)$$

The post-collision vibrational energy \hat{E}_v is a function of collisional energy E_t , pre-collision internal energies E_v , E_r , E'_v , E'_r and collision geometries. By making post-collision vibrational energy of molecule AB equal to the dissociation energy D , we can obtain the threshold function $F = E_{t,min}$, which is the minimum collisional energy for the dissociation reaction $AB + CD \rightarrow A + B + CD$ to occur. For diatom-atom collision, the threshold function is,

$$F = \frac{\mu/\mu_{AB}}{4 \cos^2 \gamma_1 \cos^2 \gamma_2} \left\{ \frac{\sqrt{D - E_v \sin^2 \varphi_0} + \sqrt{E_v} \cos \varphi_0}{\cos \theta \cdot m_C / (m_B + m_C)} - \frac{2\mu_{AB}}{m_B} \left[\sqrt{E_v} \cos \varphi_0 \cos \theta + \sqrt{E_r} \cos \beta \sin \theta \right] \right\}^2. \quad (3.6)$$

For diatom-diatom collision, the threshold function is,

$$F = \frac{\mu/\mu_{AB}}{4 \cos^2 \gamma_1 \cos^2 \gamma_2} \left\{ \frac{\sqrt{D - E_v \sin^2 \varphi_0} + \sqrt{E_v} \cos \varphi_0}{\cos \theta \cdot m_C / (m_B + m_C)} - \frac{2\mu_{AB}}{m_B} \left[\sqrt{E_v} \cos \varphi_0 \cos \theta + \sqrt{E_r} \cos \beta \sin \theta \right] - \frac{2\sqrt{\mu_{AB}\mu_{CD}}}{m_C} \left[\sqrt{E'_r} (\cos \delta \cos \beta_2 \sin \beta_1 + \sin \delta \sin \beta_2) - \sqrt{E'_v} \cos \varphi_1 \cos \beta_1 \cos \beta_2 \right] \right\}^2. \quad (3.7)$$

The derivations of Eqs. 3.6 and 3.7 are based on the assumption that collisions are close to the impulsive limit. However, it should be noted that the results do not obey the conservation of angular momentum, as the rotational energy E_r changes after the collision, but the bond length of AB molecule stays the same. To resolve this issue, we neglect the contribution of E_r to the collision, i.e. set E_r equals to zero in Eqs. 3.6 and 3.7, but change the dissociation energy from D to an effective value, D_{eff} . A

model potential energy curve (PEC) for diatomic molecule is shown in Fig. 3.3. It can be found that the effective dissociation energy should be calculated as,

$$D_{ef} = D - E_r + \delta E_r, \quad (3.8)$$

where δE_r is the centrifugal barrier. For the simplest exp-6 potential energy curve $V(r) = -2D(R_{eq}/r)^6$, where R_{eq} is the equilibrium distance of molecular bond and r is the internuclear distance, the effective dissociation energy can be calculated as,

$$D_{ef} = D - E_r + \frac{2E_r^{3/2}}{3\sqrt{6D}}. \quad (3.9)$$

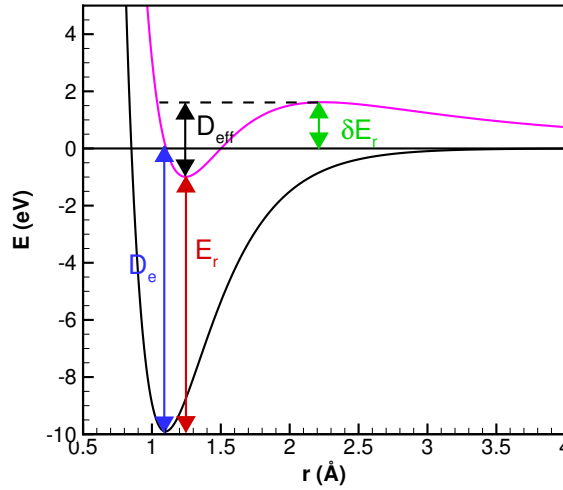


Figure 3.3. Model potential energy curve

The final expressions of threshold functions for diatom-atom and diatom-diatom collisions are:

$$F = \frac{\mu/\mu_{AB}}{4 \cos^2 \gamma_1 \cos^2 \gamma_2} \left[\frac{\sqrt{D_{ef} - E_v \sin^2 \varphi_0} + \sqrt{E_v} \cos \varphi_0}{\cos \theta \cdot m_C / (m_B + m_C)} - \frac{2\mu_{AB}}{m_B} \sqrt{E_v} \cos \varphi_0 \cos \theta \right]^2, \quad (3.10a)$$

$$F = \frac{\mu/\mu_{AB}}{4 \cos^2 \gamma_1 \cos^2 \gamma_2} \left\{ \frac{\sqrt{D_{ef} - E_v \sin^2 \varphi_0} + \sqrt{E_v} \cos \varphi_0}{\cos \theta \cdot m_C / (m_B + m_C)} - \frac{2\mu_{AB}}{m_B} \sqrt{E_v} \cos \varphi_0 \cos \theta \right. \\ \left. - \frac{2\sqrt{\mu_{AB}\mu_{CD}}}{m_C} \left[\sqrt{E'_r} (\cos \delta \cos \beta_2 \sin \beta_1 + \sin \delta \sin \beta_2) - \sqrt{E'_v} \cos \varphi_1 \cos \beta_1 \cos \beta_2 \right] \right\}^2. \quad (3.10b)$$

It should be noted that, for diatom-diatom colliding pairs like O_2+N_2 , there are more than one possible dissociation reaction pathways. With the same definitions of generalized coordinates in Fig. 3.2, we derive the threshold function for the dissociation of CD molecule as well,

$$F' = \frac{\mu/\mu_{CD}}{4 \cos^2 \gamma_1 \cos^2 \gamma_2} \left\{ \frac{\sqrt{D'_{ef} - E'_v \sin^2 \varphi_1} + \sqrt{E'_v} \cos \varphi_1}{\cos \beta_1 \cos \beta_2 \cdot m_B / (m_B + m_C)} \right. \\ \left. - \frac{2\mu_{CD}}{m_C} \sqrt{E'_v} \cos \varphi_1 \cos \beta_1 \cos \beta_2 \right. \\ \left. + \frac{2\sqrt{\mu_{AB}\mu_{CD}}}{m_B} \left[\sqrt{E_r} \cos \beta \sin \theta + \sqrt{E_v} \cos \varphi_0 \cos \theta \right] \right\}^2, \quad (3.11)$$

where D'_{ef} is the effective dissociation energy of molecule BC and β is an additional angle describing the direction of rotational velocity of AB molecule. The angle β doesn't influence the dissociation of molecule AB as the rotational velocity is perpendicular to the molecular bond.

For the most common case of a homonuclear molecule ($m_A = m_B = m$) being dissociated by an energetic atom ($m_C = M$), we can define a mass fraction $\alpha = (m/(M + m))^2$. The threshold function is then reduced to,

$$F = \frac{1 - \sqrt{\alpha}}{(1 + \sqrt{\alpha}) \cos^2 \gamma_1 \cos^2 \gamma_2} \\ \times \left(\frac{\sqrt{D_{ef} - E_v \sin^2 \varphi_0} + \sqrt{E_v} \cos \varphi_0}{(1 - \sqrt{\alpha}) \cos \theta} - \sqrt{E_v} \cos \theta \cos \varphi_0 \right)^2 \quad (3.12)$$

3.3 Macheret-Fridman Model for CFD

3.3.1 Derivation of the Model

To develop MF formulas for CFD, i.e. multi-temperature reaction rate coefficients and vibrational-dissociation energy exchange, we need to first calculate the probability of dissociation as a function of collision energy and internal energy, and then integrate the probability with appropriate energy distribution functions. For the simple case of diatom-atom collision, the probability of dissociation is calculated as,

$$P(E_t, E_r, E_v) = \frac{\oint_{E_t \leq F(E_r, E_v)} d\gamma_1 d\gamma_2 d\theta d\varphi_0}{\int_{\gamma_1} \int_{\gamma_2} \int_{\theta} \int_{\varphi_0} d\gamma_1 d\gamma_2 d\theta d\varphi_0}. \quad (3.13)$$

The integration in Eq. 3.13 can only be calculated approximately with Taylor expansion of the threshold function near the optimum configuration. The optimum configuration with the minimum threshold energy can be calculated by setting all the partial derivatives of the threshold function to 0. For diatom-atom collisions, the result is:

$$\begin{aligned} \gamma_1 = \gamma_2 = \theta = 0, \\ \cos \varphi = \begin{cases} -1, & \text{if } E_v \leq \alpha D_{ef} \\ -\left(\frac{\alpha}{1-\alpha} \frac{D_{ef} - E_v}{E_v}\right)^{1/2}, & \text{if } E_v > \alpha D_{ef} \end{cases}, \end{aligned} \quad (3.14)$$

The threshold function now reduces to a threshold line F , which only depends on the pre-collision vibrational energy:

$$F(E_v) = \begin{cases} \frac{(\sqrt{D_{ef}} - \sqrt{\alpha E_v})^2}{1-\alpha}, & \text{if } E_v \leq \alpha D_{ef} \\ D_{ef} - E_v, & \text{if } E_v > \alpha D_{ef} \end{cases} \quad (3.15)$$

The probability of dissociation can then be obtained based on Taylor expansion of threshold function near the optimum configuration. If we expand the threshold function to the second order,

$$E_t = F(E_v) + \frac{G_{\gamma_1, \gamma_1}}{2} \cdot \Delta\gamma_1^2 + \frac{G_{\gamma_2, \gamma_2}}{2} \cdot \Delta\gamma_2^2 + \frac{G_{\theta, \theta}}{2} \cdot \Delta\theta^2 + \frac{G_{\varphi, \varphi}}{2} \cdot \Delta\varphi^2. \quad (3.16)$$

The envelope $S(\gamma_1, \gamma_2, \theta, \varphi)$ with the threshold energy equal to E_t forms a n -dimensional ellipsoid and its volume $V(E_t, E_v)$ can be calculated. Then the probability of reaction is determined by the ratio of $V(E_t, E_v)$ to the volume of the entire accessible phase space corresponding to the full range of variation of the angular and phase variables. The complete expressions for the second order derivatives were listed in Ref. 101. Minor numerical errors were found in the Eqs. 17 and 25 in Ref. 101 and corrected in this work. The final probability of reaction with corrections is,

$$P = \begin{cases} \frac{4(E_t - F)^{3/2}}{\frac{3\pi^2 F \sqrt{D_{ef}}}{\sqrt{1 - \alpha}} \times \sqrt{\left(1 - \sqrt{\frac{\alpha E_v}{D_{ef}}}\right) \left[1 - (2 - \sqrt{\alpha}) \sqrt{\frac{E_v}{D_{ef}}}\right]}}, & \text{if } E_v \leq \alpha D_{ef} \\ \frac{(E_t - F)^2}{\frac{2\pi^2 F D_{ef} \sqrt{\alpha}}{\sqrt{(1 + \sqrt{\alpha})/(1 - \sqrt{\alpha})}} \sqrt{\left(1 - \frac{E_v}{D_{ef}}\right) \left(\frac{E_v}{\alpha D_{ef}} - 1\right)}}, & \text{if } E_v > \alpha D_{ef} \end{cases} \quad (3.17)$$

The reaction probability has been implemented in DSMC by Boyd [96] as well as Wadsworth and Wysong [105]. However, due the mathematical approximations, the formula has singularities for collisions with certain values of energy. The model also yields a reaction probability greater than unity under certain conditions, resulting in the need for rather artificial cut-off procedure. Moreover, the implementation limited to diatom-atom collision. The new DSMC model proposed in Sec. 3.4 resolves these issues.

Multi-temperature reaction rates coefficients can then be calculated by integrating the probability with distribution functions of translational, rotational and vibrational energy. To keep consistent with basic assumptions in CFD, Maxwell-Boltzmann distribution functions are used. However, it should be noted that dissociation reaction favors high vibrational levels and thus depletes their population, making the vibrational energy distribution deviate from Boltzmann distribution. It is important to note that the MF model analyzes the energy transformation in reactions and calculates the energy threshold and the probability of dissociation assuming that the collision has occurred. Thus, in order to obtain the rate coefficient of dissociation,

the dissociation probability calculated by the model should be multiplied by the “total” rate coefficients; such total collisional rate coefficients should be taken from sources other than the model itself., we do not attempt to calculate the total collisional rates $k_{coll}(T)$ for the CFD model. Instead, we focus on the nonequilibrium factor $Z = k(T, T_v)/k(T)$, i.e. on the behavior of the dissociation rate in thermally nonequilibrium conditions normalized by its thermally equilibrium (Arrhenius) value,

$$k(T) = AT^n \exp\left(-\frac{D}{T}\right), \quad (3.18)$$

where the dissociation energy D in this equation and in the subsequent Eqs. 3.21-3.27 is in Kelvin. Accordingly, we use the condition $k(T = T_r = T_v) = k(T)$. In such context, the multi-temperature rates are calculated as

$$k(T, T_v, T_r) = k_{coll}(T) \int_{E_v} \int_{E_t=F}^{+\infty} \int_{E_r} P \cdot f_{T_r}(E_r) dE_r f_T(E_t) dE_t f_{T_v}(E_v) dE_v. \quad (3.19)$$

The extreme complexity of the reaction probability in Eq. 3.17 precludes the direct analytical integration in Eq. 3.19, and we use the same approximations as those employed in Ref. 101. Specifically, the two-temperature rate coefficient is the sum of contributions from low, $E_v \leq \alpha D_{ef}$, and high, $E_v > \alpha D_{ef}$, vibrational levels:

$$k(T, T_v) = k_l + k_h. \quad (3.20)$$

A simple version of the steepest descend method can be applied to calculate the rates for $E_v \leq \alpha D_{ef}$. The method approximates the pre-exponential factor by its value in the vicinity of the exponent’s maxima. In the derivations, minor numerical errors were found in the Eqs. (34) and (35) in Ref. 101 and in the description of the Macheret-Fridman model in Ref. 104 and corrected here. The two-temperature rate coefficients for dissociation from low vibrational states with the corrections are:

$$k_l(T, T_v) = AT^n \times L \exp\left(-\frac{D}{T_a} + \Delta D \left(\frac{1}{T_a} - \frac{1}{T}\right)\right), \quad (3.21)$$

$$L = \frac{\sqrt{1-\alpha}}{\pi^{3/2}} \sqrt{\frac{D}{D^*}} \left(\frac{T}{D}\right)^{1-n} \left(1 + \frac{5(1-\alpha)T}{2D^*}\right) \left(12\pi b\alpha(1-\alpha)\frac{D}{T}\right)^{1/2}, \quad (3.22)$$

where T_a is the average temperature:

$$T_a = \alpha T_v + (1 - \alpha)T \quad (3.23)$$

D^* is the approximated value of D_{ef} in Eq. 3.9 (assuming small value of α , which is usually the case),

$$D^* = D - \Delta D = D - 3b\alpha^2 D, \quad (3.24)$$

and AT^n is the pre-exponential factor of the Arrhenius equilibrium dissociation rates obtained from experimental measurements or *ab-initio* calculations. For $E_v > \alpha D_{ef}$, the probability of dissociation has singularities at $E_v \rightarrow \alpha D_{ef}$ and $E_v \rightarrow D$, resulting from the approximation of threshold function by Taylor expansion. Instead of removing the singularities, it can be assumed that dissociation mainly occurs from highest vibrational levels and the rates are proportional to the nonequilibrium-to-equilibrium population ratio. Thus, the rates become:

$$k_h(T, T_v) = AT^n \times (1 - L) \frac{1 - \exp(-h\nu/T_v)}{1 - \exp(-h\nu/T)} \exp\left(-\frac{D}{T_v}\right), \quad (3.25)$$

where ν is the vibrational frequency of the dissociating molecule. The average vibrational energy removed by dissociation reaction is:

$$E_{v,rem} = \frac{(\alpha D^* \times (T_v/T_a)^2) \cdot k_l + D \cdot k_h}{k_l + k_h} \quad (3.26)$$

The two-temperature dissociation rates for diatom-diatom collisions can also be calculated with Eqs. 3.20-3.25, except that the function L should be calculated with the following formula rather than with Eq. 3.22:

$$L = \frac{2(1 - \alpha)}{\pi^2 \alpha^{3/4}} \left(\frac{D}{D^*}\right) \left(\frac{T}{D}\right)^{3/2-n} \left(1 + \frac{7(1 - \alpha)(1 + \sqrt{\alpha})T}{2D^*}\right) \left(12\pi b\alpha(1 - \alpha)\frac{D}{T}\right)^{1/2} \quad (3.27)$$

Numerical errors introduced by the approximate calculations of the probabilities in Eq. 3.17 as well as by the approximate integration that results in Eqs. 3.20-3.27 will be assessed in the following DSMC version of the thermal nonequilibrium dissociation reaction model, which uses the same assumption of classical impulsive limit but does not rely on the numerical approximations.

3.3.2 Validation of the Model

We now focus on the comparison of two-temperature reaction rates predicted by the model with the latest QCT calculations or experimental measurements. Two versions of the MF model are considered. One is the original simplified version included in the book [104]. It neglects the influence of pre-collision rotation of the dissociating molecule, which corresponds to Eqs. 3.20-3.27 with $\Delta D = 0$ (i.e. $D^* = D$) and without the factor $\left(12\pi b\alpha(1-\alpha)\frac{D}{T}\right)^{1/2}$ in Eqs. 3.22 and 3.27. The factor comes from the integration of reaction probabilities over rotational energy distribution. The other one is the extended version corresponding to Eqs. 3.20-3.27. The models are accordingly denoted as ‘‘Macheret-Fridman S’’ and ‘‘Macheret-Fridman F’’ in the following figures.

The nonequilibrium factor Z defined as the ratio of two-temperature rates $k(T, T_v)$ and the equilibrium rates $k_{eq}(T)$ is compared here. There are few experimental measurements of the value. Losev et al.’s fit [106] of their experimentally measured N_2-N_2 dissociation rates [107] is the only one included here. For other systems, the nonequilibrium reaction rates are calculated from QCT data. For N_2+N [51], N_2+O [56] and O_2+O [54], the two-temperature rates are calculated from rovibrational state-specific dissociation rates with fully coupled rovibrational ladder,

$$k(T, T_v) = \frac{\sum_{v,J} n_J k(T, v, J) \exp\left(-\frac{E_v(v)}{k_B T_v}\right) \exp\left(-\frac{E_{rv}(v, J) - E_v(v)}{k_B T}\right)}{\sum_{v,J} n_J \exp\left(-\frac{E_v(v)}{k_B T_v}\right) \exp\left(-\frac{E_{rv}(v, J) - E_v(v)}{k_B T}\right)}. \quad (3.28)$$

For O_2+O_2 [108], the nonequilibrium factor is directly calculated from the probability of reaction $P(T, E_v)$ as the following:

$$Z(T, T_v) = \frac{\sum_v P(T, E_v) \exp(-E_v/k_B T_v)}{\sum_v P(T, E_v) \exp(-E_v/k_B T)}. \quad (3.29)$$

Bender et al. reported two-temperature rates of N_2+N_2 [58] systems for specific temperatures. Their results are shown as discrete symbols in the comparisons.

Figures 3.4, 3.5 and 3.6 show the comparison of nonequilibrium factor by the two versions of MF model with QCT calculations for $\text{N}_2 - \text{O}$ [56], $\text{N}_2 - \text{N}$ [51] and $\text{O}_2 - \text{O}$ [54] collisional dissociation. To keep consistency, all the equilibrium reaction rates (Eq. 3.18) used in the MF model were taken from QCT calculations listed in Table. 3.1.

Table 3.1.: Equilibrium chemical reaction rates

Reaction	A ($\text{cm}^3\text{mol}^{-1}\text{s}^{-1}$)	n	D (K)	Source
$\text{N}_2 + \text{O} \rightarrow \text{N} + \text{N} + \text{O}$	5.3802E+17	-0.4807	113,950	QCT [56]
$\text{N}_2 + \text{N} \rightarrow \text{N} + \text{N} + \text{N}$	4.0247E+18	-0.6996	113,200	QCT [51]
$\text{N}_2 + \text{N}_2 \rightarrow \text{N} + \text{N} + \text{N}_2$	2.71E+18	-0.6750	117,000	QCT [58]
$\text{O}_2 + \text{O} \rightarrow \text{O} + \text{O} + \text{O}$	2.50E+18	-0.5650	60,492	QCT [54]
$\text{O}_2 + \text{O}_2 \rightarrow \text{O} + \text{O} + \text{O}_2$	2E+21	-1.5	59,500	Empirical [27]

As seen in Figs. 3.4-3.6, the simplified model underpredicts the dissociation rates at vibrationally-cold condition by 1-2 orders of magnitude, whereas the extended version of the model shows very good agreement with QCT, especially since the uncertainty of QCT results at low vibrational temperature is a factor of 3 at best. The good accuracy of the full model that includes rotational effects versus the poor accuracy of the simplified model that ignores rotational energy underscores the critical role played by rotational energy in dissociation at low vibrational temperature [101, 103]. It is also found that the agreement of the full model with the QCT results becomes better at higher translational temperatures, in line with the expectation that the accuracy of the impulsive approximation improves with temperature. The two versions of the model predict similar results in vibrationally-hot conditions as the reaction rates are determined by molecules with high vibrational energy in this regime, i.e. $k_h \gg k_l$, and the formulas for k_h are similar for the two versions.

Figures 3.7 and 3.8 compare the full and simplified MF models with QCT results for $\text{N}_2 - \text{N}_2$ [58] and $\text{O}_2 - \text{O}_2$ [108] collisional dissociation. For $\text{N}_2 - \text{N}_2$ dissociation, Singh and Schwartzentruber’s algebraic interpolation formula [67] fitted to the QCT data and an algebraic fit to experimental measurements [109] are also presented. Although it might appear that for $\text{N}_2 - \text{N}_2$ dissociation (Fig. 3.7) both QCT and the full MF model diverge from the fit to experimental results at vibrational temperatures below 7,000-8,000 K, it must be kept in mind that the actual experimental data have been obtained at vibrational temperatures of at least 7,000-8,000 K, and simple extrapolation of those experimental results to low vibrational temperature would be incorrect. For ground-state oxygen molecule $\text{O}_2(^3\Sigma_g^+)$, three spin states are possible for $\text{O}_2 - \text{O}_2$ interaction, namely singlet, triplet and quintet states. Statistically, they have relative weights of 1/9, 3/9 and 5/9. QCT rates shown in Fig. 3.8 were calculated for quintet and singlet states based on the probability of reaction presented in Fig. 10 of Ref. 108 and they are compared with the rates given by MF model as normalized by the equilibrium rates proposed by Park. Again, given the factor of ~ 3 (or higher) estimated uncertainty of QCT in vibrationally-cold conditions, the agreement between the full MF model and QCT seen in Fig. 3.8 is very good.

In summary, we found that the full version of MF model provides very good predictions of nonequilibrium factors in vibrationally cold conditions. The agreement with QCT calculations becomes better at high translational temperature as the collision gets closer to the impulsive limit. The vibration-rotation coupling is seen to be very important in vibrationally-cold conditions, as the rotation lowers the effective dissociation energy (although not by the full rotational energy due to the “centrifugal barrier” stemming from the conservation of angular momentum). This effect, predicted in Refs. 103 and 101 and validated here, is quite consistent with the observations made in Ref. 58 from the QCT analysis. The simplified version of MF model that ignores this rotationally-induced reduction in dissociation threshold underestimates the rates by at least an order of magnitude for the cases considered. Therefore, we recommend using the full version of MF model in CFD calculations.

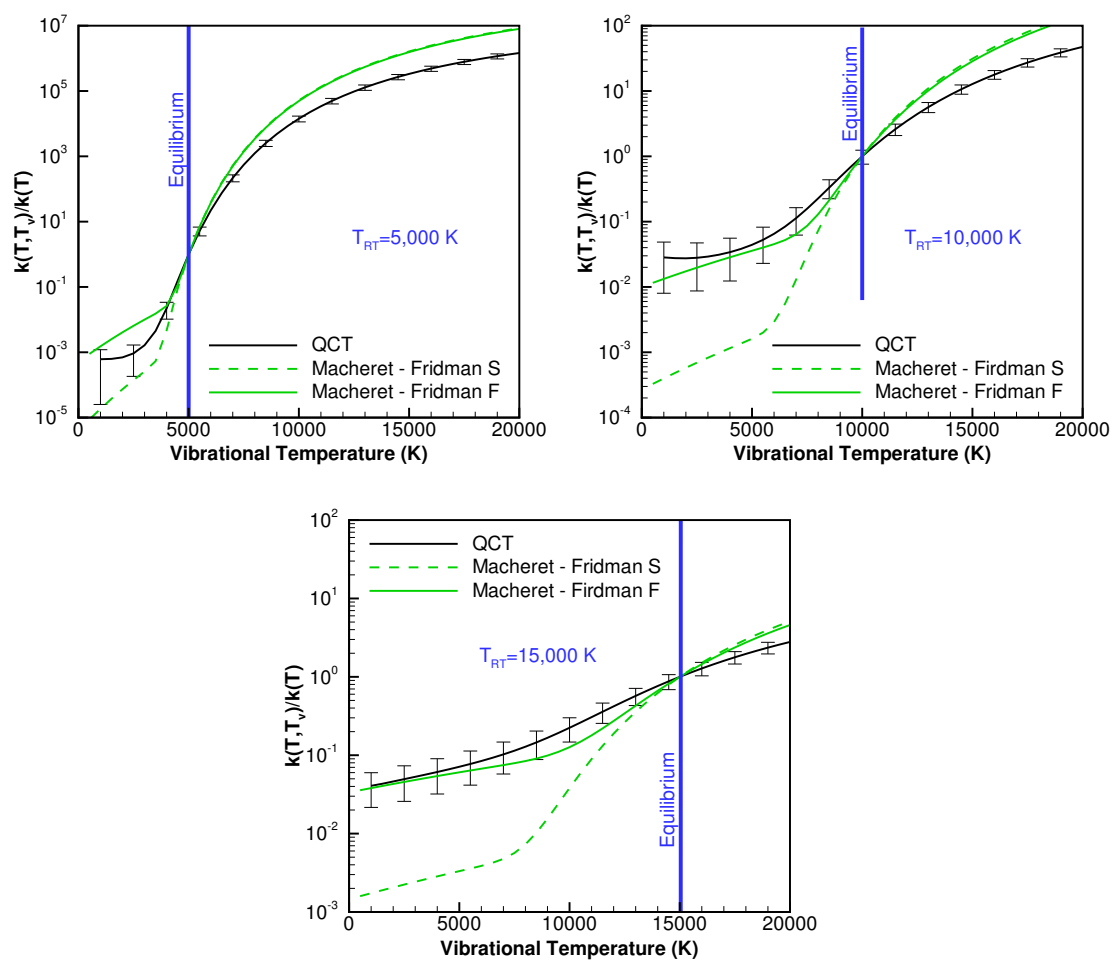


Figure 3.4. Nonequilibrium factor for $N_2 + O \rightarrow N + N + O$

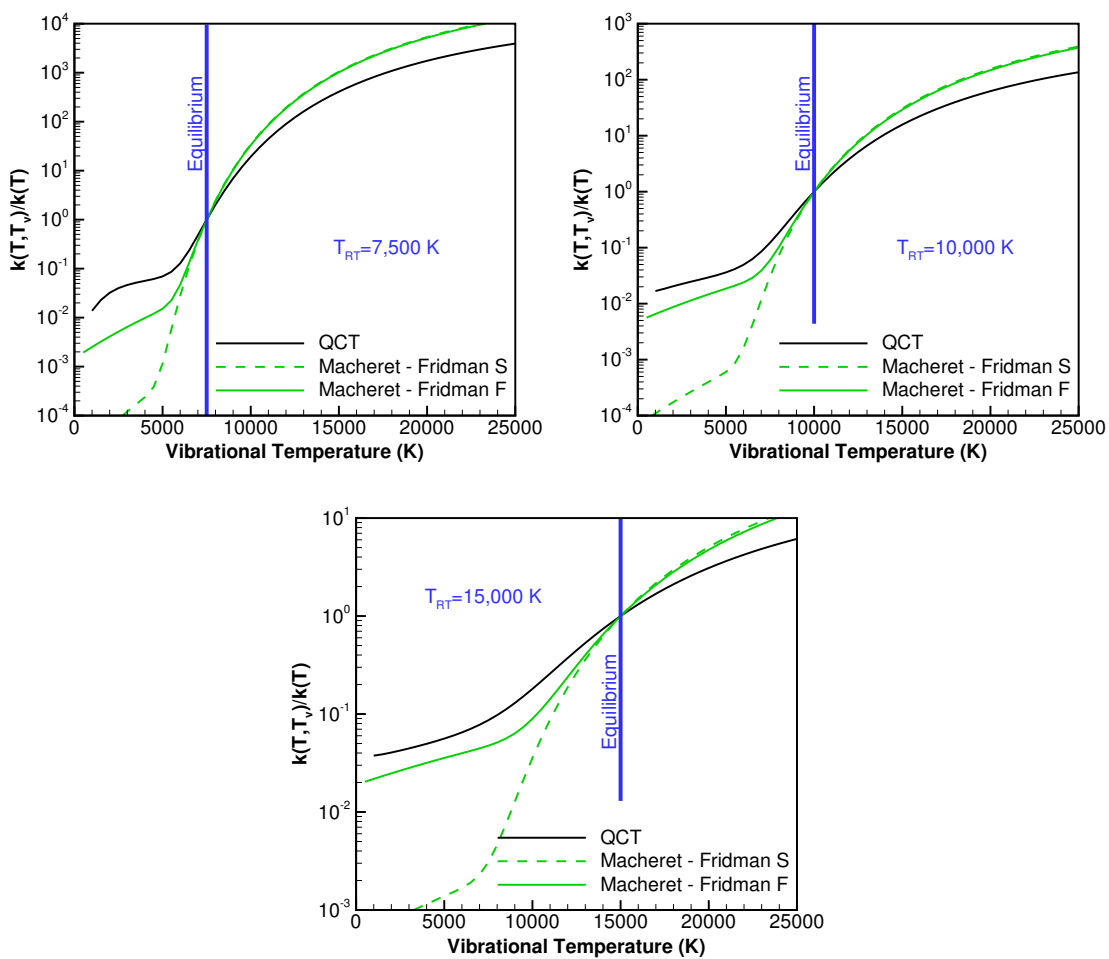


Figure 3.5. Nonequilibrium factor for $N_2 + N \rightarrow N + N + N$

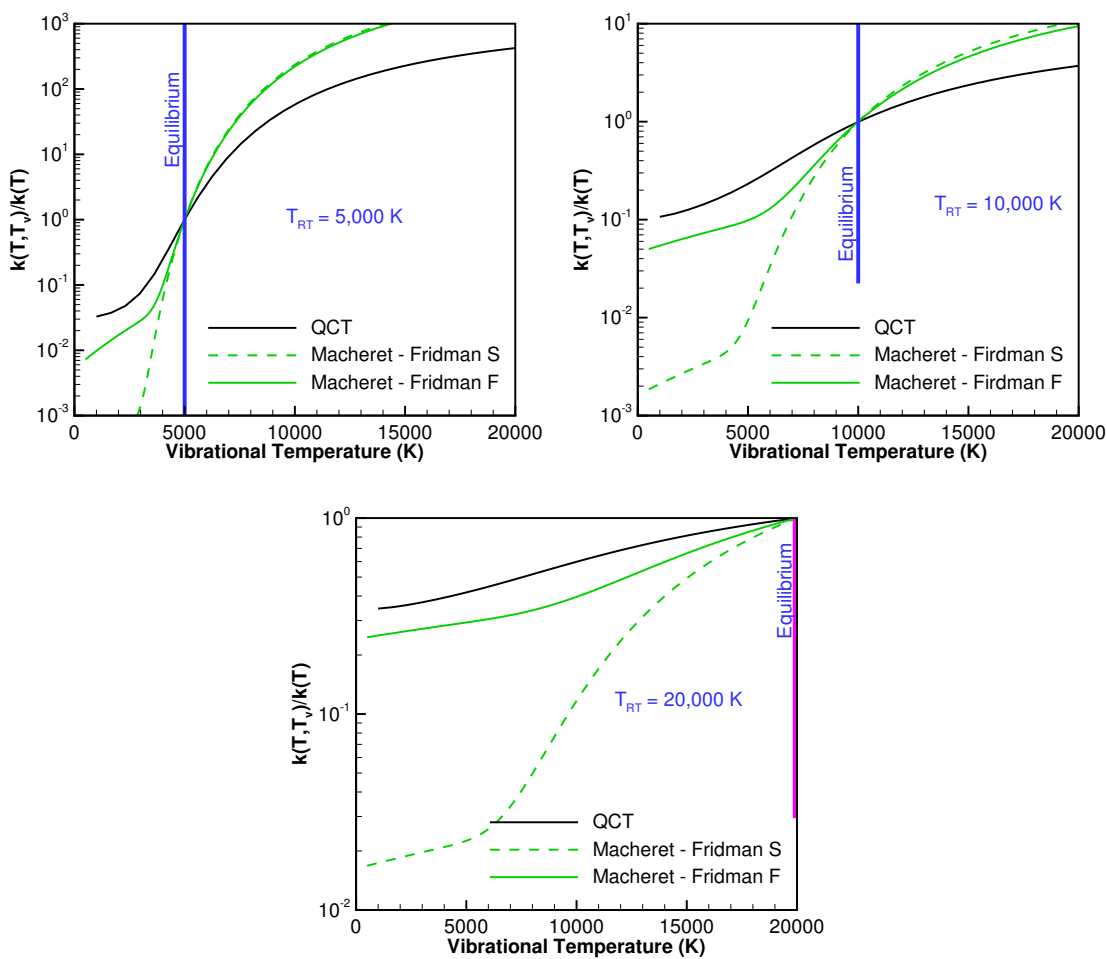


Figure 3.6. Nonequilibrium factor for $O_2 + O \rightarrow O + O + O$

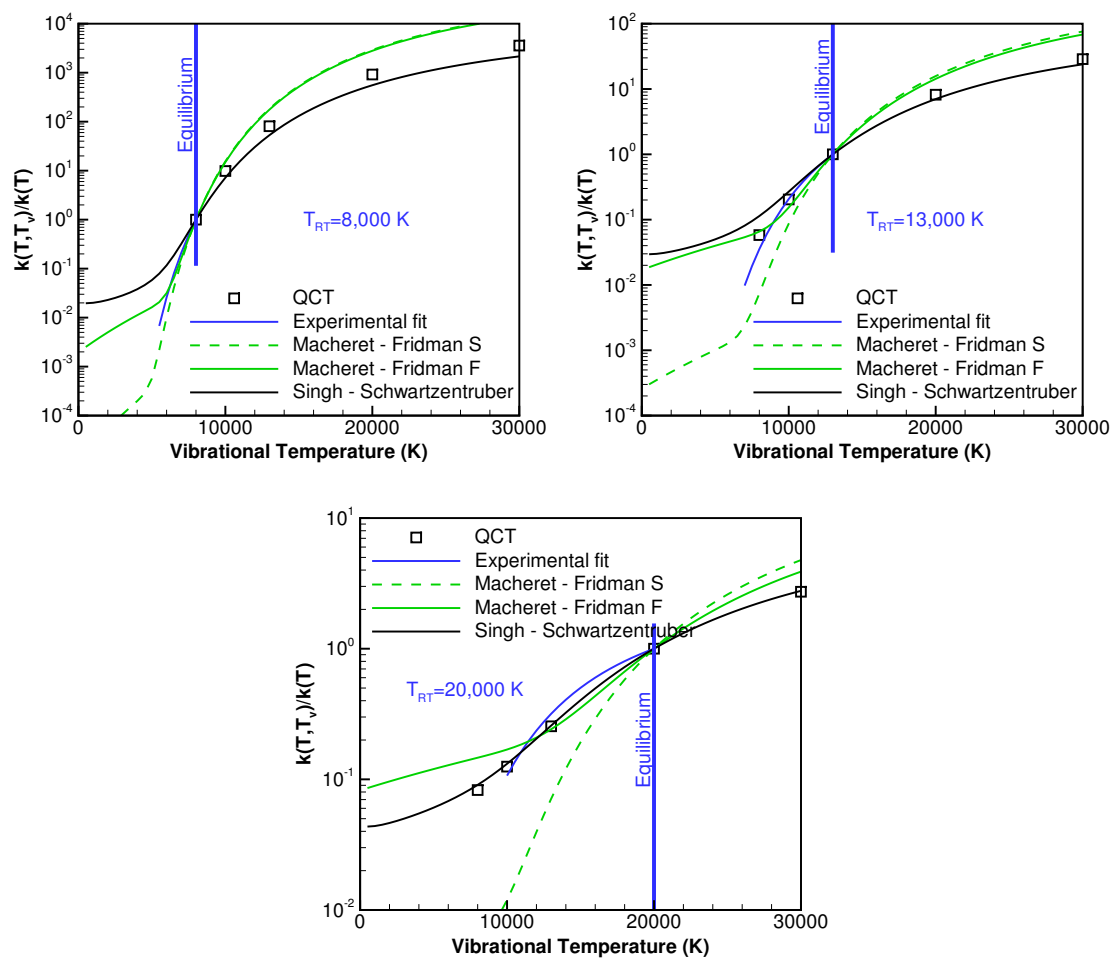


Figure 3.7. Nonequilibrium factor for $N_2 + N_2 \rightarrow N + N + N_2$

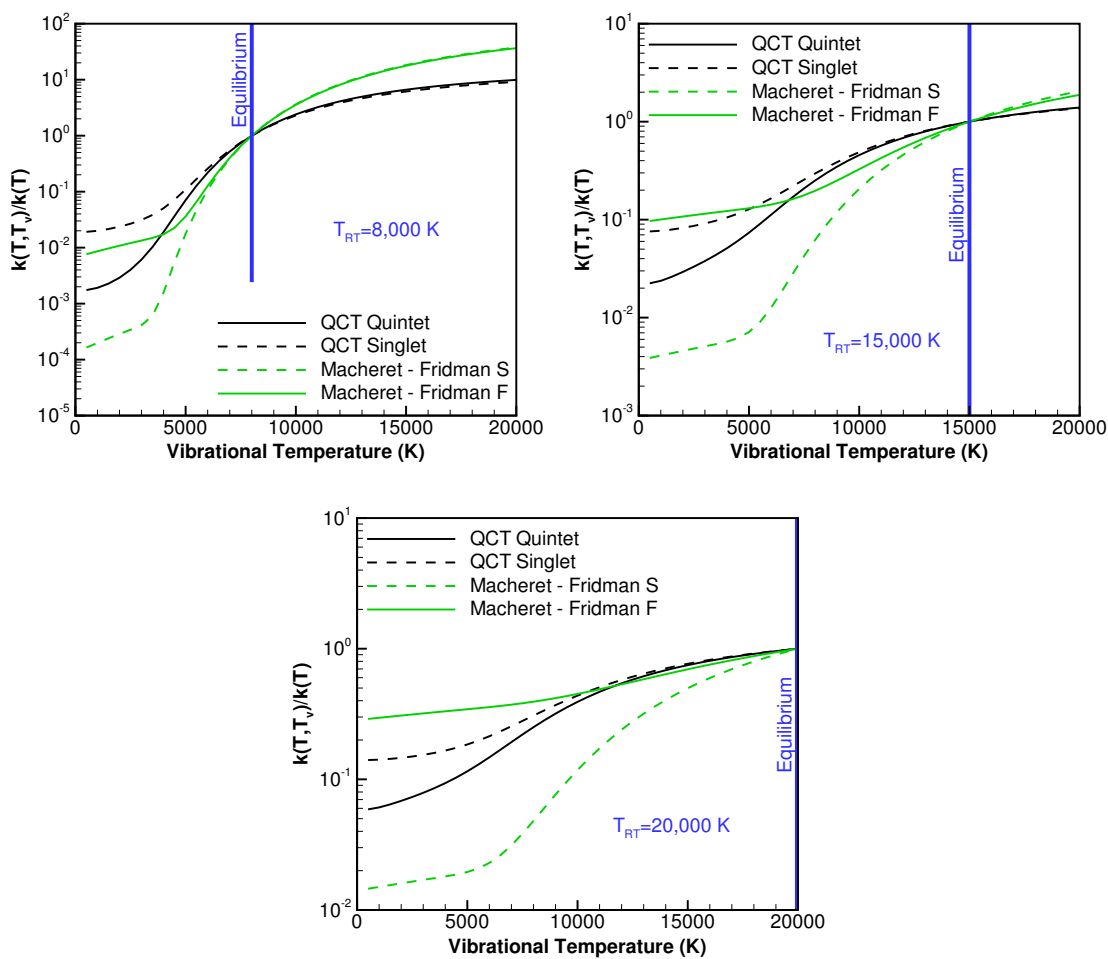


Figure 3.8. Nonequilibrium factor for $O_2 + O_2 \rightarrow O + O + O_2$

3.3.3 Simulation of O₂ Reacting Shock

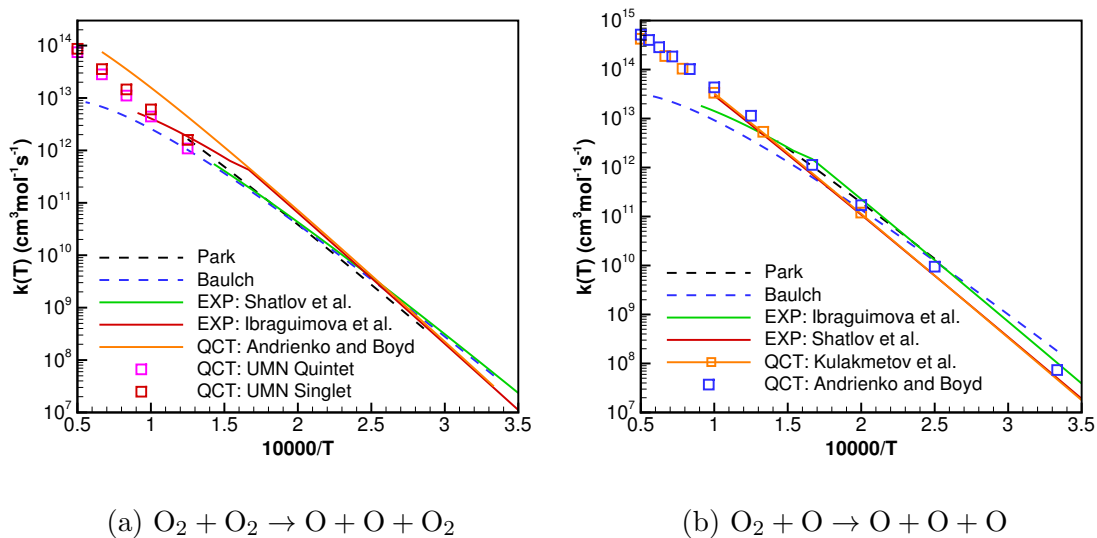
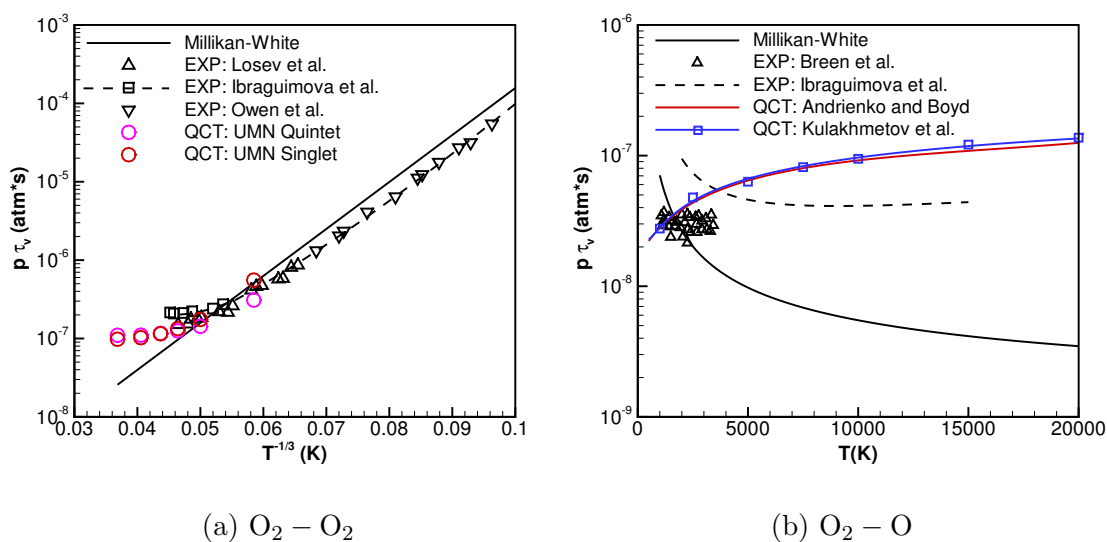
Ibraguimova et al. studied O₂ dissociation behind shocks at various experimental conditions [100, 110, 111]. Here we evaluate the use of full MF model (Eqs. 3.20-3.27) by simulating the Mach 11.9 and Mach 13.4 cases with two-temperature CFD. The freestream conditions are listed in Table. 3.2. We use a one-dimensional shock-wave solver, Poshax3 [112], to solve the Euler equations for the problem. The gas is assumed to be calorically perfect with constant specific heat of translational and rotational mode, $c_{v,TR}$. Vibrational energy is calculated by the harmonic oscillator model. There are two dissociation reactions ($O_2 + O_2 \rightarrow 2O + O_2$, $O_2 + O \rightarrow 3O$) and two V-T relaxation processes ($O_2 - O$, $O_2 - O$) in the system. Reaction rates and V-T relaxation time from different experimental measurements [33, 99, 100, 113–115] and QCT calculations [54, 108, 116] are compared in Fig. 3.9 and 3.10. All the data are for thermal equilibrium condition with the exception of the one from Grover and Schwartzentruber [108] (denoted as UMN) which is for quasi-steady state. Empirical interpolation/extrapolation formulas by Park [33], Baulch [28] and Millikan-White [117] are also plotted in the figures. In general, excluding Baulch’s interpolation/extrapolation, the reactions rates are very close to each other. The fitting formula proposed by Ibraguimova et al. [100] gives the best agreement of $O_2 - O_2$ relaxation time to with the experiments. The biggest difference is seen in Fig. 3.10 in the $O_2 - O$ relaxation time as QCT calculations predict a trend opposite to that given by the empirical Millikan-White formula. However, Ibraguimova et al.’s analysis based on their experiments gives a value closer to the QCT calculations.

Table 3.2.: Freestream conditions of O_2 reacting shock

Mach number	Pressure (Torr)	Shock speed (km/s)	Temperature (K)
11.9	1.0	3.98	298.5
13.4	0.8	4.44	298.5

Table 3.3.: Summary of simulation parameters

	Model 1	Model 2	Model 3	Model 4
$k(T)$: $O_2 - O_2$	Park	Andrienko and Boyd	Park	Park
$k(T)$: $O_2 - O$	Kulakhmetov et al.	Kulakhmetov et al.	Kulakhmetov et al.	Kulakhmetov et al.
$p\tau_v$: $O_2 - O_2$	Ibraguimova et al.	Ibraguimova et al.	Ibraguimova et al.	Millikan-White
$p\tau_v$: $O_2 - O$	Kulakhmetov et al.	Kulakhmetov et al.	Ibraguimova et al.	Kulakhmetov et al.

Figure 3.9. Chemical reaction rates for reactions in pure O_2 Figure 3.10. Vibrational-translational relaxation time of O_2 -O and O_2 - O_2

We have used different combinations of reaction rates and V-T relaxation time as listed in Table. 3.3 with the full version of Macheret-Fridman model (Eqs. 3.20-3.27). For the shock with Mach 13.4, the temperature profile, mass fraction of O_2 and den-

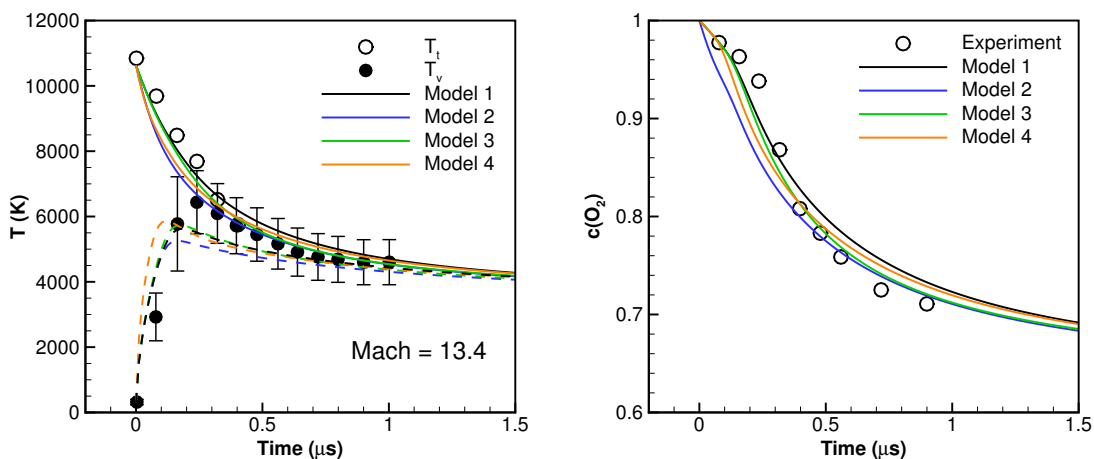
sity after the shock front are compared in Fig. 3.11. Experimental measurements are shown as circle symbols. CFD calculated temperatures are shown as solid lines for translational temperature and dashed lines for vibrational temperature in Fig. 3.11a. It can be seen that the model gives reasonable predictions for all the properties within the error bar. In particular, model 3 shows the best agreement for the mass fraction of O_2 . Note, however, the model somewhat underpredicts the peak vibrational temperature and overpredicts the overall time of thermal equilibration. The temperature profile at Mach 11.2 exhibits a similar behavior as shown in Fig. 3.12. One possible reason is the Boltzmann distribution of vibrational energy inherently assumed in CFD. In reality, high vibrational states are depleted by the dissociation, which slows the overall dissociation and reduces the mean vibrational energy spent on dissociation, thus potentially leading to a higher peak vibrational temperature. Another possible reason is overprediction of the mean vibrational energy removal in dissociation. Further investigation of this is in progress. Comparing the different simulation frameworks, we found that $O_2 - O_2$ dissociation reaction controls the shock structure right after the shock front (i.e. $t < 0.5 \mu s$) and $O_2 - O$ V-T relaxation influences the structure in the downstream (i.e. $t > 1 \mu s$). Due to the high concentration of O_2 right after the shock front, the position of peak vibrational temperature is mainly determined by $O_2 - O_2$ V-T relaxation.

3.3.4 Summary

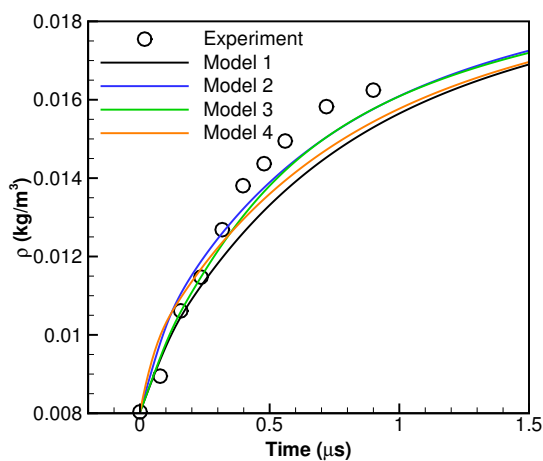
The principal findings can be summarized as follows.

First, the improved dissociation model based on classical impulsive approximation shows a very good agreement with QCT simulations for both diatom-atom and diatom-diatom collisions in vibrationally cold conditions and thus can be recommended for CFD.

The very good agreement between the classical impulsive models and QCT simulations suggests that the reaction dynamics at high temperature is not very sensitive



(a) Temperature

(b) Mass fraction of O_2 

(c) Density

Figure 3.11. Properties of gas behind the shock front for shock with Mach 13.4

to the details of PES. The collisions are close to the sudden (impulsive) limit, and the colliding molecules do not feel long-range interactions and three-body interactions before and after the collision.

Next, the reduction of dissociation energy due to rotation of the dissociating molecule and the emergence of centrifugal barrier are very important in vibrationally

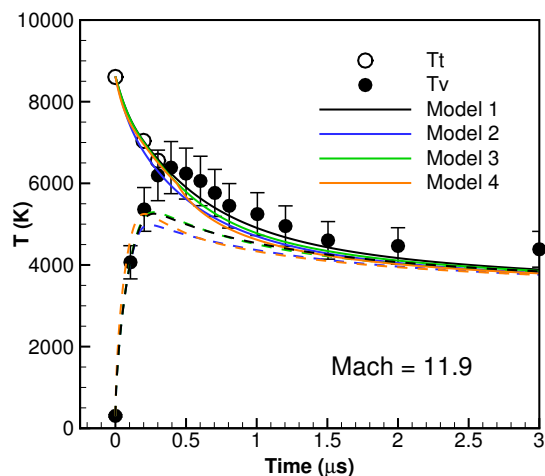


Figure 3.12. Temperature profile for shock with Mach 11.9

cold conditions (e.g. immediately behind strong shocks) but less significant closer to thermal equilibrium.

Finally, The classical impulsive dissociation model predicts O_2 reacting shock structure in reasonable agreement with the experimental measurements in strong shocks. However, there is some difference in the peak vibrational temperature, which could be due to non-Boltzmann vibrational distributions and to inaccuracies in calculation of the mean vibrational energy removal in dissociation. The DSMC version of the model is expected to resolve the issue.

3.4 Macheret-Fridman Model for DSMC

3.4.1 Introduction

As it is shown in Sec. 3.3.1, the derivation of MF model for CFD method uses several mathematical approximations in order to get closed-form formulas of reaction rates. The approximations reduce the accuracy of the model and limit its performance. Different from CFD, DSMC simulates molecular collisions and it needs low-level properties like reaction probabilities and reaction cross sections. Thus, the error due to the approximated integration of reaction probabilities over energy distribution function in Eq. 3.19 is eliminated. There were attempts to directly implement Eq. 3.17 in DSMC [96,105]. However, the implementation suffers from singularities of Eq. 3.17 at $E_v = \alpha D_{ef}$ and $E_v = D_{ef}$. The probability can also be larger than unity under certain conditions. All these issues are caused by the approximation of the integral in Eq. 3.13. Besides, the existing implementation is only able to model dissociation of homonuclear molecule impacted by atom, which significantly limits the applicability of the theory.

In the present work, instead of using the reaction probability calculated with Taylor expansion, we use a different technique. Because DSMC is a stochastic method, we can directly sample collision geometries required for the MF theory on the fly and use the threshold function to determine whether dissociation occurs. Since the threshold function is independent from collisional model, the ensemble average will then produce the correct reaction probabilities. The pseudo-code for the implementation of the model is list as the following,

1. Identify collisional type (atom-diatom or diatom-diatom) and number of possible dissociation reaction pathways
2. Generate phase angles $\gamma_1, \gamma_2, \beta_1, \beta_2, \theta, \varphi_0, \varphi_1, \theta, \delta, \beta$
3. Compute effective dissociation energy $D_{ef,i}$ with Eq. 3.8 for each dissociation reaction pathway i

4. Compute the corresponding threshold energy $F_i(E_v, E_r, E'_v, E'_r)$ with Eqs. 3.6 to 3.7
5. Select the reaction pathway i with the minimum threshold energy F_i
6. **If** $E_t \geq F_i$ **then** Reaction i occurs (i.e. $P_{j=i} = 1, P_{j \neq i} = 0$)
7. **Else** No dissociation occurs (i.e. $P_j = 0$)
8. **EndIf**

Making use of the periodicity of sinusoidal function, we sample phase angles $\gamma_1, \gamma_2, \beta_1, \varphi_0, \varphi_1$ uniformly between 0 to π and β_2, θ, δ between 0 to 2π .

It should be noted that, D_{ef} and the term $D_{ef} - E_v \sin^2 \varphi_0$ in Eqs. 3.10a and 3.10b may become less than 0 for certain values of energies of the colliding particles. This is due to the particular form of the potential energy curve used to derive D_{ef} . We have used a more realistic potential energy curve, i.e. the Morse potential, to remove this singularity, but found that the change in final results is not significant. Thus, a simple recipe is to make the reaction probability P equal to 1 when this condition occurs.

3.4.2 Validation of the Model

To validate the new MF-DSMC model, we implemented the model in a heavily modified DS1V code [36]. Standard no-time-counter (NTC) scheme is used. Elastic collisions are modeled according to variable hard sphere (VHS) model [36]. The reference diameter d_{ref} and viscosity index ω for different species are listed in Table 3.4. The VHS parameters for O_2 - O_2 , O_2 - N_2 and NO - N_2 are calibrated based on the collisional integrals calculated by Capitelli et al. for high-temperature air species [74]. Regarding the modeling of internal modes of N_2 , O_2 and NO , discrete vibrational energy model is used with continuous model for rotational energy. The vibrational ladders calculated in Refs. 53 and 56 are used in this work. All the calculations are

started at either thermal equilibrium ($T = T_r = T_v$) or nonequilibrium ($T = T_r \neq T_v$) conditions with Maxwell-Boltzmann distribution of collisional energy and internal energy. Unless stated otherwise, the vibrational temperature is numerically calculated by solving the equation,

$$\bar{E}_v = \frac{\sum_v E_v(v) \exp(-E_v(v)/k_b T_v)}{\sum_v \exp(-E_v(v)/k_b T_v)}, \quad (3.30)$$

where \bar{E}_v is DSMC calculated cell averaged vibrational energy and $E_v(v)$ is the vibrational energy of level v .

In order to isolate the influence of reaction models from the VT and RT energy relaxations, the Larsen-Borgnakke (LB) [118] thermal relaxation model with constant $Z_R = 1$ and $Z_V = 10^4$ is used. This ensures there is no energy transfer between translational and vibrational mode. To maintain the concentration of the species and make the system isothermal, dissociations are only tracked and molecules are not actually dissociated. A counter is set up to count number of reactions for the given temperatures and used to calculate reaction rates.

Table 3.4.: VHS parameters with $T_{ref} = 273$ K

	d_{ref} (Å)	ω (-)		d_{ref} (Å)	ω (-)
N ₂ -N [119]	3.585	0.770	O ₂ -O ₂	4.152	0.732
O ₂ -O [120]	3.442	0.750	O ₂ -N ₂	4.051	0.734
N ₂ -O [119]	3.814	0.750	O ₂ -N ₂	4.051	0.729
N ₂ -N ₂ [119]	4.170	0.740			

A very important feature of the MF model is that it calculates the probability of dissociation reaction provided that a collision occurs. Therefore, in order to calculate the total probability and rate of dissociation, one needs to multiply the MF probability by the rate of collisions which has to be taken from outside the MF model. For example, the rate of collisions can be calculated with VHS model or from matching

the thermally-equilibrium rate to the experimental or QCT data. In this context, we first validate the MF-DSMC model by comparing the nonequilibrium characteristics such as state-specific rates and nonequilibrium factors to the available data, and then examine the absolute dissociation rates that require knowledge of the collision rates.

3.4.2.1 Vibrational State-Specific Rates

Vibrational state-specific reaction rates for different colliding pairs are compared in Fig. 3.13 and 3.14. We assume that translational and rotational mode are in thermal equilibrium (i.e. $T = T_r$), then the rates can be calculated as the following,

$$k(T, E_v) = \frac{\sum_{J=0}^{J_{max}(v)} k(T, v, J) n_J \exp(-E_{rv}(v, J)/k_B T)}{\sum_{J=0}^{J_{max}(v)} n_J \exp(-E_{rv}(v, J)/k_B T)}, \quad (3.31)$$

where $k(T, v, J)$ is the QCT calculated rovibrational state-specific reaction rates, n_J is the product of nuclear spin and rotational degeneracy, $J_{max}(v)$ is the maximum rotational quantum number for vibrational state v and E_{rv} is the coupled rovibrational energy. Eq. 3.31 is used to calculate $k(T, E_v)$ for N_2+N [51], N_2+O [56] and O_2+O [54] systems. For NO dissociated by N, N_2 dissociated by O_2 and O_2 dissociated by N_2 , the rates are directly obtained from the papers [62, 63]. It should be noted that ground state $N_2(X^1\Sigma_g^+)$ and $O(^3P)$ correlate with three electronic states of N_2O but only two of them, namely $^3A''$ and $^3A'$ correlate with ground state atomic nitrogen in the dissociation reaction channel. For Fig. 3.13, we take the QCT results for both PESs and multiply the rates by the weight of each PES. To remove the effect of collision rates and to focus on MF-DSMC model itself, DSMC calculated rates are scaled in the following manner,

$$k_{MF-DSMC}^{Scale}(T, E_v) = k_{MF-DSMC}(T, E_v) \cdot \frac{k_{eq,QCT}(T)}{k_{eq,MF-DSMC}(T)}, \quad (3.32)$$

where $k_{eq,QCT}$ and $k_{eq,MF-DSMC}$ are the corresponding equilibrium dissociation rates predicted by QCT method and MF-DSMC model. For O_2 dissociated by O_2 , there

are DMS calculated probabilities of dissociation $P_{DMS}(T, E_v)$ [108] but the collision rates are unknown. Since the collision rate $k_{coll}(T)$ is independent of vibrational level, we have

$$\frac{k(T, E_v)}{k_{eq}(T)} = \frac{k_{coll}(T)P(T, E_v)}{\sum_{v=0}^{v=v_{max}} k_{coll}(T)P(T, E_v) \exp(-E_v/k_B T)} = \frac{P(T, E_v)}{\sum_{v=0}^{v=v_{max}} P(T, E_v) \exp(-E_v/k_B T)}. \quad (3.33)$$

Therefore, we compare the following scaled probability of reaction for O_2+O_2 system with the DMS calculated values,

$$P_{MF-DSMC}^{Scale}(T, E_v) = P_{MF-DSMC}(T, E_v) \cdot \frac{\sum_{v=0}^{v=v_{max}} P_{DMS}(T, E_v) \exp(-E_v/k_B T)}{\sum_{v=0}^{v=v_{max}} P_{MF-DSMC}(T, E_v) \exp(-E_v/k_B T)}. \quad (3.34)$$

As seen in Figs. 3.13 and 3.14, there is a good agreement of MF-DSMC vibrational state-specific reaction rates with QCT and DMS ones for most systems investigated here. The MF-DSMC model correctly captures the linear dependence of $\log(k(T, E_v))$ on vibrational energy and also the relationship between the slope of the logarithm of the rates and translational temperature T . For N_2+O system, the model predicts rates almost identical to the QCT results multiplied by the electronic degeneracy factor. The agreement improves with increasing temperature, which confirms the expectation that collision dynamics are weakly sensitive to the details of PES at high temperature and high energy collisions. The model fails to correctly predict the non-linear part of vibrational state-specific rates for very high vibrational states because it assumes harmonic vibrations. The probability density functions of normalized internuclear distance for N_2 molecule with different values of vibrational energy are compared in Fig. 3.15. Compared to harmonic oscillator (HO), the actual particles spend more time at the outer turning point, which is the preferential phase angle for dissociation [101]. Thus, the HO assumption results in underestimation of the dissociation rates and probabilities for molecules with high vibrational energy. The MF-DSMC-AHO model presented in Sec. 3.4.4 will improve those rates by incorporating the effect of anharmonic oscillation. It should be noted that, the issue becomes

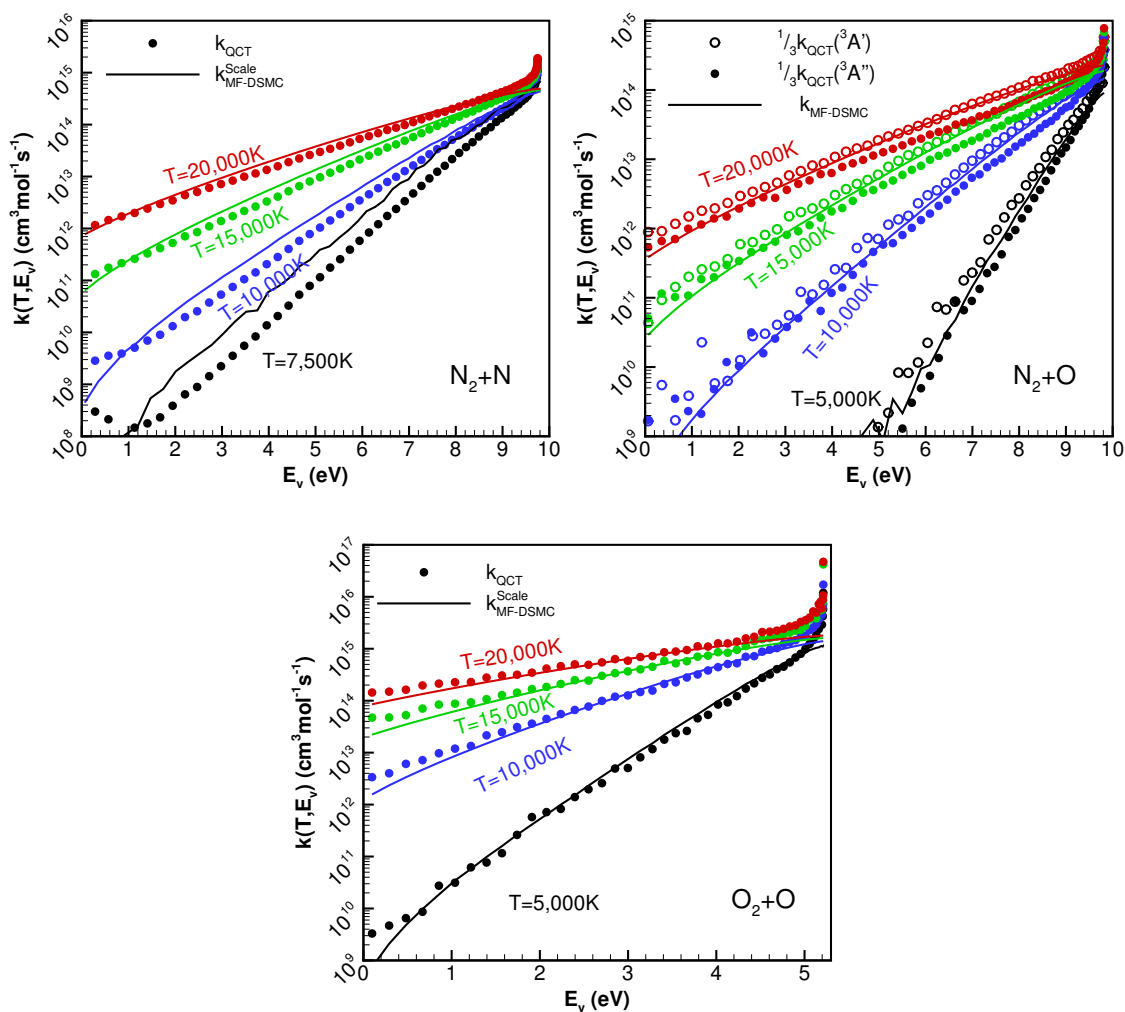


Figure 3.13. Comparison of vibrational state-specific rates calculated by QCT method and MF-DSMC model for atom-diatom collision. MF-DSMC rates for $\text{N}_2 + \text{N}$ and $\text{O}_2 + \text{O}$ are scaled.

less significant for either high translational temperature or low vibrational temperature because of the increasing contributions from molecules with low vibrational energy.

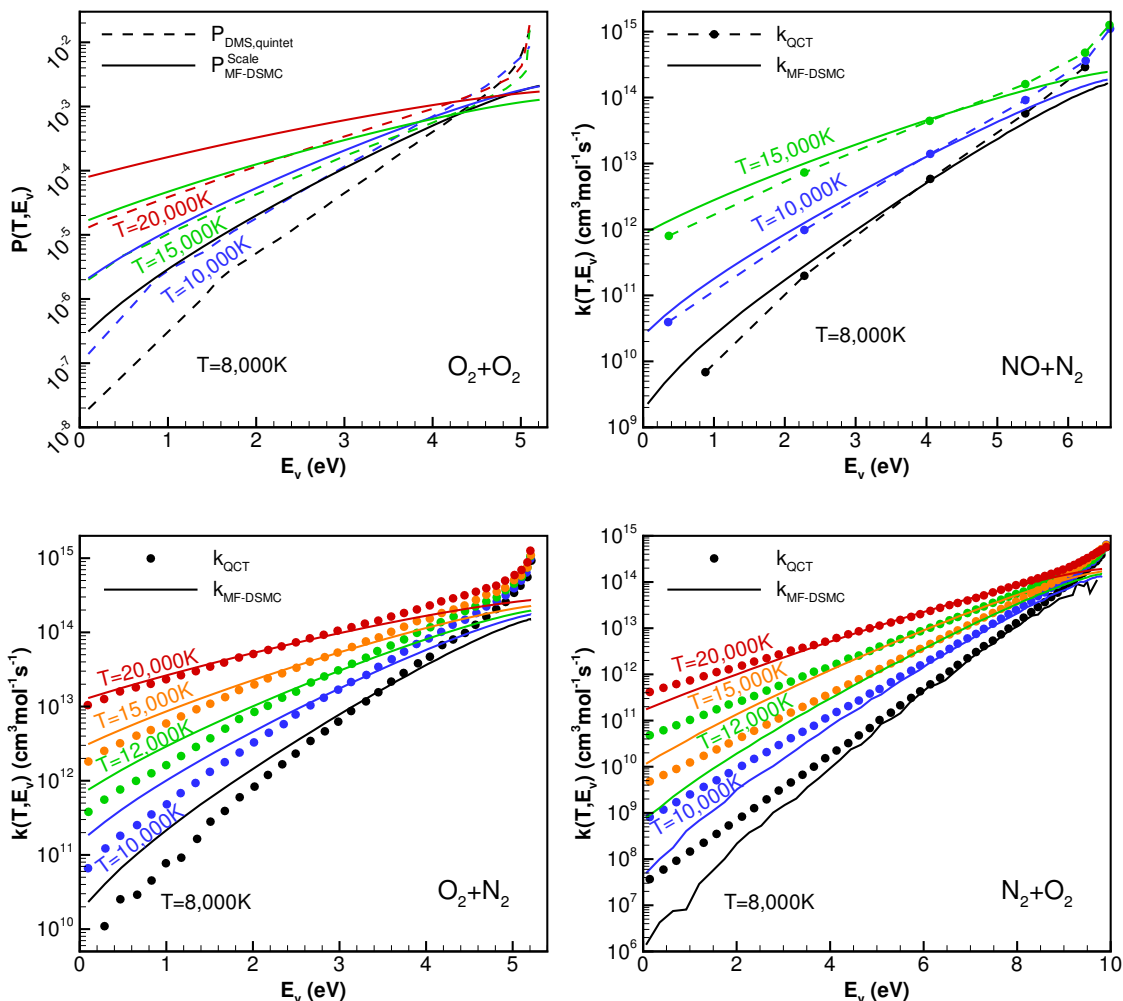


Figure 3.14. Comparison of vibrational state-specific rates calculated by QCT method and MF-DSMC model for diatom-diatom collisions. MF-DSMC rates for $\text{O}_2 + \text{O}_2$ are scaled.

3.4.2.2 Nonequilibrium Factors

Although not directly used in DSMC, multi-temperature reaction rates are crucial in nonequilibrium CFD simulations. For flow conditions like shock wave or expansion fan, strong deviations from thermal equilibrium result in several orders of magnitude difference in reaction rates and heat transfer. Comparison of nonequilibrium two-

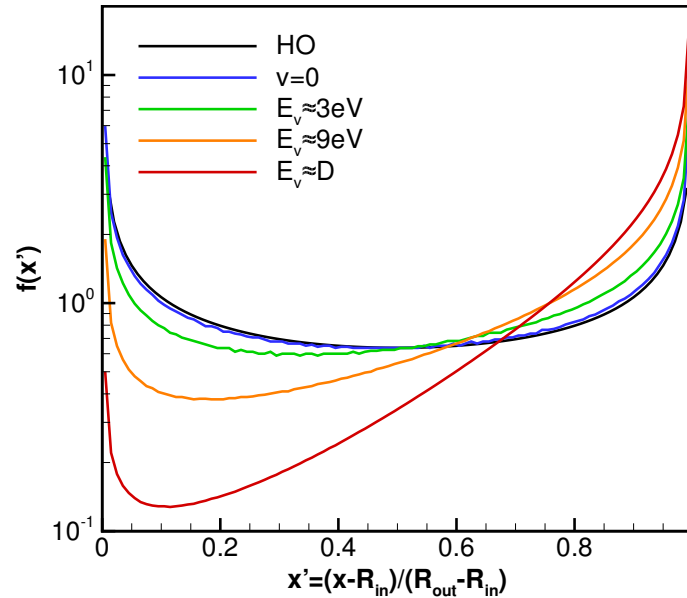


Figure 3.15. Probability density functions of internuclear distance for N_2 molecule at different values of vibrational energy

temperature reaction rates generated with MF-DSMC to those calculated by QCT or obtained from experiments can help evaluate the model consistently.

Similar to the validation of MF-CFD model in Sec. 3.3.2, we compare the nonequilibrium factors calculated by MF-DSMC model with available QCT data. Two additional dissociation reactions, N_2 dissociated by O_2 and O_2 dissociated by N_2 are added here. Andrienko et al. reported vibrational state-specific rates [62] and corresponding two-temperature rates are calculated as the following,

$$k(T, T_v) = \frac{\sum_v k(T, v) \exp(-E_v(v)/k_B T_v)}{\sum_v \exp(-E_v(v)/k_B T_v)}. \quad (3.35)$$

Chaudhry et al. reported two-temperature rates of N_2+O_2 [121, 122] systems for specific temperatures. Their results are shown as discrete symbols in the comparisons. In addition, the nonequilibrium factors calculated analytically with the extended version of MF-CFD model presented in Sec. 3.3 are also compared here.

The comparison of nonequilibrium factors is shown in Figs. 3.16-3.22. Overall, the results predicted with MF-DSMC model and QCT calculations match closely. Compared to the original two-temperature MF model, the agreement is especially better at vibrationally hot conditions. The difference between MF-DSMC model and QCT data is negligible for N_2+N and N_2+N_2 systems. For vibrationally cold condition, the nonequilibrium factor calculated from MF-DSMC model agrees with QCT data quite well, especially considering the uncertainty of QCT calculations (with the error bars illustrated in Fig. 3.18). For weakly nonequilibrium condition with $|T - T_v|/T \leq 20\%$, the differences are within a factor 2 for most systems investigated here.

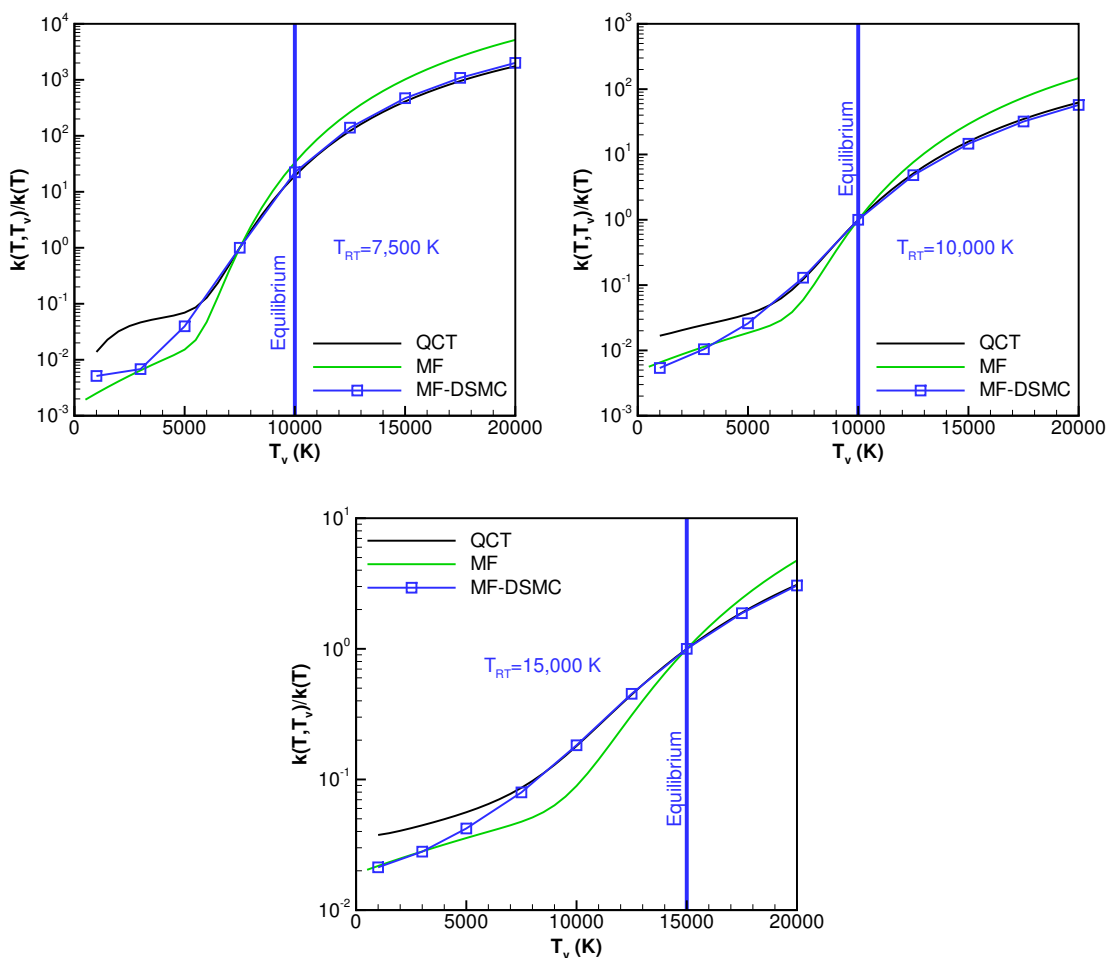


Figure 3.16. Nonequilibrium factor for $N_2 + N \rightarrow N + N + N$

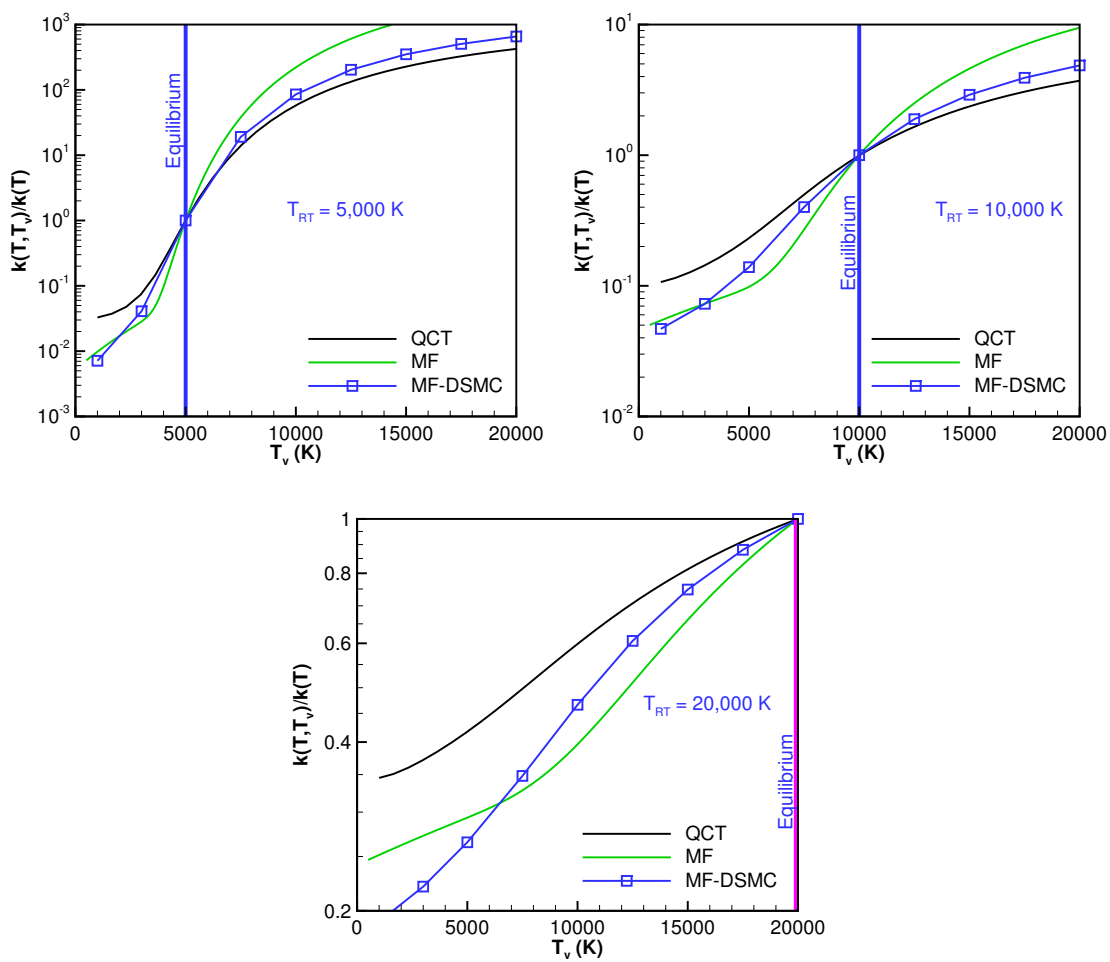
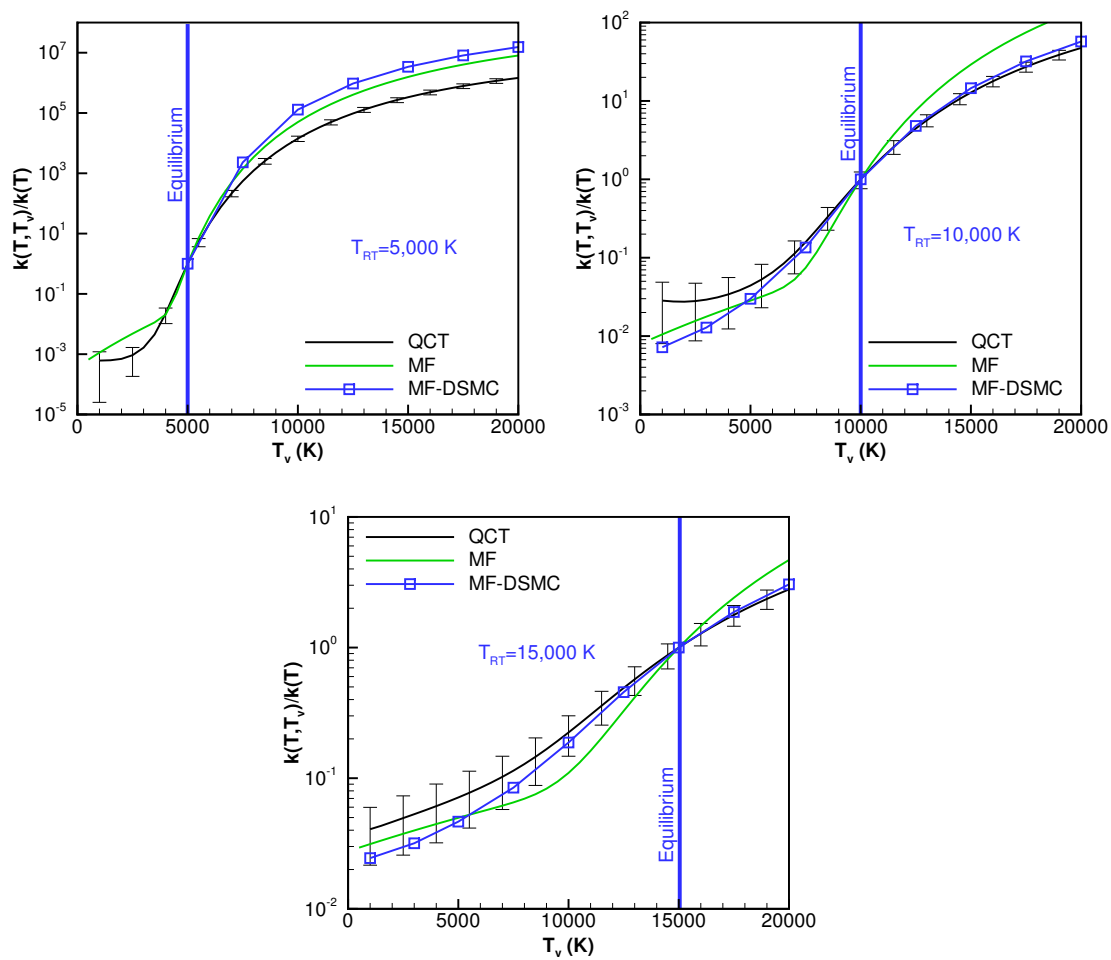


Figure 3.17. Nonequilibrium factor for $O_2 + O \rightarrow O + O + O$

Figure 3.18. Nonequilibrium factor for $N_2 + O \rightarrow N + N + O$

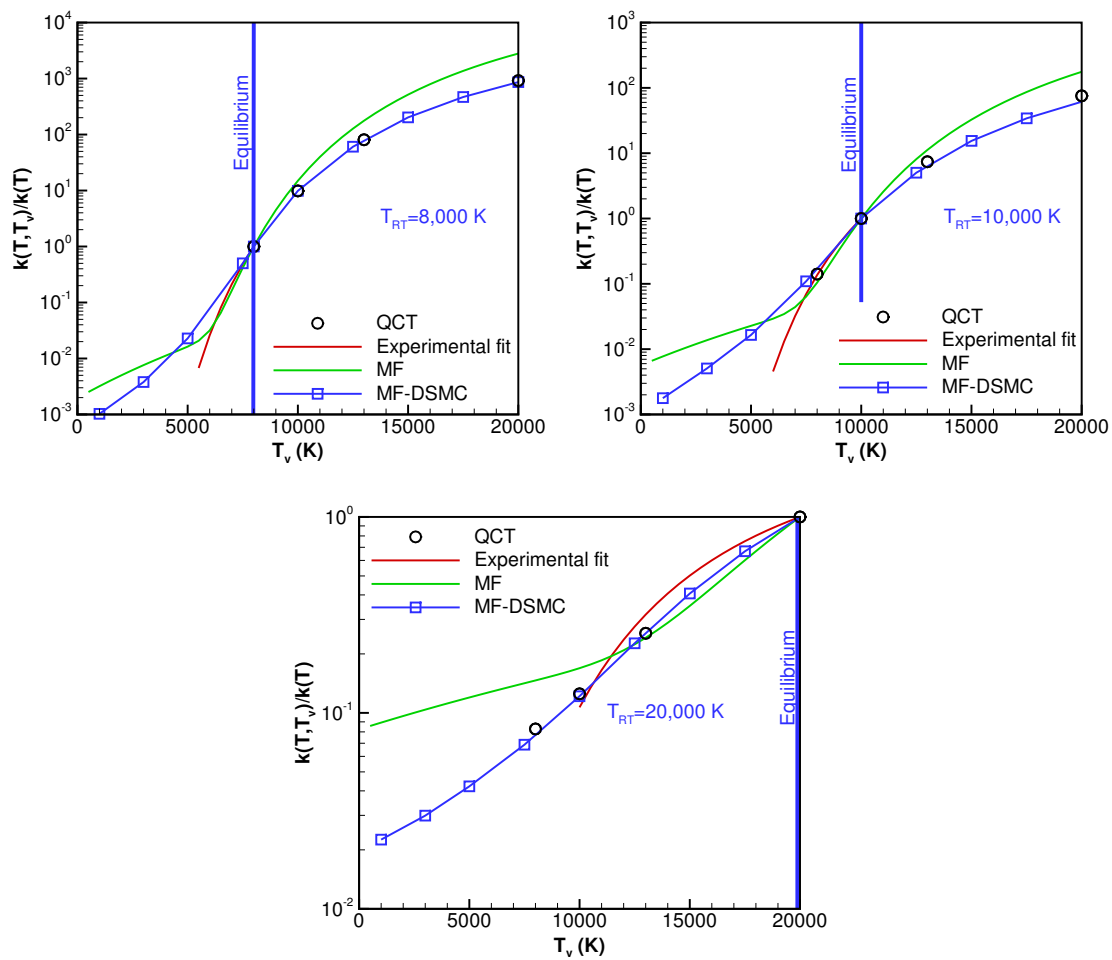


Figure 3.19. Nonequilibrium factor for $N_2 + N_2 \rightarrow N + N + N_2$

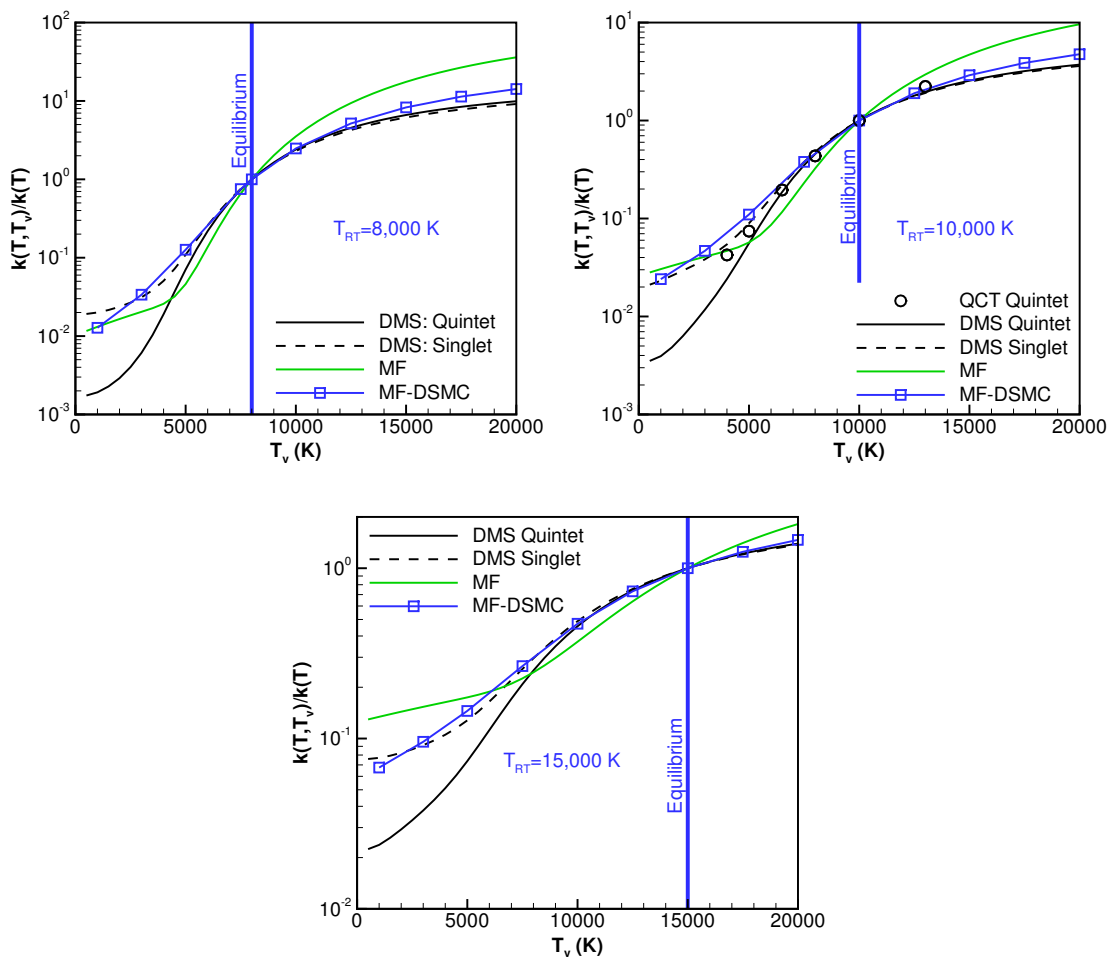


Figure 3.20. Nonequilibrium factor for $O_2 + O_2 \rightarrow O + O + O_2$

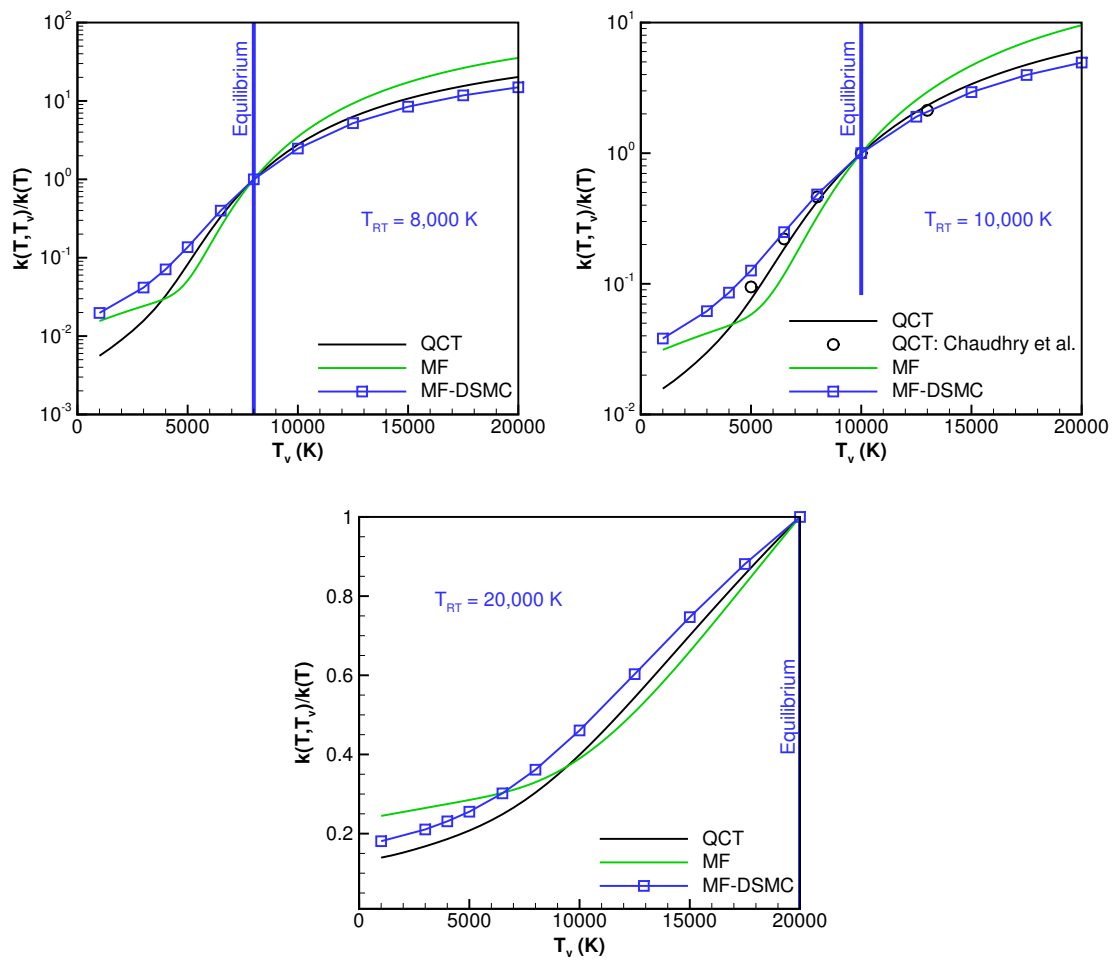


Figure 3.21. Nonequilibrium factor for $O_2 + N_2 \rightarrow O + O + N_2$

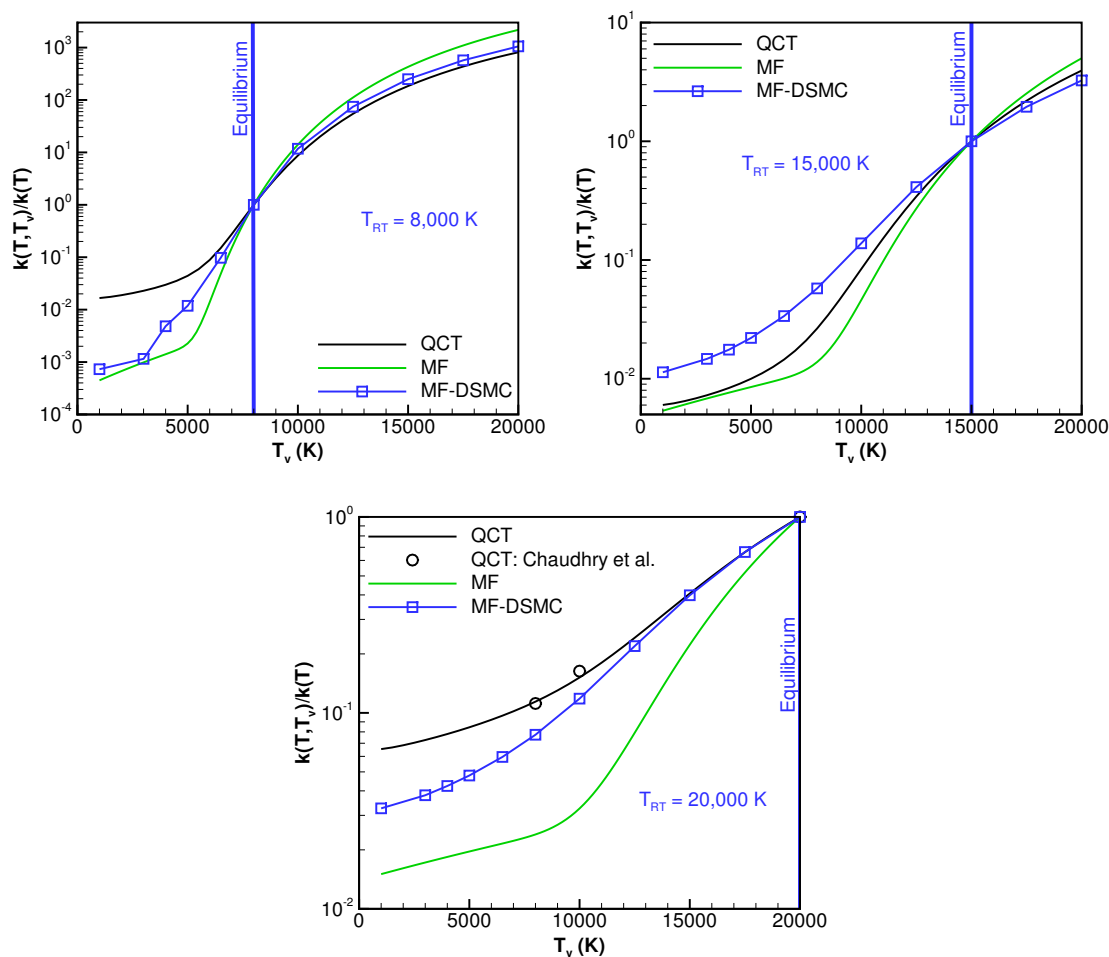


Figure 3.22. Nonequilibrium factor for $N_2 + O_2 \rightarrow N + N + O_2$

3.4.2.3 Vibrational Energy Consumption in Dissociation

In thermochemical nonequilibrium, the vibrational and rotational energy consumption in the dissociation represents an important part of the overall relaxation process, which, in turn, affects the reaction itself. In a state-specific chemical reaction model or particle-based simulation method, the vibrational and rotational energy consumption is naturally accounted for. However, for CFD with multi-temperature model, bulk chemical species with Boltzmann distributions of internal states are assumed, and the vibrational/rotational energy consumption must be explicitly mod-

eled. In this section, we compare the average vibrational energy removed by dissociation reactions (i.e. $E_{v,rem}$) in order to validate MF-DSMC model and to provide information for CFD modeling of thermally nonequilibrium chemical reactions. The baseline values of $E_{v,rem}$ are calculated from vibrational state-specific rates obtained by QCT method,

$$E_{v,rem}(T, T_v) = \frac{\sum_v E_v(v)k(T, v)x(T_v, v)}{\sum_v k(T, v)x(T_v, v)}, \quad (3.36)$$

where $E_v(v)$ is the vibrational energy of vibrational state v and $x(T_v, v)$ is the corresponding mole fraction for the given vibrational temperature T_v . For DSMC method, $E_{v,rem}$ are calculated implicitly as the following,

$$E_{v,rem}(T, T_v) = \frac{1}{N_{diss}} \sum_i^{N_{diss}} E_v(i), \quad (3.37)$$

where $E_v(i)$ is the vibrational energy of molecule i which dissociates and N_{diss} is the total number of molecules that dissociate.

The comparison is shown in Figs. 3.23 and 3.24. Red lines in the figures denote the average vibrational energy removed at thermally equilibrium conditions and other lines represent the values at nonequilibrium conditions. It is seen that MF-DSMC model reproduces $E_{v,rem}$ within 15% error for most dissociation reactions. The biggest difference is at low translational temperature since the probabilities of reactions are too low for DSMC method to resolve the accurate value of $E_{v,rem}$. For O₂ dissociated in collisions with N₂, there is some disagreement between the two sets of QCT data as T_v increases. MF-DSMC model underpredicts $E_{v,rem}$ by up to 0.2 eV at vibrationally cold conditions and agrees well with Chaudhry *et al.*'s results at vibrationally hot conditions. The model overpredicts $E_{v,rem}$ for O₂ dissociation in collisions with atomic oxygen. The reason for this is unclear. One of the plots in Fig. 3.23, namely the one for N₂+O, also shows the $E_{v,rem}$ calculated with the empirical Marrone-Treanor (MT) model [34]. Although not shown here, the non-preferential dissociation model that equates $E_{v,rem}$ to the average vibrational energy at vibrational temperature T_v would strongly disagree with both MF-DSMC and QCT. As seen in Figs. 3.23 and

3.24, $E_{v,rem}$ has strong dependence on translational temperature. As translational temperature increases, more molecules with low vibrational energy will have enough total energy to overcome the reaction barrier and dissociate. Hence, $E_{v,rem}$ should decrease with increasing translational temperature if the vibrational temperature is fixed. Preferential dissociation models such as MT model [34] can perform quite well as seen in Fig. 3.23 for N_2 dissociation in collisions with atomic oxygen.

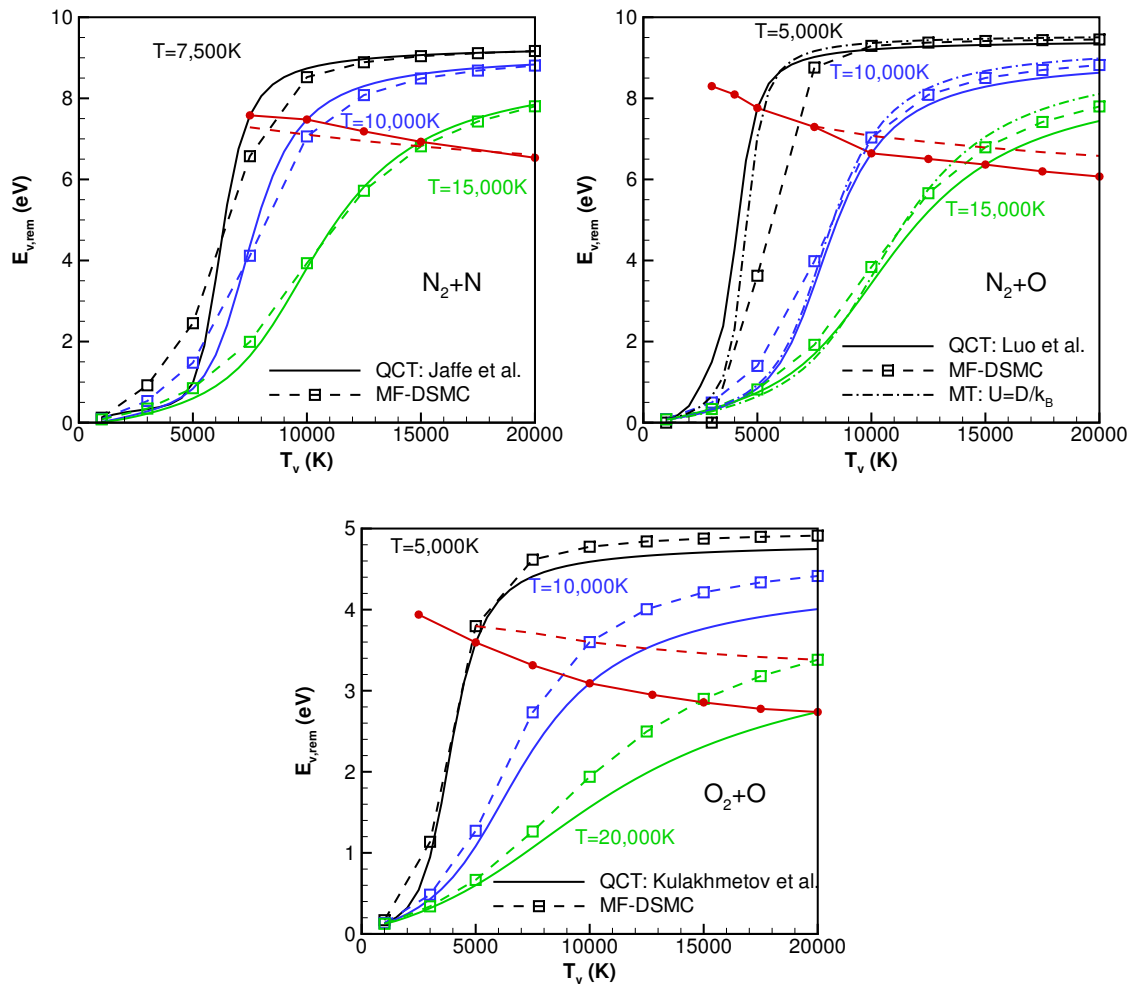


Figure 3.23. Comparison of the average vibrational energy removed by dissociation reactions for atom-diatom collisions. Red lines for thermally equilibrium conditions $T = T_v$; other lines for vibrationally nonequilibrium conditions $T \neq T_v$.

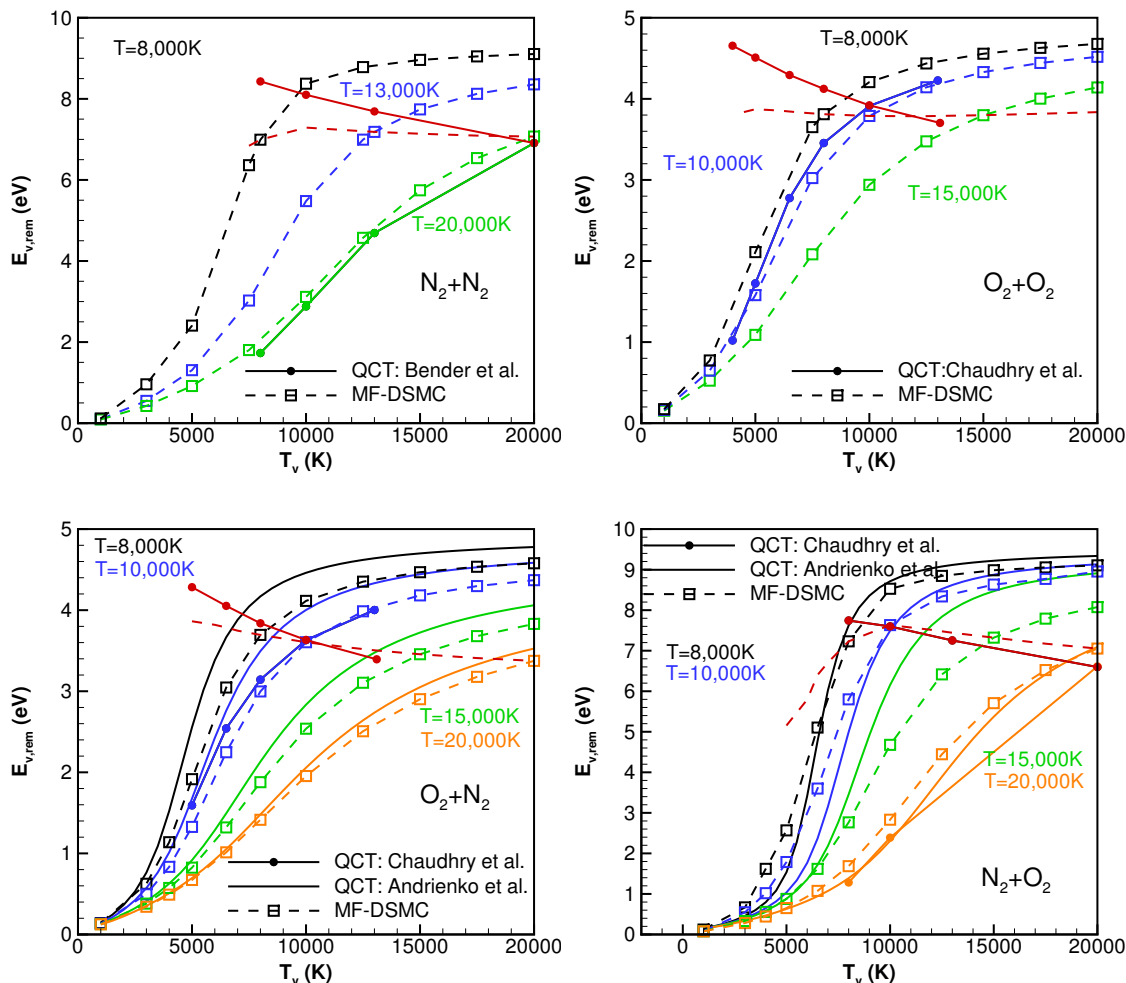


Figure 3.24. Comparison of the average vibrational energy removed by dissociation reactions for diatom-diatom collisions. Red lines for thermally equilibrium conditions $T = T_v$; other lines for vibrationally nonequilibrium conditions $T \neq T_v$.

3.4.2.4 Equilibrium Dissociation Rates

We now compare the calculated equilibrium dissociation rates with recent theoretical calculations [51–59, 62, 63, 108, 122], experimental measurements [21, 22, 100, 107, 113, 123, 124] and empirical estimations [18, 28, 33, 125, 126]. For convenience, the references for these data as well as for some empirical estimations are list in Table. 3.5. QCT data used here include Esposito *et al.*'s [52] and Jaffe *et al.*'s [51]

calculations of N_2+N , Andrienko *et al.*'s [55], Esposito *et al.*'s [53] and Kulakmetov *et al.*'s [54] calculations of O_2+O , Esposito *et al.*'s [57] and Luo *et al.*'s [56] calculations of N_2+O , Bender *et al.*'s [58] calculations of N_2+N_2 , Andrienko *et al.*'s [62] and Chaudhry *et al.*'s [121] calculations of O_2+N_2 and Andrienko *et al.*'s [63] calculations of $NO+N_2$. For ground state $O_2(X^3\Sigma_g^-)$, there are three spin states, namely singlet, triplet and quintet, for O_2-O_2 dimer. There are no complete QCT calculations for all these states. Besides, there are more than one electronic state possible to have dissociation reaction. Andrienko *et al.* [59] and Chaudhry *et al.* [122] calculated thermal equilibrium dissociation rates individually with QCT method using an empirical O_4 PES and an *ab-initio* PES. Without a factor that reflects the degeneracy of electronic state ($\eta = 16/3$), Andrienko *et al.*'s rates agree well with Byron [21] and Ibraguimova *et al.*'s measurements [100] for $T < 6,000$ K and Chaudhry *et al.*'s rates show better agreement for $T > 6,000$ K. Grover *et al.* [108] performed direct molecular simulation (DMS) with the *ab-initio* PES and obtained nonequilibrium dissociation rates with T_v lower than T by around 2,000 K.

Table 3.5.: References of equilibrium dissociation rates

Chemical reaction	QCT	Experiment	Estimation
$N_2+N \rightarrow 3N$	51, 52	123	33
$O_2+O \rightarrow 3O$	53–55	113	33
$N_2+O \rightarrow 2N+O$	56, 57	-	33
$N_2+N_2 \rightarrow 2N+N_2$	58	22, 123	33, 125
$O_2+O_2 \rightarrow 2O+O_2$	59–61	21, 100	33
$O_2+N_2 \rightarrow 2O+N_2$	60–62	21, 107, 124	18, 33
$N_2+O_2 \rightarrow 2N+O_2$	60–62	-	33
$NO+N_2 \rightarrow N+O+N_2$	63	-	18, 33, 126

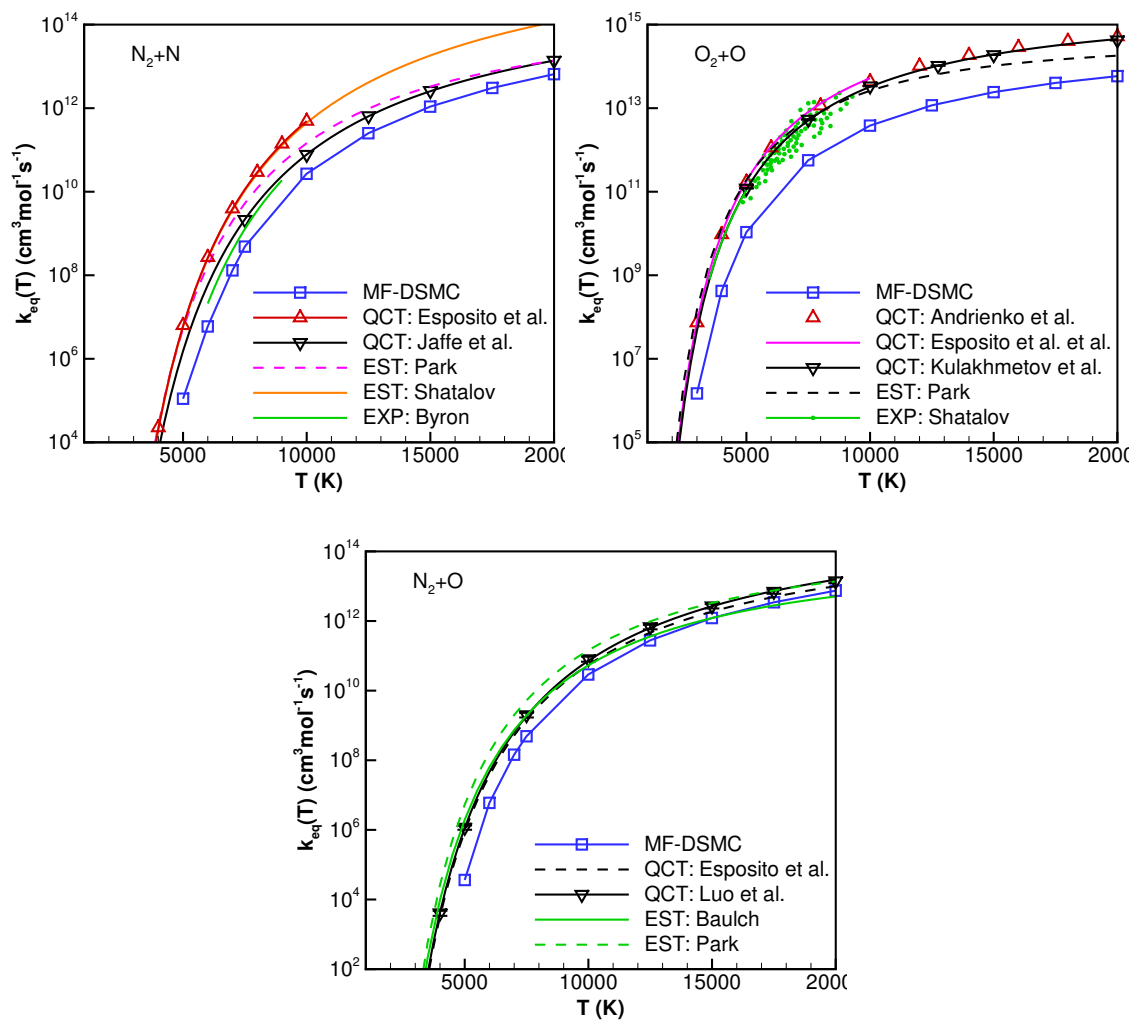


Figure 3.25. Comparison of diatom-diatom equilibrium dissociation rates

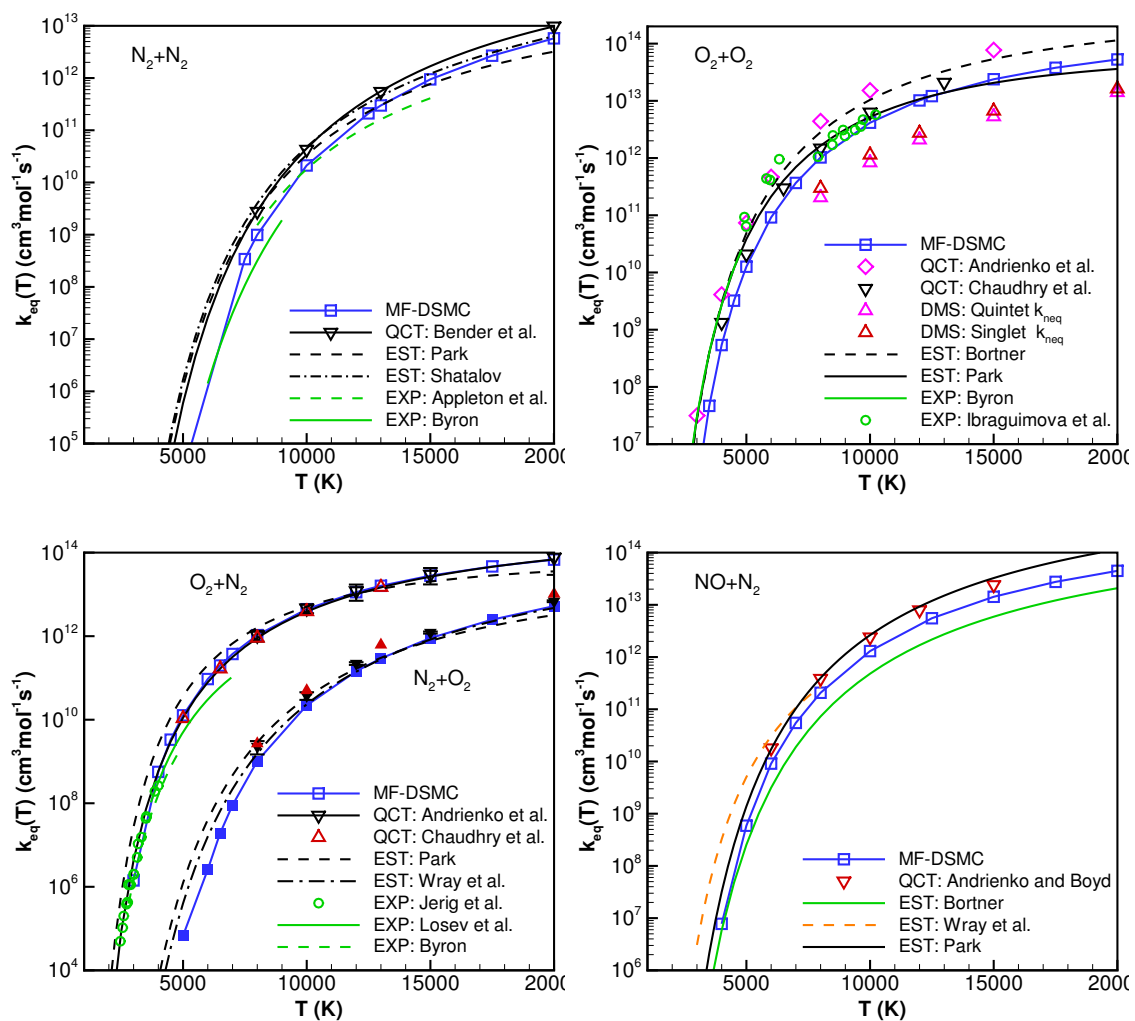


Figure 3.26. Comparison of diatom-atom equilibrium dissociation rates (QCT and DMS calculated rates for $\text{O}_2 + \text{O}_2$ are not multiplied by the electronic degeneracy factor $\eta = 16/3$)

The computed thermally-equilibrium dissociation rates are compared to the experimental data, rates recommended based on experimental data, as well as to the QCT sets discussed above in Figs. 3.25 and 3.26. It is seen that the rates calculated with MF-DSMC model are lower than the QCT data by an approximately constant factor. This is especially the case for N_2 dissociation. It is interesting to note that the equilibrium dissociation rates predicted by MF-DSMC model for N_2+N_2 show good agreements with QCT data. The agreement for N_2+O_2 is also good for $T \geq 10,000$ K but the rates are lower than Wray et al.'s estimation [18] by more than an order of magnitude for lower temperatures.

Since the nonequilibrium factors calculated with the MF-DSMC model were found in Sec. 3.4.2.2 to agree very well with QCT data, the disagreement between the calculated equilibrium rates and the QCT data is clearly due to the underestimation of total collision cross sections and rates by the VHS model commonly used in DSMC rather than to the MF dissociation model itself. Therefore, to improve the model, MF-DSMC should be paired with a better collision model. The details will be addressed in the next section.

3.4.3 Improved Modeling of Total Collision Cross Sections

As stated in Sec. 3.4.2.4, the difference between the thermally-equilibrium dissociation rates computed with MF-DSMC and QCT is a result of different collision models rather than of MF theory. Indeed, the MF theory described in Sec. 3.2 deals with energy transfer during chemical rearrangement assuming that the collision did happen. The reaction probability is the product of two probabilities: the probability of collision and the probability that dissociation occurs in the collision. It is the latter probability that is calculated in the MF theory, while the probability of collision has to be determined separately. The nonequilibrium factors, i.e. the nonequilibrium rates normalized by thermally-equilibrium rates, as well as the mean vibrational energy removed in dissociation, do not depend on the collision model, and here, as seen

in Sec. 3.4.2, MF-DSMC performs quite well. On the other hand, the absolute rates computed with MF-DSMC (Sec. 3.4.2.4) are lower than those calculated with QCT by a nearly-constant factor. Thus, in order to improve the model, the collision model has to be improved.

Since the VHS model was first proposed more than 30 years ago by Bird [36], it is still one of the most widely-used collision models for DSMC. The model is convenient due to its simple mathematical form and the model parameters can be calibrated to reproduce experimentally measured or calculated viscosities and thermal conductivities. However, the VHS model is problematic when temperature deviates substantially from the reference temperature [127]. The model assumes isotropic scattering law, which was subsequently improved in the variable soft sphere (VSS) model [79] with an additional parameter. The additional parameter changes the most probable scattering angle to a value less than 90 degrees and provides better agreement of multi-species diffusivity with experiments. However, recent QCT calculations for N_2-N_2 [82] have found that the model still overpredicts the scattering angle, especially at hyperthermal conditions. Similar findings for N_2-O was presented in Sec. 2.3.4. The larger scattering angle results in more efficient transport of mass, momentum and energy. Therefore, in order to reproduce correct transport coefficients, the model uses smaller total cross sections than the actual ones. This has been found in Ref. 81 for N_2+N collisions and will be shown below for N_2+O collisions. Additionally, the purely repulsive hard-sphere potential assumed by VHS model is inaccurate for both low [127] and high (>1 eV) [128] temperatures. For the former case, the long-range attractive force is dominant, and the Lennard-Jones potential works better. For the latter case, the colliding pair can reach shorter internuclear distances and an exponential repulsive potential is more physically realistic.

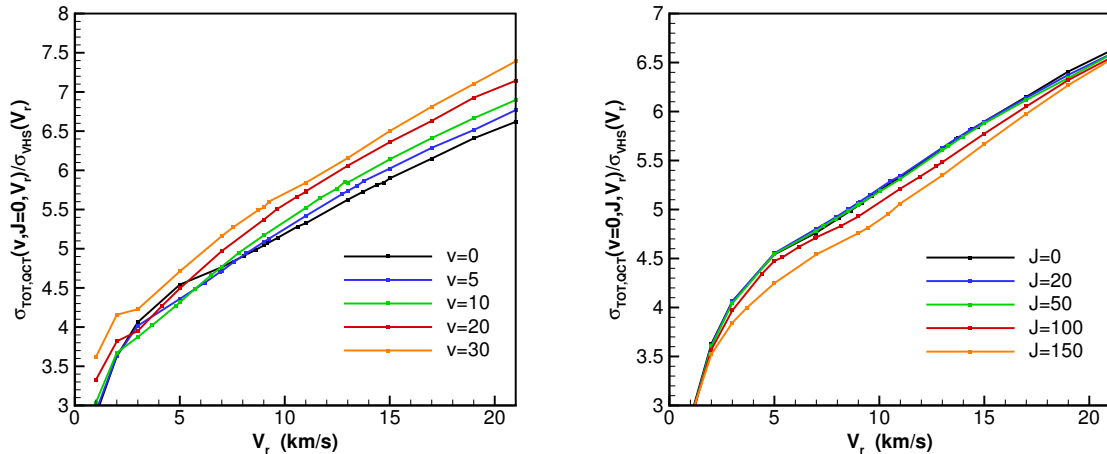


Figure 3.27. Comparison of QCT calculated total cross sections for different vibrational states and rotational states

3.4.3.1 QCT-Based Collision Model

To improve the modeling of collisions in DSMC, we made use of the available QCT data for $\text{N}_2\text{-O}$ collisions presented in Sec. 2.3.4 and calculated the total collision cross sections as the following,

$$\sigma_{T, QCT} = \sigma_{\text{elastic}}(\chi > 1^\circ) + \sigma_{\text{inelastic}} + \sigma_{\text{reaction}}, \quad (3.38)$$

where $\sigma_{\text{elastic}}(\chi > 1^\circ)$ are the elastic collision cross sections with the scattering angle χ larger than one degree, $\sigma_{\text{inelastic}}$ are the inelastic cross sections for collisions with at least one quantum change of vibrational or rotational energy and σ_{reaction} are the reaction cross sections. The total cross sections normalized by VHS cross sections are shown in Fig. 3.27. It is seen that VHS model significantly underpredicts the total cross sections. QCT total cross sections are at least a factor of 3 larger than VHS cross sections. The total cross section changes slightly with increasing rotational level. Importantly, it increases considerably with the vibrational level of N_2 molecule

because of the larger internuclear distance. We fit the vibrational state-specific total cross sections with the following analytical function:

$$\sigma_T = \sigma_0 \exp \left\{ aE_v + (b_1 + b_2E_v^2) \cdot \tanh [c (\log E_t - (d_1E_v^2 + d_2E_v + d_3))] \right\}$$

$$\sigma_0 = 69.0592 \text{ \AA}^2, a = 0.0510044, b_1 = -0.584551,$$

$$b_2 = -2.96928 \times 10^{-3}, c = 0.281619, d_1 = 0.0301812, d_2 = -0.436593, d_3 = 0.152225, \quad (3.39)$$

where E_v and E_t are the vibrational and translational energy in electron-volt and σ_T is the total cross sections in \AA^2 . The fitting is shown in Fig. 3.28. The maximum fitting error is less than 1 \AA^2 .

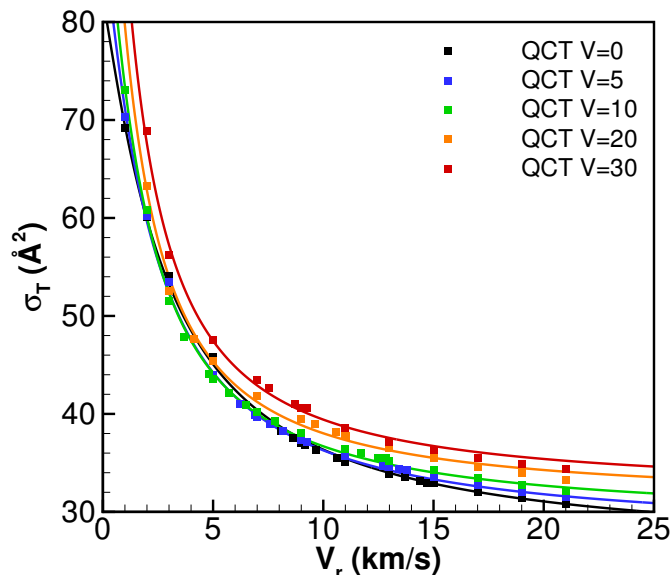


Figure 3.28. Comparison of fitted total cross sections and QCT data

Compared with VHS model, the larger total collision cross sections observed here, combined with the smaller scattering angles presented in Sec. 2.3.4, makes the QCT-based collisional model predict similar transport cross sections and transport properties. The new QCT-based collision model was implemented in DS1V code [36]. Equilibrium dissociation rates calculated from MF-DSMC model with VHS collision model (MF-DSMC-VHS) and QCT-based collision model (MF-DSMC-QCT) are compared

in Fig. 3.29. Better agreement with QCT calculated thermal equilibrium dissociation rate is obtained. For $T > 10,000$ K, the difference between MF-DSMC and QCT is negligible, which justifies the assumption of impulsive limit for high energy collisions and dissociation reactions. For other colliding partners, similar procedures of correcting total collision cross sections and scattering law can be used.

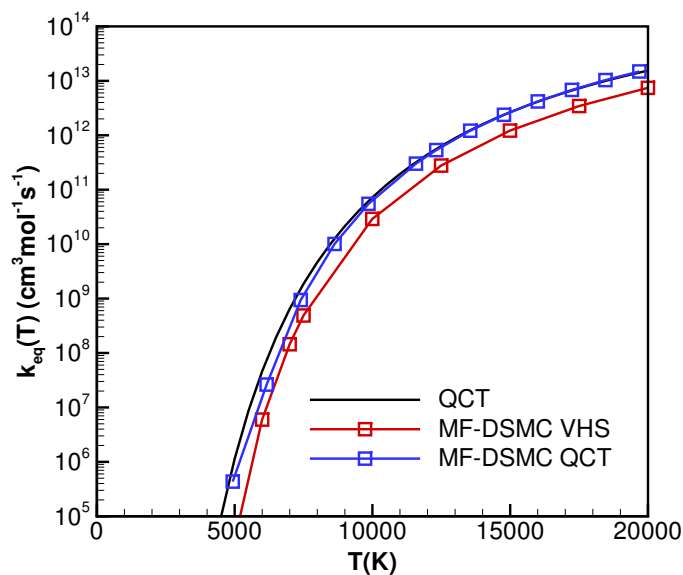


Figure 3.29. Comparison of equilibrium dissociation rates for N_2 dissociation in collisions with atomic oxygen predicted by MF-DSMC model with VHS or QCT-based collision model

It should be noted that, in order to define total cross sections, we introduce a cut-off of scattering angles. However, the definition of total cross section, or more fundamentally, “collision event”, is unimportant in DSMC algorithm. Physically, as the interaction always exists between molecular pairs, there doesn’t exist a finite interaction region. DSMC introduces total collision cross sections, similar to the cut-off of pairwise interaction in molecular dynamics, in order to reduce the computational cost. The increase of total collision cross sections will only influence the number of colliding pairs selected with the algorithm and increases computational time, but does

not affect any physical properties. It is the transport, reaction and internal energy exchange cross sections that should be modeled accurately in order to predict correct macroscopic properties. Regarding to the collision model, its main role is to provide the scattering law $\chi(b, E_t)$ and determine the transport cross sections defined as the following:

$$Q^{(l)}(E_t) = 2\pi \int_0^{+\infty} [1 - \cos^l \chi(b, E_t)] b db \quad l = 1, 2 \quad (3.40)$$

where χ is the scattering angle, b is the impact parameter, $Q^{(1)}$ is the momentum cross section related to diffusivity and $Q^{(2)}$ is the viscous cross section related to viscosity and thermal conductivity. Although the integral in Eq. 3.40 is improper, it is converged for most potentials with the notable exception of the long-range Coulomb potential. The convergence of transport cross sections at large impact parameters and therefore small scattering angles $\chi \ll 1$ is due to the factor $(1 - \cos \chi) \approx \frac{1}{2}\chi^2$ absent in the total cross section integral $\sigma_T = 2\pi \int_0^{b_{max}} db = \pi b_{max}^2$. Due to the negligible contribution of scattering with large impact parameter to the integral in Eq. 3.40, one can theoretically set b_{max} at any value that is large enough, as long as the corresponding minimum scattering angle χ_{min} is small and the scattering law is independent of b_{max} . In other words, one can select the cut-off scattering angle or impact parameter so as to change the total cross section without altering the transport cross section and thus transport properties. This flexibility of σ_T enables us to reproduce thermal equilibrium reaction rates with MF-DSMC model. Since, VHS and VSS models do not allow such flexibility (a change in total cross section would result in different scattering law), it is not possible to modify their parameters to improve the agreement of thermal equilibrium reaction rates when combined with MF-DSMC model.

3.4.3.2 Collision Model Based on Exponential Potential

In the previous section, we formulated a collision model based on *ab initio* potential. Although the model predicts equilibrium reaction rates that are in good

agreement with QCT data, the QCT calculated scattering angles are available to a very limited number of systems. On the other hand, the exponential repulsive potential has been widely used for the calculations of high-temperature transport coefficients [74, 129, 130] and VT relaxation rates [131] due to its simplicity. In the present section, a collision model based on exponential potential is presented in order to improve the prediction of thermal equilibrium dissociation rates by MF-DSMC model.

The potential investigated here has the following form:

$$V(r) = A \exp(-\alpha r), \quad (3.41)$$

where the suitable values of parameters A and α can be obtained from fitting to experimental data on scattering or transport properties [74, 90, 91] or to *ab initio* PEC [132]. The parameters used in the present work are summarized in Table 3.6.

Table 3.6.: Parameters of exponential potential

Colliding pair	A (eV)	α (\AA^{-1})	σ_{ref} (\AA^2)	$E_{t,ref}$ (eV)	η	Reference
N ₂ -N ₂	1.730E+03	4.000	110.90	3.46929E-05	0.0734	133
N ₂ -N	6.200E+02	3.310	147.63	3.70287E-05	0.0772	91
N ₂ -O ₂	4.816E+03	4.400	104.86	1.79835E-05	0.0682	134
N ₂ -O	1.135E+04	5.120	90.97	4.86912E-06	0.0626	91
NO-N ₂	5.780E+03	3.610	160.30	1.48752E-05	0.0672	91
O ₂ -O ₂	1.500E+02	3.000	129.65	2.88002E-04	0.0924	91
O ₂ -O	1.025E+04	4.850	99.52	5.69258E-06	0.0632	91

For a given impact parameter b and collisional energy E_t , the scattering angle χ is given by

$$\chi = \pi - 2/b \int_{r_0}^{+\infty} \frac{b^2/r^2 \cdot dr}{\sqrt{1 - (b^2/r^2) - V(r)/E_t}}, \quad (3.42)$$

where r_0 is the minimum distance between the colliding particles during the collision. It can be calculated from the following nonlinear algebraic equation by iteration:

$$1 - \frac{b^2}{r_0^2} - \frac{V(r_0)}{E_t} = 0. \quad (3.43)$$

The integration in Eq. 3.42 can only be performed numerically. To reduce the computational cost in DSMC, we first introduce the following nondimensional variables:

$$\begin{aligned} b^* &= \alpha b, & r^* &= \alpha r, & r_0^* &= \alpha r_0 \\ E_t^* &= E_t/A. \end{aligned} \quad (3.44)$$

Then the integral with respect to the intermolecular distance r is transformed into the integral with respect to $y = r_0^*/r^*$,

$$\chi = \pi - \frac{2b^*}{r_0^*} \int_0^1 f(y) \frac{dy}{\sqrt{1-y^2}}, \quad (3.45)$$

$$f(y) = \sqrt{\frac{1-y^2}{1 - b^{*2}/r_0^{*2} \cdot y^2 - \exp(-r_0^*/y)/E_t^*}}. \quad (3.46)$$

The function $f(y)$ is smooth and well behaved for y ranging from 0 to 1. The integral in Eq. 3.45 can be calculated with Gauss-Chebyshev quadrature. Convergence is obtained with less than 6 nodes. Since the integral parametrically depends on b^* and E_t^* , a lookup table can be built to use in DSMC to further reduce the computational cost. A comparison of the scattering angles for different collision velocity calculated with VHS model, exponential potential and QCT approach is shown in Fig. 3.30.

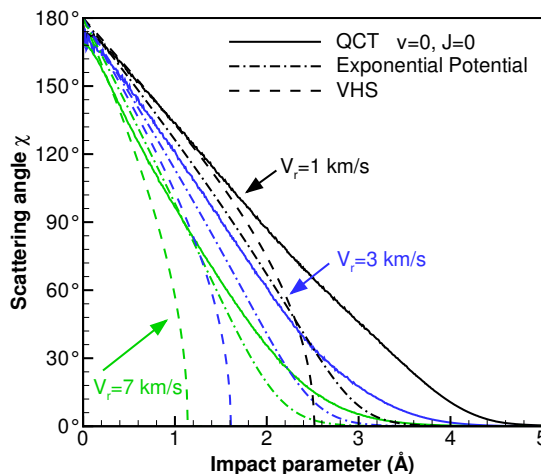


Figure 3.30. Comparison of scattering angles calculated with different approaches for N_2 -O collisions. QCT results of N_2 ground vibrational and rotational state are shown.

As discussed above and illustrated in Fig. 3.30, in contrast to the VHS model, for the exponential potential no finite impact parameter would result in 0 degree scattering. To model total cross sections and collision rates, we need to introduce a maximum impact parameter b_{max} . In the present work, we conservatively select b_{max} as the impact parameter which gives $\chi_{min} = 0.01$ rad deflection. The value can be further adjusted to reproduce the exact equilibrium dissociation rates as the reaction probability predicted by MF-DSMC model is independent of the collision model. The total cross sections can then be calculated as $\sigma_T = \pi b_{max}^2$. In our cases, the final values are fitted to the following form for all the colliding pairs investigated here:

$$\sigma_T = \sigma_{ref} \cdot \exp \left[1 - \left(\frac{E_t}{E_{t,ref}} \right)^\eta \right]. \quad (3.47)$$

The fitting parameters σ_{ref} , $E_{t,ref}$ and η are also listed in Table 3.6.

Since the collision frequency is changed, to reproduce the correct behavior of thermal relaxation, we also need to modify thermal relaxation numbers. Details can be found in Ref. 135. Moreover, it should be noted that the collision model also determines the distribution function of relative collisional energy for the selected col-

liding pairs, which further influences the probability density function (P.D.F.) used in Larsen-Borgnakke relaxation model to redistribute internal energy and translational energy after the collision. Although the influence is usually small, we present the form of the P.D.F. here for consistency. For the collision model based on exponential potential, the P.D.F. of collisional energy satisfies:

$$f_{E_t} \left(\frac{E_t}{kT} \right) \propto \frac{E_t}{kT} \exp \left[-\frac{E_t}{kT} - \left(\frac{E_t}{E_{t,ref}} \right)^\eta \right]. \quad (3.48)$$

For an internal mode with ζ degree of freedom (D.O.F.), the P.D.F. of its corresponding energy is given by

$$f_{E_i} \left(\frac{E_i}{kT} \right) = \frac{1}{\Gamma[\zeta/2]} \left(\frac{E_i}{kT} \right)^{\zeta/2-1} \exp \left(-\frac{E_i}{kT} \right), \quad (3.49)$$

where T_i is the temperature of the internal mode. Combining Eq. 3.48 and Eq. 3.49, we can obtain the appropriate P.D.F to sample post-collision internal energy for a given total energy E_c ,

$$f\left(\frac{E_i}{E_c}\right) \propto \left(\frac{E_i}{E_c}\right)^{\zeta/2-1} \left(\frac{E_c - E_i}{E_c}\right) \exp \left[-\left(\frac{E_c - E_i}{E_{t,ref}}\right)^\eta \right]. \quad (3.50)$$

The P.D.F. in Eq. 3.50 can be sampled with acceptance-rejection method. Details can be found in Ref. 36.

3.4.4 Improved Modeling of Vibrational Phase Angle

In the original algorithm of MF-DSMC model presented in Sec.3.4.2, the distribution function of vibrational phase angle was taken as a uniform distribution between 0 and 2π . This is based on the assumption that molecule vibrates as a harmonic oscillator (HO). It has been shown in Sec. 3.4.2.1 that when calculating vibrational state-specific rates for high vibrational levels, a significant error is introduced due to the HO assumption. The use of HO assumption for vibrational phase angle is also inconsistent with the anharmonic oscillator (AHO) model for vibrational energy ladder.

To model anharmonic vibration, we first need to solve the equation for molecular vibration,

$$\frac{1}{2}\mu \left(\frac{dr}{dt} \right)^2 + \frac{J(J+1)\hbar^2}{2\mu r^2} + V(r) = E_{rv}(v, J), \quad (3.51)$$

where r is the interatomic distance, μ is the reduced mass of the dissociated molecule, v and J are the vibrational and rotational levels, $V(r)$ is the two-body potential energy curve (PEC) and $E_{rv}(v, J)$ is the rovibrational energy. Once the variation of interatomic distance during a period of vibration τ is calculated, the vibrational velocity and vibrational phase angle φ can be calculated as the follows,

$$v(r) = \frac{dr(t)}{dt}, \quad v_{max} = v(r = r_{eq}) \quad (3.52)$$

$$\varphi(t/\tau) = \arccos \left[\frac{v}{v_{max}} \right] \quad (3.53)$$

Eq. 3.53 should then be used to sample phase angle for anharmonic vibration.

In the present work, we neglect the coupling between rotational and vibrational motion and further set for $J = 0$. There are multiple options for the two-body PEC $V(r)$, Rydberg–Klein–Rees (RKR), PEC derived from molecular constants, *ab initio* PEC calculated from electronic structure or empirical Morse potential. Due to the complexity of their mathematical forms, RKR and *ab initio* PEC would both require a pre-calculated table of vibrational phase angles as a function of time for different vibrational levels in order to implement them in DSMC. In contrast, Morse potential lends itself to a simple analytical solution [136]. We take the following form of Morse potential,

$$V(r) = D_e (1 - e^{-\beta(r-r_e)})^2 - D_e, \quad (3.54)$$

where r_e is the equilibrium distance for the interatomic vibration. Introducing the following notations,

$$\rho^2 = E_v/D_e, \quad \theta_0 = \arcsin(\rho), \quad (3.55)$$

$$\omega_0 = \beta \sqrt{\frac{2D_e}{\mu}}, \quad \omega_v = \sqrt{1 - \rho^2} \omega_0, \quad (3.56)$$

$$v_{max} = \frac{\rho \omega_0}{\beta} = \sqrt{\frac{2E_v}{\mu}}, \quad (3.57)$$

we can get the solutions of interatomic distance r as well as the vibrational velocity with the initial condition $v(t = 0) = v_{max}$,

$$r = r_e + \frac{1}{\beta} \ln \left[\frac{1 + \rho \sin(\omega_v t - \theta_0)}{1 - \rho^2} \right], \quad (3.58)$$

$$v = \frac{\rho \omega_v}{\beta} \frac{\cos(\omega_v t - \theta_0)}{1 + \rho \sin(\omega_v t - \theta_0)}. \quad (3.59)$$

The phase angle and the period of vibration can be calculated according to Eqs. 3.52 and 3.53,

$$\varphi = \arccos \left[\frac{v}{v_{max}} \right] = \begin{cases} \arccos \left[\frac{\cos \theta_0 \cos(\omega_v t - \theta_0)}{1 + \sin \theta_0 \sin(\omega_v t - \theta_0)} \right] & \frac{t}{\tau} \in [0, \frac{\theta_0}{\pi} + \frac{1}{2}] \\ 2\pi - \arccos \left[\frac{\cos \theta_0 \cos(\omega_v t - \theta_0)}{1 + \sin \theta_0 \sin(\omega_v t - \theta_0)} \right] & \frac{t}{\tau} \in (\frac{\theta_0}{\pi} + \frac{1}{2}, 1] \end{cases}, \quad (3.60)$$

$$\tau = 2\pi/\omega_v. \quad (3.61)$$

It can be found from Eqs. 3.51-3.60 that the only parameters needed for this are the coefficients of Morse potential, (D_e , r_e and β) and the rovibrational ladder $E_{rv}(v, J)$. They can be obtained by using RKR classical turning points [137] or fitting *ab initio* PEC. The coefficients used in the present work are listed in Table. 3.7.

Table 3.7.: Parameters of Morse potential

	N ₂	O ₂	NO
D_e (eV)	9.905	5.211	6.623
r_e (Å)	1.0977	1.207	1.159
β (Å ⁻¹)	2.81971	2.78	2.83

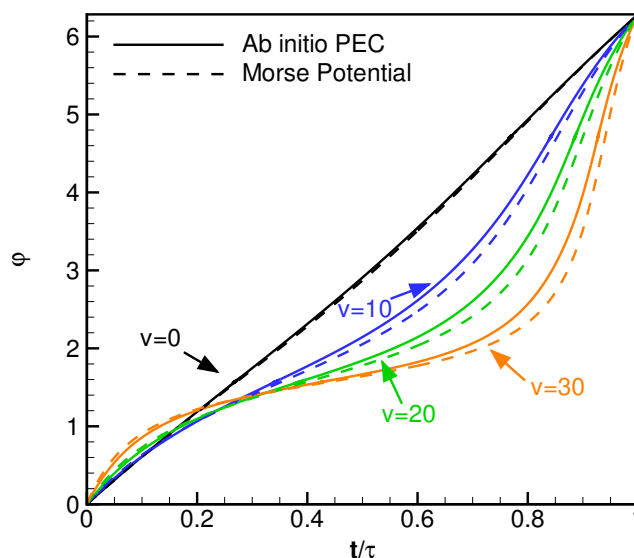


Figure 3.31. Time variation of vibrational phase angle during the period of vibration for O_2 molecule

To validate the accuracy of Morse potential, vibrational phase angles of molecular oxygen for different vibrational levels calculated with Eq. 3.60 are compared with the solution of *ab initio* PEC in Fig. 3.31. In general, the agreement is satisfactory. It can be seen that as vibrational level increases, the molecule stays longer near $\varphi = \pi/2$, which corresponds to the outer turning point of the oscillator. Because the outer turning point corresponds to the optimal geometry for dissociation to occur [101,103], the AHO model should predict a higher probability of dissociation compared with SHO model. To incorporate AHO model into MF-DSMC model, we only need to replace the one-step procedure of sampling φ from $\mathcal{U}(0, 2\pi)$ in the algorithm by first sampling t/τ from $\mathcal{U}(0, 1)$ and then calculating φ based on Eq. 3.60.

3.4.5 Validation of the Improved Model

To illustrate the improvements of MF-DSMC model, both the AHO model presented in Sec.3.4.4 and the collision model based on exponential potential presented

in Sec. 3.4.3.2 were implemented in DSMC. In the following context, the original version of MF-DSMC model will be denoted as “MF-DSMC”. The one with vibrational phase angle sampled from AHO model will be denoted as “MF-DSMC-AHO” and the one with combined with the collision model based on exponential potential will be denoted as “MF-DSMC-EXP”.

3.4.5.1 Vibrational State-Specific Rates

To check the performance of the AHO model, the vibrational state-specific dissociation rates calculated with different models for various colliding pairs are compared in Fig. 3.32. Although these rates are not directly used in DSMC method, the comparison helps to verify the model at thermal nonequilibrium conditions and provides information for state-specific modeling in CFD. The method of calculating vibrational state-specific dissociation rates in DSMC has been introduced in Sec. 3.4.2.1. To clearly show the difference between MF-DSMC and MF-DSMC-AHO model, the rates for N_2+N and N_2+O are scaled in the following manner,

$$k^{Scale}(T, E_v) = k(T, E_v) \cdot \frac{k_{eq, QCT}(T)}{k_{eq}(T)}, \quad (3.62)$$

where $k(T, E_v)$ and $k_{eq}(T)$ are the state-specific rates and equilibrium rates predicted by the models.

In this context, it can be found that the incorporation of AHO model in MF-DSMC model helps to capture the nonlinear dependence of $\log(k(T, E_v))$ on E_v for high vibrational levels. The MF-DSMC model with harmonic oscillator assumption tends to underpredict the rates by up to an order of magnitude at high vibrational levels. This could make the model underpredict $E_{v,rem}$ and reaction rates for vibrationally hot conditions. However, as the change of rates brought by the AHO model for low vibrational levels is insignificant and the concentration of molecules with high vibrational energy is low, the nonequilibrium rates at vibrationally cold conditions should not be affected.

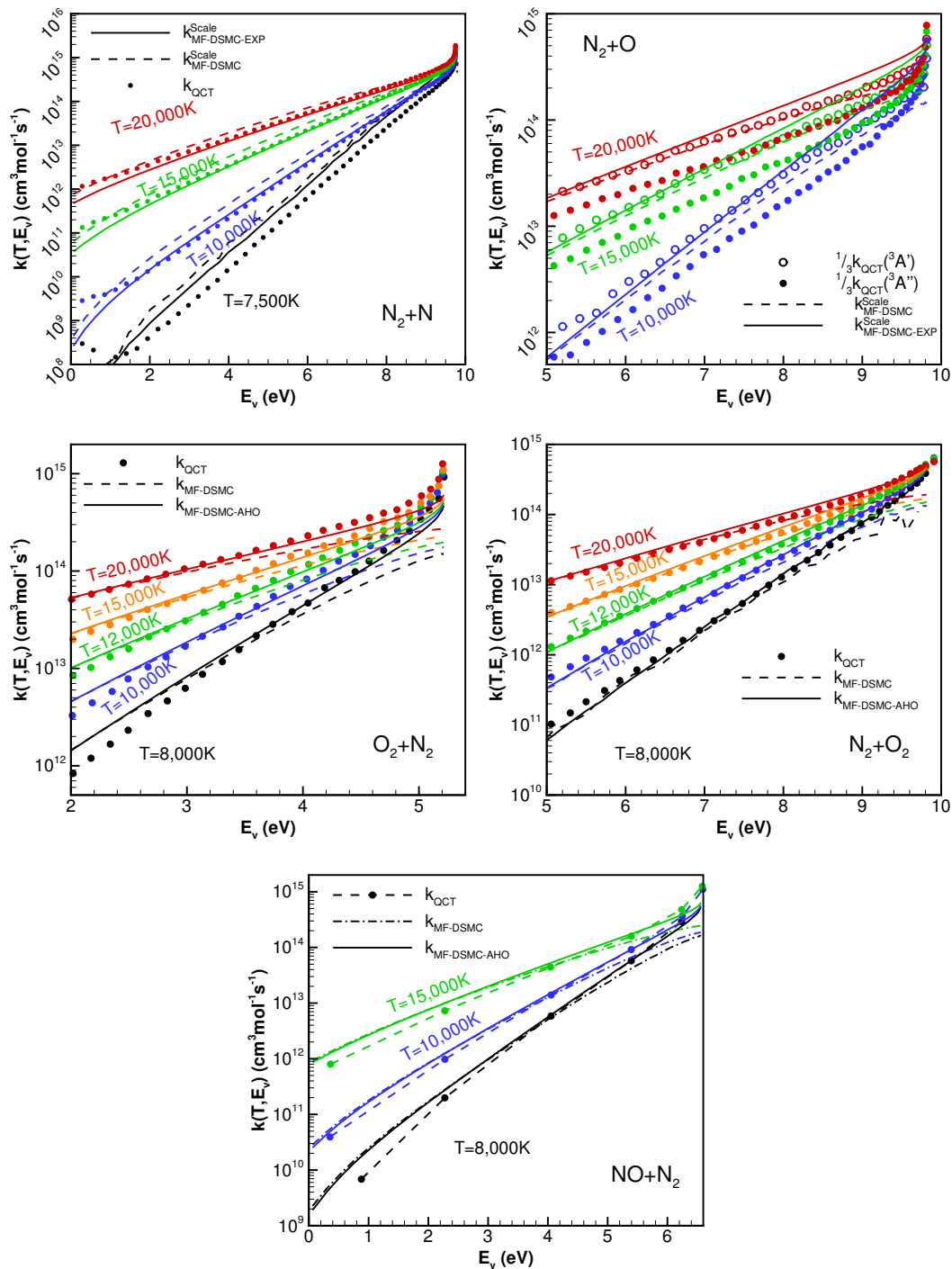


Figure 3.32. Comparison of vibrational state-specific rates calculated by QCT method and MF-DSMC model for $\text{N}_2 + \text{N}$, $\text{N}_2 + \text{O}$, $\text{O}_2 + \text{N}_2$, $\text{N}_2 + \text{O}_2$, and $\text{NO} + \text{N}_2$ dissociations. MF-DSMC rates for $\text{N}_2 + \text{N}$ and $\text{N}_2 + \text{O}$ are scaled.

3.4.5.2 Equilibrium Dissociation Rates

Unlike the phenomenological TCE model based on the inverse Laplace transform of Arrhenius reaction rates, MF-DSMC model has no adjustable parameters and it only predicts the probability of dissociation once a collision occurs. To calculate equilibrium reaction rates, collision rates need to be modeled separately. In Sec. 3.4.3, it has been concluded that the exact total collision rates and cross sections in DSMC algorithm don't matter as long as the scattering law and transport cross sections are correct. Such flexibility allows us to use collision models like the one based on exponential potential introduced in Sec. 3.4.3.2 to make MF-DSMC model reproduce experimentally or theoretically calculated thermal equilibrium rates. In this section, the equilibrium dissociation rates predicted by MF-DSMC-AHO and MF-DSMC-EXP models are compared with recent QCT calculations and experimental measurements.

The equilibrium dissociation rates are shown in Figs. 3.33 and 3.34. It is seen that for N_2+N and N_2+O , the MF-DSMC-EXP model clearly in a better agreement with QCT data for the entire range of temperatures. For N_2+O , MF-DSMC-AHO agrees better with Esposito et al.'s calculations [57] while MF-DSMC-EXP agrees better with Luo et al.'s data [56]. There is no discernible difference between the QCT data and those predicted by the models for $T > 10,000$ K. For N_2+N_2 , O_2+O_2 and $NO+N_2$, the MF-DSMC-EXP model slightly overpredicts the collision rates at high temperatures and results in slightly higher equilibrium dissociation rates. MF-DSMC-AHO shows better agreements for these colliding pairs, although the difference is very small, within a factor of 2. It should be noted that, since AHO model has little effect for molecules with low vibrational energy and such low energy levels are more populated at low temperatures, it is expected that MF-DSMC and MF-DSMC-AHO models should give similar predictions as temperature decreases or in vibrationally cold conditions. For O_2+N_2 , the original version of MF-DSMC model gives the best predictions for both reaction channels.

The comparison for O_2+O shows some interesting findings. The chemical reaction by itself is complex due to the multiple PESs for O_2-O system and the small gap between different electronic states of O_2 . For ground state molecular oxygen $O_2(^3\Sigma_g^-)$ and atomic oxygen $O(^3P)$, their combination results in 27-fold degeneracy, contributed from 3 singlet, 3 triplet and 3 quintet states. Esposito et al. [53] and Kulakhmetov et al. [54] conducted QCT calculations for one singlet PES and assumed reaction rates from other PESs are 0. On the other hand, Chaudhry [61] conducted QCT calculations for all 9 PESs and obtained the average reaction rates weighted by the degeneracy (labeled as “QCT: Chaudhry” in Fig. 3.33). To take the existence of multiple electronic states of O_2 even at low temperatures, the rates need to be multiplied by the multi-surface correction factor $\eta = 16/3$, which is the ratio of the degeneracy of all bonded O_2 electronic states to the one of ground state. Chaudhry’s result is labeled as “QCT: Chaudhry (with $\eta = 16/3$)” in Fig. 3.33. By comparing Chaudhry’s QCT data to experiment, we can clearly see the importance of the multi-surface correction factor. Since MF-DSMC model only considers the dissociation from ground state molecule (electronically excited states have smaller dissociation energy and different energy spectrum), it is more fair to compare the rates with QCT data that are not multiplied by the multi-surface correction factor. It can be found MF-DSMC-AHO shows a descent agreement with Chaudhry’s uncorrected QCT result, which further confirms the validity of classical impulsive assumption for high temperature dissociation reaction. However, it also shows the shortcoming of MF-DSMC model for species that have close lying electronic states. This can be overcome by modifications of collisional model.

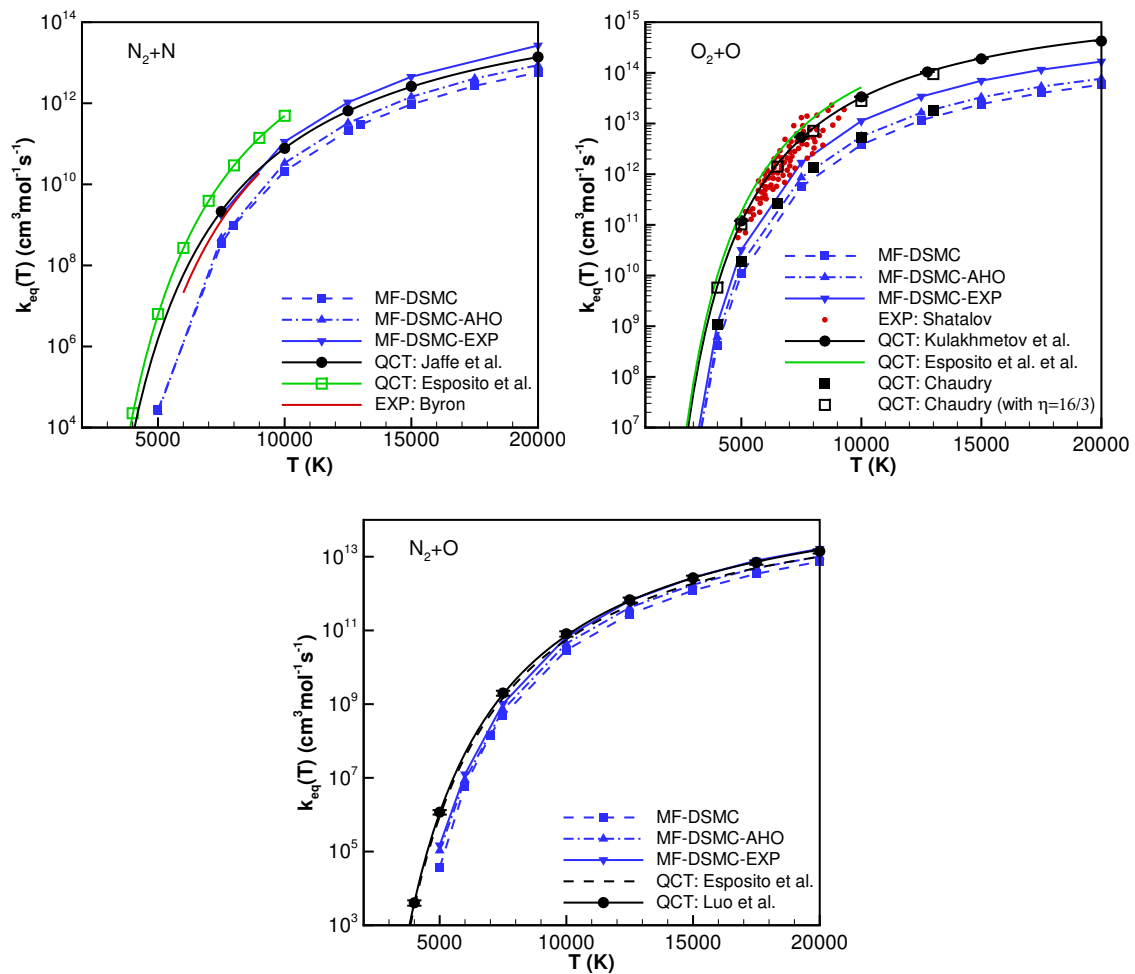


Figure 3.33. Comparison of diatom-atom equilibrium dissociation rates for N_2+N , O_2+O , and N_2+O colliding pairs.

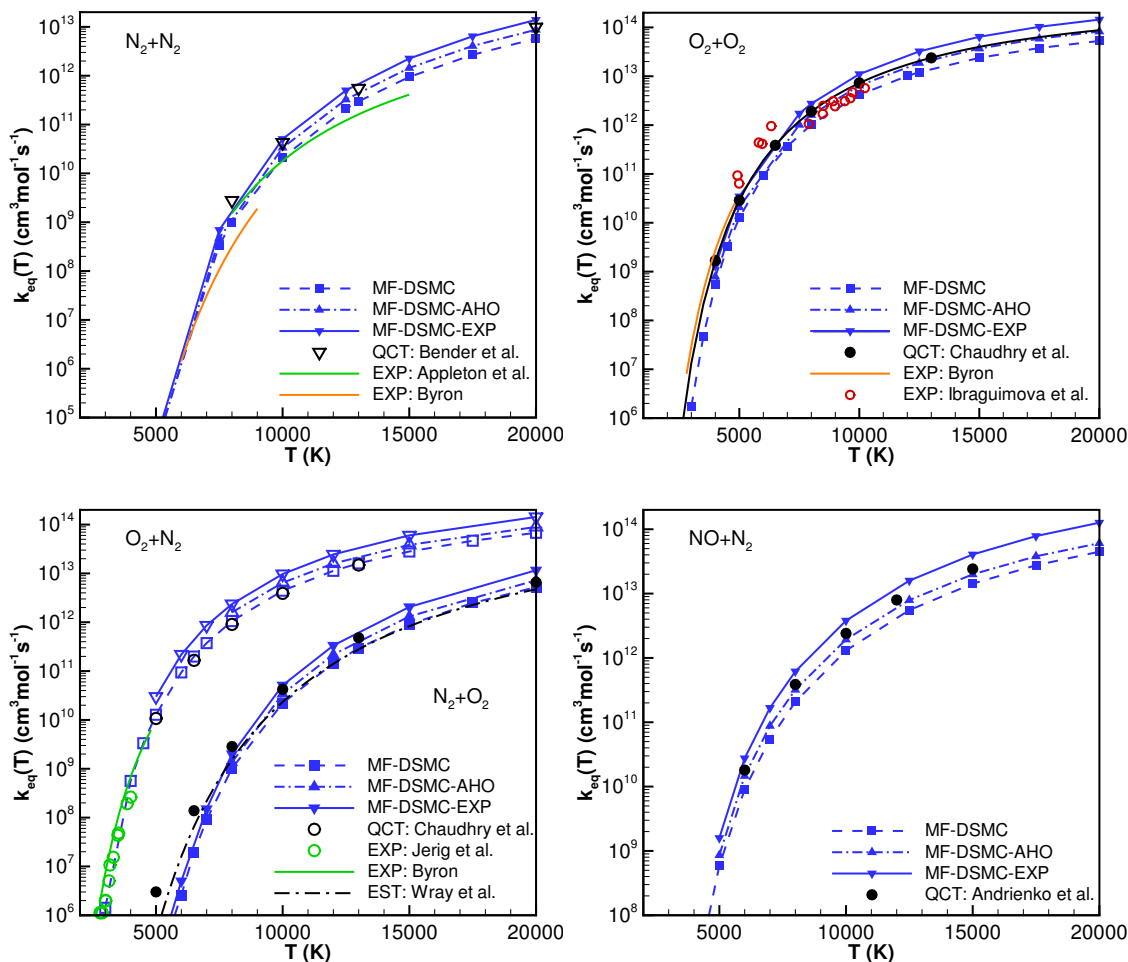


Figure 3.34. Comparison of diatom-diatom equilibrium dissociation rates for N_2+N_2 , O_2+O_2 , O_2+N_2 and N_2+O_2 , and $\text{NO}+\text{N}_2$ colliding pairs. The first molecular symbol indicates the dissociating molecule.

3.4.6 Simulation of O_2 Reacting Shock

In this section, the MF-DSMC and MF-DSMC-AHO model are evaluated by simulating O_2 reacting shock experiments by Ibragimova *et al.* [100]. The case has been extensively used to validate nonequilibrium chemical reaction models. Studies using QCT based state-specific rates [138] or cross sections [139] in general show good agreement for flow properties. Additionally, adjusting empirical vibrational-

favoring models such as Marrone-Treanor model [140] and Kuznestsov state-specific model [100,120] to match QCT data, produces better agreement with the shock tube experiments than the original Marrone-Treanor and Kuznestsov models.

Table 3.8.: Freestream conditions of O₂ reacting shock

Mach number	Pressure (Torr)	Shock speed (km/s)	Temperature (K)
9.3	2.0	3.07	295
13.4	0.8	4.44	295

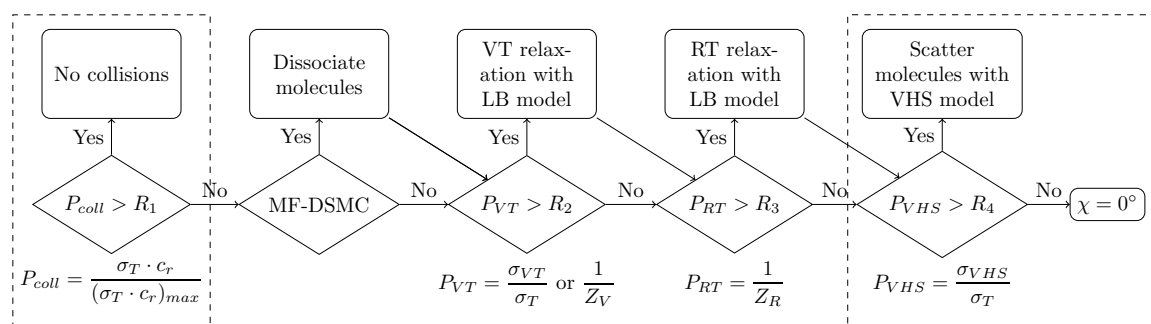


Figure 3.35. Collision procedure of the DSMC code

In the present work, two different free stream conditions are considered and they are listed in Table 3.8. The DSMC code used to calculate reaction rates is employed here to simulate the 1D flow. There are two reactions need to be modeled, namely O₂ dissociated by O₂ and O₂ dissociated by O. As it has been shown in Sec. 3.4.5.2, MF-DSMC-AHO model combined with VHS model can reproduce Byron's experimentally measured equilibration dissociation rate for O₂+O₂ [21] (it is the rate coefficient recommended by Park [33]). However, the equilibration dissociation rate for O₂+O is always underpredicted. In order to reproduce the correct equilibrium rate, the collision procedure of DSMC was modified and is summarized in Fig. 3.35. Main changes include the implementation of carefully tuned total collision cross sections and the change of scattering procedure, which are enclosed by dashed lines in the figure. σ_T for

O_2+O collision is calibrated to make MF-DSMC-AHO model reproduce Kulakhmetov *et al.*'s QCT calculated rates. As it is shown in Fig. 3.36, the calibrated total cross sections allow MF-DSMC-AHO to reproduce the rates. The implementation of the additional check for scattering is aimed at reproducing transport properties.

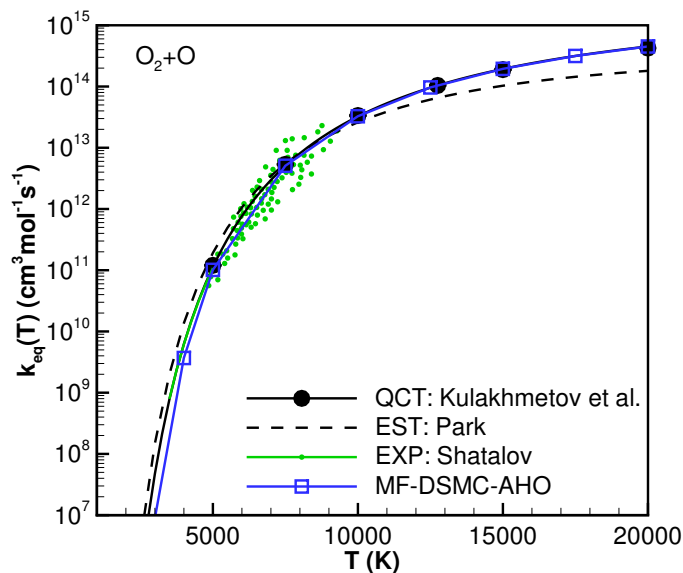


Figure 3.36. Comparison of equilibrium dissociation rate for O_2-O predicted by MF-DSMC-AHO model combined with calibrated total cross sections with experimental data and QCT calculations

Except for chemical reactions, VT relaxation and RT relaxation also play important roles here as the flow is highly thermochemical nonequilibrium. A standard Larsen-Borgnakke model is employed to describe VT relaxation for O_2-O_2 and RT relaxation for both O_2-O_2 and O_2-O . The model uses vibrational relaxation number Z_V and rotational relaxation number Z_R to determine whether a relaxation occurs or not. The relaxation number is defined as the number of collisions required before for a relaxation event. These numbers are calculated as the ratio of relaxation time $\tau_{VT/RT}$ and mean collision time τ_{coll} . They are also corrected with Haas *et al.*'s method for Z_R [141] and Gimelshein *et al.*'s method for Z_V [135] in order to fix the inconsistency

between the definitions of relaxation collision numbers in CFD and DSMC. For VT relaxation of O₂-O₂, τ_{VT} measured by Ibraguimova *et al.* [100] was used. The values of τ_{VT} have been presented in Sec. 3.3.3. The rotational relaxation numbers come from Parker's polynomial fit [142]. For O₂-O VT relaxation, Kulakhmetov *et al.*'s ME-QCT-VT state-specific model [54] was used. The model calculates the VT relaxation cross section σ_{VT} for a transition from initial vibrational level v to final vibrational level v' with a total collision energy E_c as,

$$\sigma_{VT}(E_c, v \rightarrow v') = \sigma_{ref} E_t^{\nu-1} \frac{\left(1 - \frac{E_v(v')}{E_c}\right)^\nu}{\sum_{v'} \left(1 - \frac{E_v(v')}{E_c}\right)^\nu} \exp\left(S_v(E_c, v, v')\right), \quad (3.63)$$

$$\begin{aligned} S_v(E_c, v, v') &= A|E_v(v) - E_v(v')| + B \exp\left(-\left|\frac{E_v(v) - E_v(v')}{C}\right|^D\right) \\ &+ E \exp\left(-F\left(\frac{E_v(v')}{E_d} - 1\right)\left(\frac{E_v(v)}{E_d} - 1\right)\right), \end{aligned} \quad (3.64)$$

where E_d is the dissociation energy, E_v is the vibrational energy and σ_{ref} , A , B , C , D and E are model parameters. Details of the model can be found in Ref. 54. Since the VT cross sections σ_{VT} are directly calculated with the model, there is no need for a relaxation time or relaxation number. The probability of VT relaxation is simply the ratio of σ_{VT} to the total cross sections.

To simulate 1D shock wave, the stagnation streamline flow approach [36] is used. The hypersonic free stream is set at the upstream boundary and a wall is placed at the downstream boundary. The one-dimensional shock wave is obtained through the removal of particles in the downstream region based on the mass flow rate from the upstream. The method is actually a one-dimensional approximation of the actual stagnation streamline in a two-dimensional flow over a blunt body.

The comparison of flow properties including temperatures, density and mass fraction of O₂ are shown in Figs. 3.37-3.39. Figure 3.40 presents the vibrational energy populations of O₂ molecules at different locations across the shock wave predicted by MF-DSMC and MF-DSMC-AHO models. In addition to Ibraguimova *et al.*'s experimental measurements [100], the results of two state-specific simulations are also shown in the same figures. Andrienko *et al.* [138] conducted simulations with master

equations. QCT calculated VT relaxation rates and state-specific dissociation rates for O_2+O were used. O_2+O_2 VT relaxation were modeled with forced harmonic oscillator model [131]. The state-specific dissociation rates for O_2+O_2 were obtained by scaling the ones for O_2+O with Marrone-Treanor model [34]. Sebastião *et al.*'s framework of DSMC simulation (Model 4 in Ref. 139) is very similar to the one in this work except that they used QCT state-specific O_2+O dissociation model [54] and calibrated TCE model for the chemical reactions. These two calculations are believed to be the most state-of-art state-specific simulations and are compared to evaluate the MF-DSMC model.

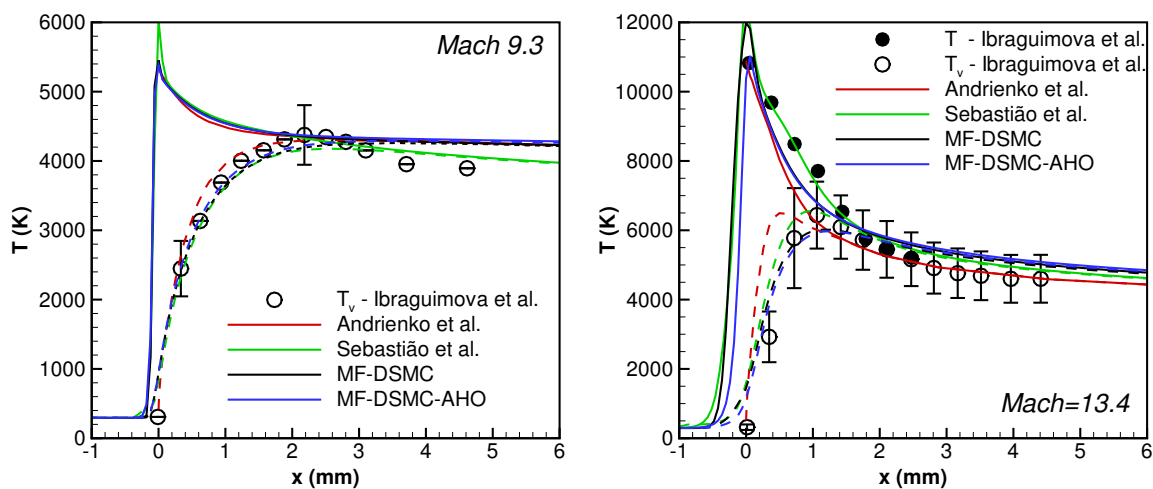


Figure 3.37. Comparison of the temperature profile for the two cases; Solid lines for translational temperature; dashed lines for vibrational temperature

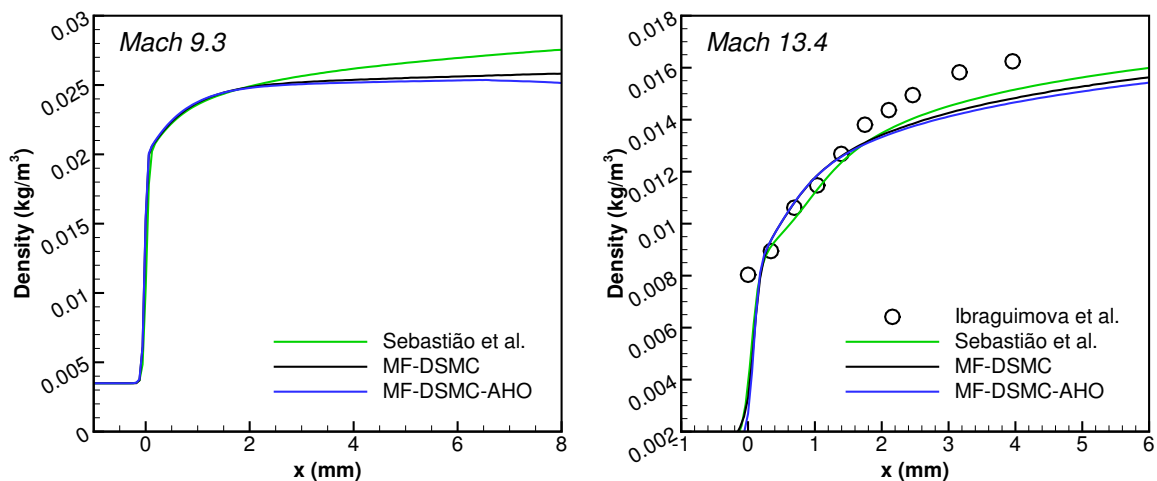


Figure 3.38. Comparison of the density profile for the two cases

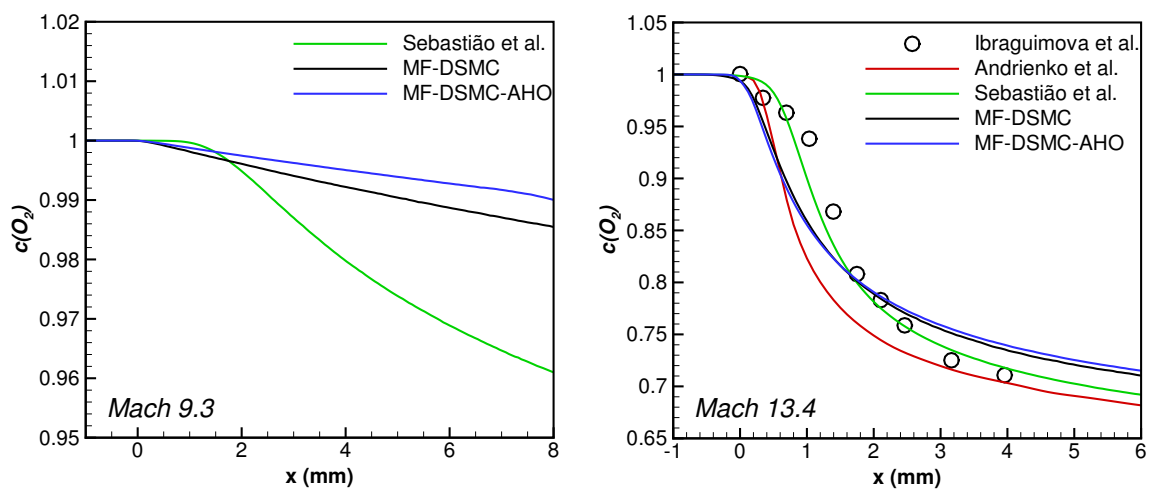


Figure 3.39. Comparison of the O₂ mass fraction for the two cases

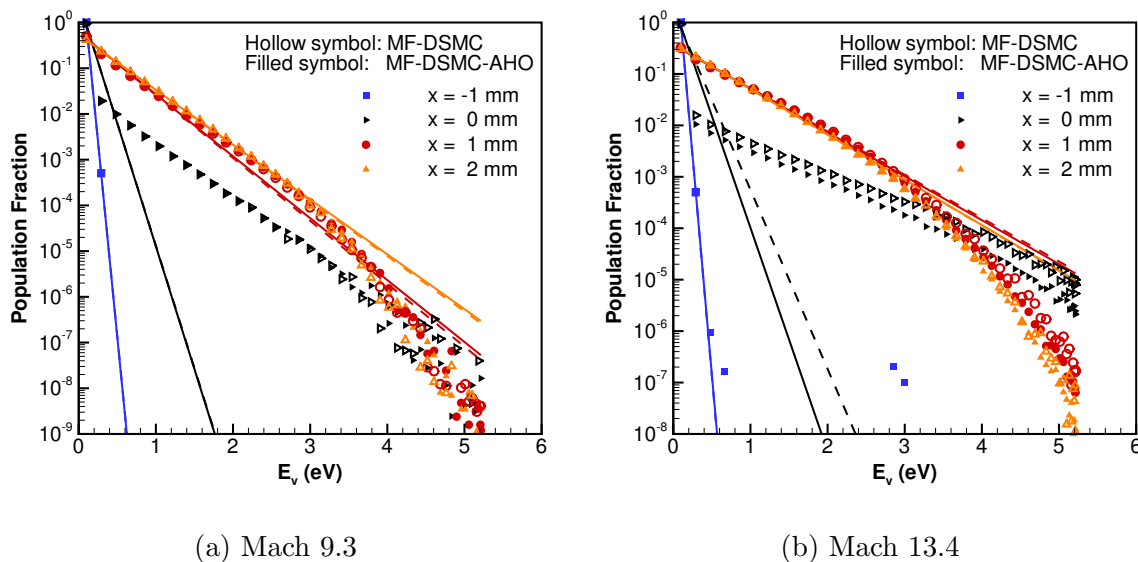


Figure 3.40. Vibrational energy populations of O_2 molecules at different locations across the shock wave for the two cases. Boltzmann distributions characterized by local T_v are shown as dashed lines for MF-DSMC model and solid lines for MF-DSMC-AHO model.

For the Mach 9.3 case, Andrienko *et al.*'s calculations reproduce the vibrational temperature profile before the peak T_v and also the correct value of peak T_v . MF-DSMC, along with Sebastião *et al.*'s simulations underpredict the values but they are within the error bar of measurements. For the region far after the peak T_v , only Sebastião *et al.*'s prediction of T_v is within the uncertainties. All other models underestimate the relaxation of temperatures. This can be understood with the help of comparisons of density and O_2 mass fraction in Figs. 3.38 and 3.39. It is seen that O_2 dissociation in Sebastião *et al.*'s calculations is more than twice as fast as that in the MF-DSMC simulations. The faster dissociation results in higher consumption of energy to break O-O bond and therefore to faster drop of temperatures. There is no distinguishable difference between MF-DSMC and MF-DSMC-AHO model. This is expected since the AHO model only influences the probability of dissociation for

molecules with high vibrational energy while those high levels are less populated in this case as shown in Fig. 3.40a.

For the Mach 13.4 case, Sebastião *et al.*'s simulations give the best agreement in terms of temperature and O₂ mass fraction. However, the models proposed in the present work also reproduce important features of the flow including thermal relaxation right after the shock front and downstream, the profile of density and the mass fraction of O₂ in the downstream. Andrienko's simulation predicts a faster VT relaxation and the translational temperatures are underpredicted. The MF-DSMC and MF-DSMC-AHO model underpredict the peak T_v because the nonequilibrium factor for O₂+O₂ is slightly higher than Sebastião *et al.*'s modeling. In addition, the average vibrational energy removed for O₂ dissociated by O₂ ranges between 1.5 to 3 eV for their simulations, which are below the values predicted by MF-DSMC model as shown in Fig. 3.23. It should be noted that although the local vibrational temperature values given by the two versions of MF-DSMC models are the same at locations $x=1$ mm and $x=2$ mm, MF-DSMC-AHO shows stronger depopulation of vibrationally hot molecules. For these locations, the populations of low vibrational levels molecules have already reached their values corresponding to the Boltzmann distribution but vibrationally hot molecules are still being depleted by the dissociation reaction. Clearly, the traditional Landau-Teller VT relaxation model is unable to reproduce such behavior in CFD, and specific models such as the force harmonic oscillator model [131] would be preferred.

In summary, it is not clear which model is the best one for the simulation due to the different performance for the two cases and the uncertainties of experimental measurements. What is clear is that MF-DSMC and MF-DSMC-AHO model can replace QCT-based state-specific model for simulations of thermal-chemical nonequilibrium reactions without losing much accuracy. From the comparisons, we also see that VT relaxation plays a more important role at relatively low temperatures where the rates of relaxation are higher than chemical reaction rates. In contrast, chemical reaction dominates the energy relaxation behind the shock front at high temperatures.

3.4.7 Summary

In this work, to develop a physics-based model of nonequilibrium dissociation for DSMC, we started from the Macheret-Fridman theory based on the assumption of instantaneous classical collisions and proposed a new implementation of the MF model in DSMC, i.e. MF-DSMC model. The new model was validated by comparison to recent QCT calculations. Very good agreement was obtained for thermochemical nonequilibrium characteristics like vibrational state-specific reaction rates, nonequilibrium factors and average vibrational energy removed by dissociation. To improve the model, we also incorporated the vibrational phase angle calculated with realistic potential energy curve into the model. The improved model, MF-DSMC-AHO, shows better agreement for the prediction of vibrational state-specific rates for molecules with high vibrational energy.

Unlike phenomenological TCE model, which is based on the inverse Laplace transform of Arrhenius reaction rates, MF-DSMC model does not have adjustable parameters to match experimentally measured or theoretically calculated thermal equilibrium reaction rates. After analyzing DSMC algorithm and the physics behind that, we found that as long as the scattering law is independent of the total collision cross sections, it doesn't matter how total collision cross sections are modeled since the transport cross sections are the same. Such flexibility allows us to combine MF-DSMC model with a physically realistic collision model/scattering law and calibrate total collision cross sections. A QCT-based collision model for $\text{N}_2\text{-O}$ and a general collision model based on exponential potential were proposed under such background. The MF-DSMC-EXP model, built upon the general collision model, provides flexibility for MF-DSMC model to match certain thermal equilibration reaction rates. In general, the new models improve the agreement of thermal equilibrium reaction rates. A notable exception is the O_2+O dissociation reaction as MF-DSMC is unable to take electronically excited states into account. Nevertheless, the good agreement

of MF-DSMC model with the QCT calculations for ground electronic state confirms the validity of classical impulsive assumption.

Finally, the MF-DSMC model was implemented in DS1V and used to simulate O₂ shockwave experiment [100]. Good agreement with the measurements as well as with previous state-specific numerical simulations [138, 139] was obtained.

3.5 Summary

Benefiting from the improved ability of *ab initio* QCT calculations, we are now able to develop and validate chemical reaction models by comparing fundamental properties of the reaction instead of conducting trial-and-error study to fit experimental results. The goal of this chapter was to develop consistent thermochemical nonequilibrium dissociation reaction models for both CFD and DSMC. The model should have similar mathematical simplicity as empirical nonequilibrium reaction models but also have physically realistic descriptions of reactions as QCT method does.

To achieve the goal, we started from the Macheret-Fridman theory, i.e. high-energy collisions resulting dissociation can be described by classical mechanics and are close to the impulsive limit, and developed MF-CFD and MF-DSMC models. The models were progressively improved by incorporating more physics and eliminating mathematical approximations. Several effects were found important for the correct description of dissociation reactions, including 1) the reduction of the threshold energy due to the rotation of the dissociating molecule; 2) the increase of the threshold energy due to the centrifugal barrier; 3) the anharmonic vibration of the dissociating molecule; 4) the rate of collisions.

We conducted a systematic study of nonequilibrium reaction characteristics computed with the proposed models. The calculated vibrational state-specific rates, nonequilibrium factors and vibrational-dissociation energy exchange show good agreement with QCT simulations for both diatom-atom and diatom-diatom collisions. The models were also validated by simulating the O₂ reacting shock experiment. The similarity of the results predicted by the models compared to the ones predicted by QCT-based state-specific models confirms the classical impulsive collision assumption is valid for high-energy dissociation reactions.

The present calculations and results indicate the potential of the new models to be used as the standard CFD or DSMC dissociation reaction model.

4. CONCLUSIONS

4.1 Concluding Remarks

The ability to model thermochemical nonequilibrium flow is becoming critical for an increasing need of cost-effective commercial space missions and scientific explorations of other planets. With the recent availability of *ab initio* PESs for gas species of interest, QCT method has almost become routine for the calculations of state-specific relaxation and reaction rates and cross sections. However, to the best of our knowledge, QCT method hasn't been used to study the transport properties at high-temperature thermal nonequilibrium conditions. Besides, there is no clear general technology roadmap for the implementation of QCT data in CFD and DSMC simulations.

In the first part of this work, the thermal nonequilibrium transport properties were studied. By simulating a flow with Mach number 11.3 passing a flat plate with DSMC method, we found vibrational nonequilibrium could result in different values of viscosity than the ones at thermal equilibrium condition. The method of calculating thermal nonequilibrium transport properties with QCT method was formulated based on Wang Chang and Uhlenbeck's theory. The computational results of collision integrals for N₂-O show that the quasi-elastic collision approximation used in conventional calculations is valid for low vibrational levels ($v < 30$) but leads to the underprediction of state-specific collision integrals by up to a factor of two for high vibrational levels. The collisional integrals characterized by both T and T_v show different dependence on T_v for different electronic states. However, the mean collision integrals (weighted by electronic degeneracy) change by less than 5% compared to the thermal equilibrium ones for the condition $T=3,000 \sim 20,000$ K and $|T - T_v| \leq 5,000$ K. Compared to the widely-used values of collision integrals, an

uncertainty of 30~50% was found. It clearly illustrates the importance of studying transport properties by QCT method when available.

In the second part of this work, consistent thermochemical nonequilibrium dissociation reaction models were developed for both CFD and DSMC methods. The models are based on Macheret-Fridman theory of dissociation reactions. The MF-CFD model is a correction and improvement of the old MF model [101]. The importance of rotational-dissociation coupling was addressed. The MF-DSMC model is a new implementation of the theory in DSMC. New influence factors to dissociation reactions, like the anharmonic vibration of the molecule and improved collision models based on either QCT scattering or exponential potential, are included in the implementation. The models predict nonequilibrium characteristics of dissociation reaction in perfect agreement with QCT data. Simulations of O₂ reacting shock further illustrate the potential of the models to be used as the standard CFD or DSMC dissociation reaction model.

In summary, the current work fills the gap between research-oriented *ab initio* QCT method for the calculation of rates and the engineering-oriented CFD and DSMC method for the solution of real-world problem. The proposed models will further improve the predictive capabilities of CFD and DSMC methods for thermochemical nonequilibrium flow.

4.2 Future Work

There are several interesting and meaning topics can be addressed from the current work. The author would like to recommend the following ones,

- **Study the thermal nonequilibrium transport properties for other systems at higher temperatures**

In the current work, the thermal nonequilibrium transport properties were calculated for N₂-O system at temperatures up to 20,000 K. However, the peak temperature of the flow can be as high as 24,000 K for applications like sample return mission from

Mars [143]. The method introduced in the current work should also be used to study transport properties at these conditions.

- **Implementation of MF-CFD and MF-DSMC models in engineering-oriented code**

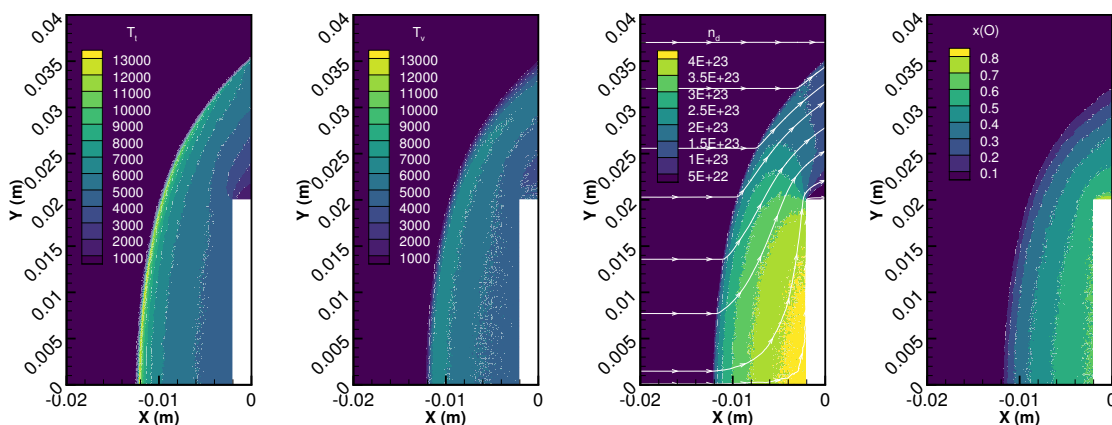
The author of this thesis was focused on the improvement and validation of the thermochemical nonequilibrium dissociation reaction models. Thus the research-oriented DS1V was used as the test platform due to its high performance for 1D simulation. The model has also been successfully implemented in SPARTA DSMC simulator from Sandia National Laboratory as a separate module. This allows people having interest in the model to directly use it for 2D or 3D simulations. To test the implementation, we used the modified SPARTA and simulated the Mach=13.5 O₂ reacting shock experiment introduced in Sec. 3.4.6. Because SPARTA only simulates 2D or 3D flows, a two-dimensional configuration with a high aspect ratio blunt body was set as shown Fig. 4.1. The left and top boundaries were set as inflow boundaries and the free stream condition is the same as the one in Sec. 3.4.6. The periodic boundary condition was employed for the bottom boundary. To minimize the influence of the surface on molecules, specular reflection boundary condition was used to model gas-surface interaction. We used the same physics models as the simulation with MF-DSMC-AHO model in Sec. 3.4.6. However, the numerical parameters of DSMC algorithm are different due to the difference of the code. The number of collision cells N_{coll} , number of sampling cells N_{sample} , size of the collision cell Δx , minimum number of pseudo-particles per collision cell N_{min} , average time step Δt , and number of time steps used for the sampling of macroscopic properties N_t are compared between DS1V and SPARTA in Table 4.1.

The profiles of translational temperature, vibrational temperature, total number density and mole fraction of atomic oxygen are shown in Fig. 4.1. The profiles of temperature and mole fraction of atomic oxygen predicted by SPARTA for the stagnation streamline are compared with DS1V's results in Fig. 4.2. Although the same physics

Table 4.1.: Comparison of numerical parameters used in DS1V and SPARTA

	N_{coll}		N_{sample}		Δx (μm)	N_{min}	Δt (ns)	N_t ($\times 10^4$)
	x	y	x	y				
DS1V	16,000	-	500	-	1.875	12	0.1243	66.2
SPARTA	334	667	334	667	60.000	19	0.1000	3.0

models were used in the simulations, there is noticeable difference between the results. SPARTA predicts higher peak temperatures than DS1V does. It is because the shock wave profile along the stagnation streamline will only approach the 1D profile when the Knudsen number becomes zero, while the Knudsen number is inversely proportional to the characteristic length of the blunt body. To improve the agreement, we need to increase the size of the blunt body and the number of pseudo-particles, which will make the computation more expensive.

Figure 4.1. Simulation of the Mach=13.5 O₂ reacting shock with MF-DSMC-AHO model in SPARTA

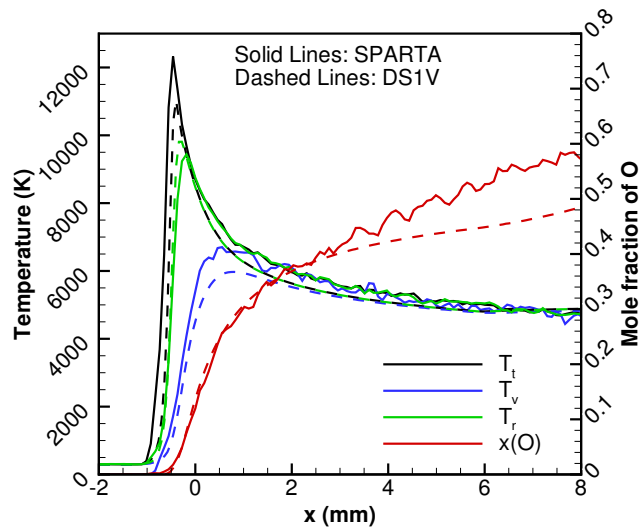


Figure 4.2. Comparison of the shock profile predicted by SPARTA and DS1V for the Mach=13.5 O_2 reacting shock

- **Use MF-DSMC model to study post-reaction energy distribution**

Due to the arising interest of Martian exploration, Mars sample-return (MSR) missions are foreseeable in the near future. A critical flow regime with a free stream velocity of 11 to 15 km/s will be experienced during the Earth's entry in a MSR mission [144]. In such a hyper-velocity flight, a total enthalpy of more than 82 MJ/kg is expected [145], which makes thermochemical nonequilibrium more pronounced. As a preliminary study, we used the MF-DSMC model and simulated a hypothetical 1D shock wave to get an understanding of the problem we will be faced with. The simulation result of a 14 km/s O_2 reacting shock is shown in Fig. 4.3. Ionization and radiation are not considered in the simulation. As a result, the temperature becomes incredibly high. The peak translational temperature is about 6 eV. Thus, oxygen molecules get fully dissociated after the shock front. There also exists translational nonequilibrium which is expected. However, an interesting effect we found is that O_2 dissociation occurs not only before vibrational excitation begins, but also when translational relaxation is incomplete. There are two couplings, namely vibration-

dissociation coupling and translation-dissociation coupling. Besides, we found there are super-hot oxygen atoms spread from the shock front to the end of the shock. Their translational temperature is always higher than the average translational temperature. Besides possible numerical issue of the simulation method, a possible physical explanation is the failure of Larsen-Borgnakke model used by DSMC for the post-reaction energy redistribution. Since MF-DSMC model directly solves the post-collision velocities of each atoms, it can also be used to calculate post-dissociation energy of the particles, which will give us a better understanding of the effect.

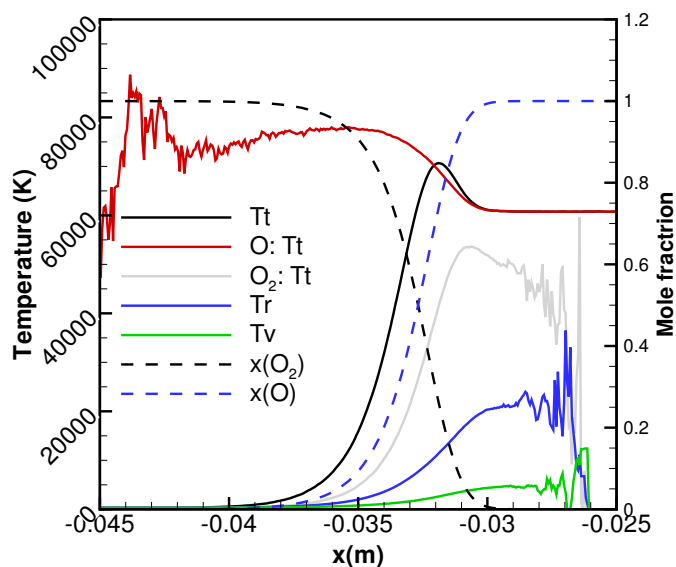


Figure 4.3. Temperatures and mole fractions of 14 km/s O_2 reacting shock

REFERENCES

REFERENCES

- [1] N. M. Laurendeau. *Statistical thermodynamics: fundamentals and applications*. Cambridge University Press, 2005.
- [2] H. H. Reising, K. C. U., S. Voelkel, N. T. Clemens, V. Raman, P. L. Varghese, and H. Koo. Vibrational non-equilibrium effects in supersonic jet mixing. In *52nd AIAA Aerospace Sciences Meeting*, AIAA Paper 2014-0231, jan 2014.
- [3] A. A. Fridman and L. A. Kennedy. *Plasma Physics and Engineering*. CRC Press, 2011.
- [4] C. P. Gendrich, M. M. Koochesfahani, and D. G. Nocera. Molecular tagging velocimetry and other novel applications of a new phosphorescent supramolecule. *Experiments in Fluids*, 23(5):361–372, nov 1997.
- [5] Y. Liu, D. Prabhu, K. A. Trumble, D. Saunders, and P. Jenniskens. Radiation Modeling For the Reentry of the Stardust Sample Return Capsule. *Journal of Spacecraft and Rockets*, 47(5):741–752, sep 2010.
- [6] P. A. Gnoffo, K. James Weilmuenster, R. D. Braun, and C. I. Cruz. Influence of sonic-line location on Mars Pathfinder Probe aerothermodynamics. *Journal of Spacecraft and Rockets*, 33(2):169–177, mar 1996.
- [7] M. Schoenenberger, F. McNeil Cheatwood, and P. Desai. Static aerodynamics of the mars exploration rover entry capsule. In *43rd AIAA Aerospace Sciences Meeting and Exhibit*. American Institute of Aeronautics and Astronautics, jan 2005.
- [8] K. T. Edquist, P. N. Desai, and M. Schoenenberger. Aerodynamics for Mars Phoenix Entry Capsule. *Journal of Spacecraft and Rockets*, 48(5):713–726, sep 2011.
- [9] A. M. Korzun, R. W. Maddock, M. Schoenenberger, K. T. Edquist, C. H. Zumwalt, and C. D. Karlgaard. Aerodynamic Performance of the 2018 InSight Mars Lander. In *AIAA Scitech 2020 Forum*. American Institute of Aeronautics and Astronautics, jan 2020.
- [10] I. Nompelis, G. V. Candler, and M. S. Holden. Effect of Vibrational Nonequilibrium on Hypersonic Double-Cone Experiments. *AIAA Journal*, 41(11):2162–2169, nov 2003.
- [11] D. A. Levin, G. V. Candler, R. J. Collins, P. W. Erdman, E. Zipf, P. Espy, and C. Howlett. Comparison of theory with experiment for the bow shock ultraviolet rocket flight. *Journal of Thermophysics and Heat Transfer*, 7(1):30–36, jan 1993.

- [12] J. D Anderson Jr. *Hypersonic and high-temperature gas dynamics*. American Institute of Aeronautics and Astronautics, 2006.
- [13] R. Wagnild, G. Candler, P. Subbareddy, and H. Johnson. Vibrational Relaxation Effects on Acoustic Disturbances in a Hypersonic Boundary Layer over a Cone. In *50th AIAA Aerospace Sciences Meeting including the New Horizons Forum and Aerospace Exposition*. American Institute of Aeronautics and Astronautics, jan 2012.
- [14] Z. Li, I. Sohn, and D. Levin. DSMC Modeling of NO Formation for Simulation of Radiation in Hypersonic Flows. In *50th AIAA Aerospace Sciences Meeting including the New Horizons Forum and Aerospace Exposition*. American Institute of Aeronautics and Astronautics, jan 2012.
- [15] I. D. Boyd, G. V. Candler, and D. A. Levin. Dissociation modeling in low density hypersonic flows of air. *Physics of Fluids*, 7(7):1757–1763, 1995.
- [16] M. W. Winter and K. A. Trumble. Near-Ultraviolet Emission Spectroscopy During an Airborne Observation of the Stardust Reentry. *Journal of Spacecraft and Rockets*, 48(1):59–71, jan 2011.
- [17] H. Alsmeyer. Density profiles in argon and nitrogen shock waves measured by the absorption of an electron beam. *Journal of Fluid Mechanics*, 74(03):497, apr 1976.
- [18] K. L. Wray and J. Derek Teare. Shock-Tube Study of the Kinetics of Nitric Oxide at High Temperatures. *The Journal of Chemical Physics*, 36(10):2582–2596, may 1962.
- [19] M. Camac and A. Vaughan. O₂ Dissociation Rates O₂-Ar Mixtures. *The Journal of Chemical Physics*, 34(2):460–470, feb 1961.
- [20] J. P. Rink, H. T. Knight, and R. E. Duff. Shock tube determination of dissociation rates of oxygen. *The Journal of Chemical Physics*, 34(6):1942–1947, jun 1961.
- [21] S. R. Byron. Measurement of the rate of dissociation of oxygen. *The Journal of Chemical Physics*, 30(6):1380–1392, jun 1959.
- [22] J. P. Appleton, M. Steinberg, and D. J. Liquornik. Shock-tube study of nitrogen dissociation using vacuum-ultraviolet light absorption. *The Journal of Chemical Physics*, 48(2):599–608, jan 1968.
- [23] J. P. JP Monat, R. K. Hanson, and C. H. CH Kruger. Shock tube determination of the rate coefficient for the reaction $N_2+O\rightarrow NO+N$. *Symposium (International) on Combustion*, 17(1):543–552, 1979.
- [24] D. L. Matthews. Interferometric Measurement in the Shock Tube of the Dissociation Rate of Oxygen. *Physics of Fluids*, 2(2):170, 1959.
- [25] B. Cary. Shock-Tube Study of the Termal Dissociation of Nitrogen. *Physics of Fluids*, 8(1):26, 1965.
- [26] R. K. Hanson and D. Baganoff. Shock-Tube Study of Nitrogen Dissociation Rates Using Pressure Measurements. *AIAA Journal*, 10(2):211–215, feb 1972.

- [27] C. Park. *Nonequilibrium Hypersonic Aerothermodynamics*. New York: Wiley, 1989.
- [28] D. L. Baulch, D. D. Drysdale, J. Duxbury, and S. J. Grant. *Evaluated Kinetic Data for High Temperature Reactions, Vol. 3: Homogeneous Gas Phase Reactions of the O₂-O₃ System*. Number pp. 595. Butterworths, London, 1976.
- [29] K. L. Wray. Chemical Kinetics of High Temperature Air. In *Hypersonic Flow Research*, volume 04, pages 181–204. American Institute of Aeronautics and Astronautics, New York, jan 1962.
- [30] M. H. Bortner. A Review Of Rate Constants Of Selected Reactions Of Interest In Re-Entry Flow Fields In The Atmosphere.
- [31] B. A. Cruden. Absolute radiation measurements in earth and mars entry conditions. Technical report, NASA Ames Research Center, 2014.
- [32] L. Landau and E. Teller. Zur theorie der schalldispersion. *Phys. Z. Sowjetunion*, 10(1):34, 1936.
- [33] C. Park. Review of chemical-kinetic problems of future NASA missions. I-Earth entries. *Journal of Thermophysics and Heat transfer*, 7(3):385–398, 1993.
- [34] P. V. Marrone and C. E. Treanor. Chemical Relaxation with Preferential Dissociation From Excited Vibrational Levels. *Physics of Fluids*, 6(9):1215–1221, 1963.
- [35] O. Knab, H.-H. Fruehauf, and E. W. Messerschmid. Theory and validation of the physically consistent coupled vibration-chemistry-vibration model. *Journal of Thermophysics and Heat Transfer*, 9(2):219–226, apr 1995.
- [36] G. A. Bird. *Molecular Gas Dynamics and the Direct Simulation of Gas Flows*. Oxford University Press, New York, 1994.
- [37] I. D. Boyd. Analysis of vibration-dissociation-recombination processes behind strong shock waves of nitrogen. *Physics of Fluids*, 4(1):178–185, jan 1992.
- [38] I. J. Wysong and S. F. Gimelshein. Comparison of DSMC reaction models with QCT reaction rates for nitrogen. *AIP Conference Proceedings*, 1786(1):050021, 2016.
- [39] S. Gimelshein and I. Wysong. DSMC modeling of flows with recombination reactions. *Physics of Fluids*, 29(6):067106, jun 2017.
- [40] G. A. Bird. The Q-K model for gas-phase chemical reaction rates. *Physics of Fluids*, 23(10):106101, oct 2011.
- [41] B. A. Cruden and A. M. Brandis. Measurement of Radiative Non-equilibrium for Air Shocks Between 7-9 km/s. In *47th AIAA Thermophysics Conference*, AIAA Paper 2017-4535, jun 2017.
- [42] F. Esposito, C. Maria Coppola, and D. De Fazio. Complementarity between Quantum and Classical Mechanics in Chemical Modeling. The H+HeH⁺ → H₂⁺+He Reaction: A Rigorous Test for Reaction Dynamics Methods. *The Journal of Physical Chemistry*, 119(51):12615–12626, dec 2015.

- [43] M. Karplus, R. Porter, and R. Sharma. Exchange Reactions with Activation Energy. I. Simple Barrier Potential for (H, H₂). *The Journal of Chemical Physics*, 43(9):3259–3287, 1965.
- [44] D. G. Truhlar, J. T. Muckerman, and R. B. Bernstein. *Atom-Molecule Collision Theory: A Guide for the Experimentalist*. Plenum, New York, 1979.
- [45] D. G. Hopper. Ab initio multiple root optimization MCSCF study of the $C_{\infty v}/C_s$ excitation spectra and potential energy surfaces of N₂O. *The Journal of Chemical Physics*, 80(9):4290, 1984.
- [46] S. P. Walch and R. L. Jaffe. Calculated potential surfaces for the reactions: O+N₂ →NO+N and N+O₂ →NO+O. *The Journal of Chemical Physics*, 86(12):6946–6956, jun 1987.
- [47] H. Nakamura and S. Kato. Theoretical study on the spin-forbidden predissociation reaction of N₂O: Ab initio potential energy surfaces and quantum dynamics calculations. *The Journal of Chemical Physics*, 110(20):9937–9947, may 1999.
- [48] M. González, R. Valero, and R. Sayós. Ab initio and quasiclassical trajectory study of the N(²D)+NO(X²Π)→O(¹D)+N₂(X¹Σ_g⁺) reaction on the lowest ¹A' potential energy surface. *The Journal of Chemical Physics*, 113(24):10983, 2000.
- [49] P. Gamallo, M. González, and R. Sayós. Ab initio derived analytical fits of the two lowest triplet potential energy surfaces and theoretical rate constants for the N(⁴S)+NO(X²Π) system. *The Journal of Chemical Physics*, 119(5):2545–2556, 2003.
- [50] W. Lin, Z. Varga, G. Song, Y. Paukku, and D. G. Truhlar. Global triplet potential energy surfaces for the N₂(X¹Σ)+O(³P)→NO(X²Π)+N(⁴S) reaction. *The Journal of Chemical Physics*, 144(2):024309, 2016.
- [51] R. Jaffe, D. Schwenke, and G. Chaban. Theoretical analysis of N₂ collisional dissociation and rotation-vibration energy transfer. In *47th AIAA Aerospace Sciences Meeting*, AIAA Paper 2009-1569, jan 2009.
- [52] F. Esposito, I. Armenise, and M. Capitelli. N-N₂ state to state vibrational-relaxation and dissociation rates based on quasiclassical calculations. *Chemical Physics*, 331(1):1–8, dec 2006.
- [53] F. Esposito, I. Armenise, G. Capitta, and M. Capitelli. O-O₂ state-to-state vibrational relaxation and dissociation rates based on quasiclassical calculations. *Chemical Physics*, 351(1):91–98, jul 2008.
- [54] M. Kulakhmetov, M. Gallis, and A. Alexeenko. Ab initio-informed maximum entropy modeling of rovibrational relaxation and state-specific dissociation with application to the O₂+O system. *The Journal of Chemical Physics*, 144(17):174302, 2016.
- [55] D. A. Andrienko and I. D. Boyd. Rovibrational energy transfer and dissociation in O₂-O collisions. *The Journal of Chemical Physics*, 144(10):104301, mar 2016.
- [56] H. Luo, M. Kulakhmetov, and A. Alexeenko. Ab initio state-specific N₂+O dissociation and exchange modeling for molecular simulations. *The Journal of Chemical Physics*, 146(7):074303, 2017.

- [57] F. Esposito and I. Armenise. Reactive, inelastic, and dissociation processes in collisions of atomic oxygen with molecular nitrogen. *The Journal of Physical Chemistry*, 121(33):6211–6219, aug 2017.
- [58] J. D. Bender, P. Valentini, I. Nompelis, Y. Paukku, Z. Varga, D. G. Truhlar, T. Schwartzentruber, and G. V. Candler. An improved potential energy surface and multi-temperature quasiclassical trajectory calculations of N_2+N_2 dissociation reactions. *The Journal of Chemical Physics*, 143(5):054304, 2015.
- [59] D. A. Andrienko and I. D. Boyd. State-specific dissociation in O_2-O_2 collisions by quasiclassical trajectory method. *Chemical Physics*, 491:74–81, jul 2017.
- [60] R. S. Chaudhry and G. V. Candler. Statistical Analyses of Quasiclassical Trajectory Data for Air Dissociation. In *AIAA Scitech 2019 Forum*, AIAA Paper 2019-0789, jan 2019.
- [61] R. Chaudhry. *Modeling and Analysis of Chemical Kinetics for Hypersonic Flows in Air*. PhD thesis, University of Minnesota, 2018.
- [62] D. A. Andrienko and I. D. Boyd. Dissociation of oxygen and nitrogen in a bimolecular reaction at hypersonic temperatures. In *2018 AIAA Aerospace Sciences Meeting*, AIAA Paper 2018-0240, jan 2018.
- [63] D. A. Andrienko and I. D. Boyd. State-resolved characterization of nitric oxide formation in shock flows. In *2018 AIAA Aerospace Sciences Meeting*, AIAA Paper 2018-1233, jan 2018.
- [64] P. Defazio, P. Gamallo, and C. Petrongolo. Nonadiabatic dynamics of $O(^1D) + N_2(X^1\Sigma_g^+) \rightarrow O(^3P) + N_2(X^1\Sigma_g^+)$ on three coupled potential surfaces: Symmetry, Coriolis, spin-orbit, and Renner-Teller effects. *The Journal of Chemical Physics*, 136:054308, 2012.
- [65] H. Luo, S. Macheret, and A. Alexeenko. Quasi-classical Trajectory Studies of N_2+O Collisions: Trajectory Patterns and Long-lived Configurations. In *47th AIAA Thermophysics Conference*. American Institute of Aeronautics and Astronautics, jun 2017.
- [66] Y. Paukku, K. R. Yang, Z. Varga, G. Song, J. D. Bender, and D. G. Truhlar. Potential energy surfaces of quintet and singlet O_4 . *The Journal of Chemical Physics*, 147(3):034301, jul 2017.
- [67] N. Singh and T. E. Schwartzentruber. Coupled Vibration-Rotation Dissociation Model for Nitrogen from Direct Molecular Simulations. In *47th AIAA Thermophysics Conference*. AIAA Paper 2017-3490, 2017.
- [68] R. N Gupta, J. M Yos, R. A Thompson, and K. Lee. A review of reaction rates and thermodynamic and transport properties for an 11-species air model for chemical and thermal nonequilibrium calculations to 30,000 K. *NASA Reference Publication 1232*, 1990.
- [69] G. Palmer. Uncertainty analysis of CEV LEO and lunar return entries. In *39th AIAA Thermophysics Conference*, AIAA Paper 2007-4253, jan 2007.

- [70] A. V. Phelps. Cross Sections and Swarm Coefficients for Nitrogen Ions and Neutrals in N_2 and Argon Ions and Neutrals in Ar for Energies from 0.1 eV to 10 keV. *Journal of Physical and Chemical Reference Data*, 20(3):557–573, may 1991.
- [71] G. C. Maitland and E. Brian Smith. Critical reassessment of viscosities of 11 common gases. *Journal of Chemical & Engineering Data*, 17(2):150–156, apr 1972.
- [72] M. J. Wright, D. Bose, G. E. Palmer, and E. Levin. Recommended Collision Integrals for Transport Property Computations Part 1: Air Species. *AIAA Journal*, 43(12):2558–2564, dec 2005.
- [73] J. R. Stallcop, H. Partridge, and E. Levin. Effective potential energies and transport cross sections for atom-molecule interactions of nitrogen and oxygen. *Physical Review A*, 64(4), sep 2001.
- [74] M. Capitelli, C. Gorse, S. Longo, and D. Giordano. Collision integrals of high-temperature air species. *Journal of Thermophysics and Heat Transfer*, 14(2):259–268, apr 2000.
- [75] E. Levin and M. J. Wright. Collision Integrals for Ion-Neutral Interactions of Nitrogen and Oxygen. *Journal of Thermophysics and Heat Transfer*, 18(1):143–147, jan 2004.
- [76] E. A. Mason and L. Monchick. Heat conductivity of polyatomic and polar gases. *The Journal of Chemical Physics*, 36(6):1622–1639, mar 1962.
- [77] A. W. Jasper, E. Kamarchik, J. A. Miller, and S. J. Klippenstein. First-principles binary diffusion coefficients for H, H_2 , and four normal alkanes+ N_2 . *The Journal of Chemical Physics*, 141(12):124313, sep 2014.
- [78] P. J. Dagdigian and M. H. Alexander. Exact Quantum Scattering Calculation of Transport Properties for Free Radicals: OH($X^2\Pi$)-helium. *The Journal of Chemical Physics*, 137(9):094306, sep 2012.
- [79] K. Koura and H. Matsumoto. Variable soft sphere molecular model for inverse-power-law or Lennard Jones potential. *Physics of Fluids*, 3(10):2459–2465, 1991.
- [80] A. Kersch, W. Morokoff, and Chr. Werner. Selfconsistent simulation of sputter deposition with the Monte Carlo method. *Journal of Applied Physics*, 75(4):2278–2285, feb 1994.
- [81] J. Kim and I. D. Boyd. State resolved thermochemical modeling of nitrogen using DSMC. In *43rd AIAA Thermophysics Conference*, AIAA Paper 2012-2991, jun 2012.
- [82] T. Zhu, Z. Li, and D. A. Levin. Development of a two-dimensional binning model for N_2 -N relaxation in hypersonic shock conditions. *The Journal of Chemical Physics*, 145(6):064302, aug 2016.
- [83] W. Wang, I. Boyd, G. Candler, and I. Nompelis. Particle and continuum computations of hypersonic flow over sharp and blunted cones. In *35th AIAA Thermophysics Conference*. American Institute of Aeronautics and Astronautics, jun 2001.

- [84] S. J. Plimpton, S. G. Moore, A. Borner, A. K. Stagg, T. P. Koehler, J. R. Torczynski, and M. A. Gallis. Direct simulation Monte Carlo on petaflop supercomputers and beyond. *Physics of Fluids*, 31(8):086101, aug 2019.
- [85] G. V. Candler, H. B. Johnson, I. Nompelis, V. M. Gidzak, P. K. Subbareddy, and M. Barnhardt. Development of the US3D Code for Advanced Compressible and Reacting Flow Simulations. In *53rd AIAA Aerospace Sciences Meeting*. American Institute of Aeronautics and Astronautics, jan 2015.
- [86] J. Zheng, Z. Hua Li, A. W. Jasper, D. A. Bonhommeau, R. Valero, R. Meana-Paneda, S. L. Mielke, and D. G. Truhlar. ANT, version 2016. Technical report, University of Minnesota, 2016.
- [87] J. Hirschfelder, C. F. Curtiss, and R. Byron Bird. *Molecular theory of gases and liquids*. Wiley, 1964.
- [88] J. H. Ferziger and H. G. Kaper. *Mathematical theory of transport processes in gases*, volume 41. Elsevier, 1973.
- [89] A. H. H. Chang and D. R. Yarkony. On the electronic structure aspects of spin-forbidden processes in N_2O . *The Journal of Chemical Physics*, 99(9):6824–6831, 1993.
- [90] B. Brunetti, G. Liuti, E. Luzzatti, F. Pirani, and F. Vecchiocattivi. Study of the interactions of atomic and molecular oxygen with O_2 and N_2 by scattering data. *The Journal of Chemical Physics*, 74:6734–6741, 1981.
- [91] V. B Leonas. Studies of short-range intermolecular forces. *Soviet Physics Uspekhi*, 15(3):266, 1972.
- [92] J. T. Vanderslice, E. A. Mason, and W. G. Maisch. Interactions between Oxygen and Nitrogen: $O-N$, $O-N_2$, and O_2-N_2 . *The Journal of Chemical Physics*, 31(3):738–746, 1959.
- [93] H. Luo, A. A. Alexeenko, and S. O. Macheret. Assessment of classical impulsive models of dissociation in thermochemical nonequilibrium. *Journal of Thermophysics and Heat Transfer*, pages 1–8, jan 2018.
- [94] K. S. Yun and E. A. Mason. Collision Integrals for the Transport Properties of Dissociating Air at High Temperatures. *Physics of Fluids*, 5(4):380–386, 1962.
- [95] A. B. Murphy. Transport coefficients of air, argon-air, nitrogen-air, and oxygen-air plasmas. *Plasma Chemistry and Plasma Processing*, 15:279–307, 1995.
- [96] I. D. Boyd. A threshold line dissociation model for the direct simulation Monte Carlo method. *Physics of Fluids*, 8(5):1293–1300, 1996.
- [97] D. Yap, J. Tatibouët, and C. Batiot-Dupeyrat. Carbon dioxide dissociation to carbon monoxide by non-thermal plasma. *Journal of CO2 Utilization*, 12(Supplement C):54–61, 2015.
- [98] D. Hash, J. Olejniczak, M. Wright, D. Prabhu, M. Pulsonetti, B. Hollis, P. Gnoffo, M. Barnhardt, I. Nompelis, and G. Candler. FIRE II Calculations for Hypersonic Nonequilibrium Aerothermodynamics Code Verification: DPLR, LAURA, and US3D. In *45th AIAA Aerospace Sciences Meeting and Exhibit*, AIAA Paper 2007-605, jan 2007.

- [99] K. G. Owen, D. F. Davidson, and R. K. Hanson. Oxygen Vibrational Relaxation Times: Shock Tube/Laser Absorption Measurements. *Journal of Thermophysics and Heat Transfer*, 30(4):791–798, oct 2016.
- [100] L. B. Ibraguimova, A. L. Sergievskaya, V. Y. Levashov, O. P. Shatalov, Y. V. Tunik, and I. E. Zabelinskii. Investigation of oxygen dissociation and vibrational relaxation at temperatures 4000-10800K. *The Journal of Chemical Physics*, 139(3):034317, jul 2013.
- [101] S. O. Macheret, A. A. Fridman, I. V. Adamovich, J. W. Rich, and C. E. Treanor. Mechanisms of nonequilibrium dissociation of diatomic molecules. In *6th Joint Thermophysics and Heat Transfer Conference*, AIAA Paper 1994-1984, 1994.
- [102] S. O. Macheret and J. W. Rich. Theory of nonequilibrium dissociation rates behind strong shock waves. In *28th Thermophysics Conference*, AIAA Paper 1993-2860, 1993.
- [103] S. O. Macheret and J. W. Rich. Nonequilibrium dissociation rates behind strong shock waves: classical model. *Chemical Physics*, 174(1):25–43, jul 1993.
- [104] G. G. Chernyi, S. A. Losev, S. O. Macheret, and B. V. Potapkin. *Physical and Chemical Processes in Gas Dynamics, Vol. I: Cross Sections and Rate Constants*. AIAA, 2002.
- [105] D. C. Wadsworth and I. J. Wysong. Vibrational favoring effect in DSMC dissociation models. *Physics of Fluids*, 9(12):3873–3884, dec 1997.
- [106] S. A. Losev, V. N. Makarov, M. J. Pogosbekyan, O. P. Shatalov, and V. S. Nikolsky. Thermochemical nonequilibrium kinetic models in strong shock waves on air. In *6th Joint Thermophysics and Heat Transfer Conference*, AIAA Paper 1994-1990, 1994.
- [107] M. S. Yalovik and S. A. Losev. Vibrational kinetics and dissociation of nitrogen molecules at high temperature. *Scientific Proceedings, Institute of Mechanics, Mosc. State Univ*, 18:3–34, 1972.
- [108] M. S. Grover and T. E. Schwartzenruber. Internal energy relaxation and dissociation in molecular oxygen using direct molecular simulation. In *47th AIAA Thermophysics Conference*, AIAA Paper 2017-3488, jun 2017.
- [109] S. O. Macheret and I. V. Adamovich. Semiclassical Modeling of State-Specific Dissociation Rates in Diatomic Gases. *Journal of Chemical Physics*, 113(17):7351–7361, 2000.
- [110] L. B. Ibraguimova, O. P. Shatalov, Yu. V. Tunik, and I. E. Zabelinskii. Shock Tube Investigation of Molecular Oxygen Dissociation at Temperatures of 4000 to 10800 K. In *28th International Symposium on Shock Waves*, volume 1, pages 125–130. Springer, Berlin, Heidelberg, 2012.
- [111] I. E. Zabelinskii, L. B. Ibraguimova, O. P. Shatalov, and Yu. V. Tunik. Experimental Study and Numerical Modeling of Vibrational Oxygen Temperature Profiles Behind a Strong Shock Wave Front. In *Progress in Flight Physics*, volume 3, pages 231–242, Les Ulis, France, 2012. EDP Sciences.

- [112] D. F Potter. *Modelling of radiating shock layers for atmospheric entry in Mars and Earth*. Ph.D. Dissertation, University of Queensland, Australia, 2011.
- [113] O. P. Shatalov. Molecular dissociation of oxygen in the absence of vibrational equilibrium. *Combust. Explo. Shock Waves*, 9(5):610–613, Sep 1973.
- [114] S. A Losev. Modelling Results on Physical and Chemical Processes in Thermally Nonequilibrium High-Temperature Gas. In *West-East High Speed Flow Field Conference*, Moscow, Russia, 2006.
- [115] J. E. Breen, R. B. Quay, and G. P. Glass. Vibrational Relaxation of O₂ in the Presence of Atomic Oxygen. *The Journal of Chemical Physics*, 59(1):556–557, jul 1973.
- [116] D. A. Andrienko and I. D. Boyd. Master Equation Study of Vibrational and Rotational Relaxation of Oxygen. In *45th AIAA Thermophysics Conference*, page 3252, 2015.
- [117] R. C. Millikan and D. R. White. Systematics of Vibrational Relaxation. *The Journal of Chemical Physics*, 39(12):3209–3213, dec 1963.
- [118] C. Borgnakke and P. S. Larsen. Statistical collision model for Monte Carlo simulation of polyatomic gas mixture. *Journal of Computational Physics*, 18(4):405–420, aug 1975.
- [119] G. A. Bird. *The DSMC Method*. CreateSpace Independent Publishing Platform, 2013.
- [120] I. Wysong, S. Gimelshein, Y. Bondar, and M. Ivanov. Comparison of direct simulation Monte Carlo chemistry and vibrational models applied to oxygen shock measurements. *Physics of Fluids*, 26(4):043101, apr 2014.
- [121] R. S. Chaudhry, J. D. Bender, T. E. Schwartzentruber, and G. V. Candler. Quasiclassical trajectory analysis of N₂+N₂ and implications for hypersonic CFD. In *47th AIAA Thermophysics Conference*, AIAA Paper 2017-3167, jun 2017.
- [122] R. S. Chaudhry, M. S. Grover, J. D. Bender, T. E. Schwartzentruber, and G. V. Candler. Quasiclassical trajectory analysis of oxygen dissociation via O₂, O, and N₂. In *2018 AIAA Aerospace Sciences Meeting*, AIAA Paper 2018-0237, jan 2018.
- [123] S. Byron. Shock-tube measurement of the rate of dissociation of nitrogen. *The Journal of Chemical Physics*, 44(4):1378–1388, feb 1966.
- [124] L. Jerig, J. Thielen, and P. Roth. High-temperature dissociation of oxygen diluted in argon or nitrogen. *AIAA Journal*, 29(7):1136–1139, jul 1991.
- [125] O. P. Shatalov. Recommended data on rate constants of physical and chemical processes in N-O atoms system. Technical report, 1987.
- [126] M. H. Bortner. A review of rate constants of selected reactions of interest in re-entry flow fields in the atmosphere. Technical report, National Bureau of Standards, 1969.

- [127] A. B. Weaver and A. A. Alexeenko. Revised variable soft sphere and Lennard-Jones model parameters for eight common gases up to 2200K. *Journal of Physical and Chemical Reference Data*, 44(2):023103, jun 2015.
- [128] W. L. Dimpfl, I. J. Wysong, S. F. Gimelshein, M. Braunstein, and L. S. Bernstein. Application of the Born-Mayer Potential with a Hard-Sphere Scattering Kernel to Rarefied Hyperthermal Gas Flow Modeling. *AIP Conference Proceedings*, 1084(1):323–328, 2008.
- [129] L. Monchick. Collision Integrals for the Exponential Repulsive Potential. *Physics of Fluids*, 2(6):695, 1959.
- [130] E. A. Mason. Transport Properties of Gases Obeying a Modified Buckingham (Exp-Six) Potential. *Journal of Chemical Physics*, 22(2):169–186, feb 1954.
- [131] I. V. Adamovich, S. O. Macheret, J. W. Rich, and C. E. Treanor. Vibrational energy transfer rates using a forced harmonic oscillator model. *Journal of Thermophysics and Heat Transfer*, 12(1):57–65, jan 1998.
- [132] G. Due Billing and E. R. Fisher. VV and VT rate coefficients in H₂ by a quantum-classical model. *Chemical Physics*, 18(1-2):225–232, dec 1976.
- [133] G. Due Billing and E. R. Fisher. VV and VT rate coefficients in N₂ by a quantum-classical model. *Chemical Physics*, 43(3):395–401, nov 1979.
- [134] G. Due Billing. VV and VT rates in N₂-O₂ collisions. *Chemical Physics*, 179(3):463–467, feb 1994.
- [135] N. Gimelshein, S. Gimelshein, and D. Levin. Vibrational relaxation rates in the direct simulation Monte Carlo method. *Physics of Fluids*, 14:4452–4455, 2002.
- [136] W. C. DeMarcus. Classical motion of a Morse oscillator. *American Journal of Physics*, 46(7):733–734, jul 1978.
- [137] D. D. Konowalow and J. O. Hirschfelder. Morse Potential Parameters for O-O, N-N, and N-O Interactions. *Physics of Fluids*, 4(5):637, 1961.
- [138] D. A. Andrienko and I. D. Boyd. Vibrational relaxation and dissociation in O₂-O mixtures. In *46th AIAA Thermophysics Conference*, AIAA Paper 2016-4021, jun 2016.
- [139] I. B. Sebastião, M. Kulakhmetov, and A. Alexeenko. DSMC study of oxygen shockwaves based on high-fidelity vibrational relaxation and dissociation models. *Physics of Fluids*, 29(1):017102, jan 2017.
- [140] O. Kunova, E. Kustova, and A. Savelev. Generalized Treanor-Marrone model for state-specific dissociation rate coefficients. *Chemical Physics Letters*, 659:80–87, aug 2016.
- [141] B. L. Haas, D. B. Hash, G. A. Bird, F. E. Lumpkin, and H. A. Hassan. Rates of thermal relaxation in direct simulation Monte Carlo methods. *Physics of Fluids*, 6(6):2191–2201, jun 1994.
- [142] J. G. Parker. Rotational and Vibrational Relaxation in Diatomic Gases. *Physics of Fluids*, 2(4):449, 1959.

- [143] J. T. Howe. Hypervelocity Atmospheric Flight: Real Gas Flow Fields. Technical report, NASA Ames Research Center, 1989.
- [144] T. Rivell. Notes on Earth Atmospheric Entry for Mars Sample Return Missions. Technical report, NASA Ames Research Center, 2006.
- [145] G. Herdrich, M. Fertig, and S. Lohle. Experimental simulation of high enthalpy planetary entries. *The Open Plasma Physics Journal*, 2(1):150–164, dec 2009.

VITA

VITA

Han Luo

RESEARCH INTERESTS

Hypersonic aerothermodynamics, nonequilibrium and chemical reacting flow, plasma dynamics, gas radiation, computational fluid dynamics, particle-based simulation methods, large scale parallel computing

EDUCATION

Purdue University - West Lafayette, IN Aug 2020

Ph.D. in Aeronautical and Astronautical Engineering

Major: Aerodynamics, Minor: Propulsion

Thesis Topic: Multiscale Computational Analysis and Modeling of Thermochemical Nonequilibrium Flow

Purdue University - West Lafayette, IN Aug 2016

M.S. in Aeronautical and Astronautical Engineering

Major: Aerodynamics, Minor: Computer Science and Engineering

Thesis Topic: Ab-initio based State-Specific Modeling of N₂-O System

Beihang University - Beijing, China Jun 2014

B.S.E. in Aerospace Engineering

WORK EXPERIENCE

ANSYS Inc. - San Diego, CA Jan 2019 - Apr 2019

Ph.D. Student Intern, Chemkin Department

- Wrote Python scripts for parsing, syntax checking, validation and format conversion of input files for ANSYS Chemkin. Developed scripts for easily preparing input files for more than 50 heterogeneous reactions
- Reviewed experiments and numerical simulations for the chemical vapor deposition of SiC. Implemented and tested two different surface reaction mechanisms of SiC production from silane and propane in ANSYS Chemkin

Purdue University - West Lafayette, IN

Sep 2015 - May 2016

Teaching Assistant

- Lectured, held office hours and drafted homework assignments for undergraduate-level class in aerodynamics

RESEARCH EXPERIENCE

Numerical simulation of radio-frequency discharge Aug 2019-Aug 2020

Modeled the capacitively charged plasma generated between electrodes driven by RF power, and prepared the framework for coupled plasma and electromagnetic wave simulation

- Modeled low pressure, room temperature, radio-frequency Air, Argon and Neon discharge in COMSOL Multiphysics. Studied the neutral chemistry for Air discharge, water contamination for Argon discharge and the applicability of drift diffusion approximation for submillimeter Neon discharge.
- Simulated Argon and Air plasma experiments. Results were compared with experimental data and used for the improvement of the experimental setup.
- Setup the framework in COMSOL Multiphysics for coupled plasma and electromagnetic wave simulation of tunable network driven by plasma cell

Classical impulsive nonequilibrium reaction model

Jan 2017-Aug 2020

Developed physics-based nonempirical thermal nonequilibrium chemical reaction model and applied the model in CFD and direct simulation Monte Carlo (DSMC) method

- Assessed and improved classical impulsive model for thermal nonequilibrium dissociation in CFD. Implemented the model in 1D shock simulator.
- Developed and validated a new DSMC dissociation reaction model, which predicts reaction rates in excellent agreement with latest first-principle calculations. Proposed physics-based collision model and recombination model for DSMC. Implemented the model in Sandia's DSMC simulator.

Ab-initio state-specific modeling of N₂-O system Jan 2015 - Aug 2020

Studied the chemical reactions and energy transfer mechanisms between different internal modes for N₂-O system in high-temperature thermochemical nonequilibrium condition, and improved the modeling of the system for numerical simulations

Chemical physics 1) Developed scalable MATLAB and object-oriented FORTRAN code for the simulation of millions of three-body molecular collisions; 2) Calculated thermal nonequilibrium reaction rates, energy relaxation cross sections and transport properties for N₂-O system. Reduced the uncertainties of the nonequilibrium rates by two orders of magnitudes; 3) Developed an approach to formulate state-specific models based on the maximum entropy principle. The models can reduce thousands of possible transition cross sections to models with few parameters.

Aerodynamics 1) Implemented the models in CFD (Eilmer 3, coded in C++) and direct simulation Monte Carlo method (DS1V, coded in FORTRAN) for high-fidelity simulation of hypersonic nonequilibrium flow; 2) Benchmark test of the models.

MD simulation of liquid water under laser field May 2015-Aug 2015

Implemented polarizable water model in LAMMPS Molecular Dynamics (MD) code (coded in C++) to account for polarization effect. Studied the influence of laser field intensity and frequency to molecular alignment by MD simulations.

BOOK CHAPTER AND JOURNAL PAPERS

1. S. O. Macheret, **H. Luo**, and A. A. Alexeenko, “Non-empirical analytical model of non-equilibrium dissociation in high-temperature air” , in *Hypersonic meteoroid entry physics*, edited by G. Colonna, M. Capitelli, and A. Laricchiuta, IOP Series in Plasma Physics (2019) Chap. 17, 17-1 to 17–14.
2. **H. Luo**, A. A. Alexeenko, and S. O. Macheret, “Development of an impulsive model of dissociation in direct simulation monte carlo” , *Physics of Fluids* **31**, 087105 (2019).
3. **H. Luo**, A. A. Alexeenko, and S. O. Macheret, “Assessment of classical impulsive models of dissociation in thermochemical nonequilibrium” , *Journal of Thermophysics and Heat Transfer*, 1–8 (2018).
4. **H. Luo**, I. B. Sebastião, A. A. Alexeenko, and S. O. Macheret, “Classical impulsive model for dissociation of diatomic molecules in direct simulation monte carlo” , *Physical Review Fluids*, **3**, 113401, (2018).
5. **H. Luo**, M. F. Kulakhmetov, and A. A. Alexeenko, “Ab initio state-specific N_2+O dissociation and exchange modeling for molecular simulations” , *Journal of Chemical Physics*, **146**, 074303 (2017).

CONFERENCE PAPERS

1. **H. Luo**, A. Alexeenko, and S. O. Macheret, “Verification and improvement of impulsive model for dissociation of di- atomic molecules in DSMC” , in AIAA scitech 2020 forum (Jan. 2020).
2. **H. Luo**, A. Alexeenko, and S. O. Macheret, “Classical impulsive models of nonequilibrium dissociation for CFD and DSMC” , in AIAA scitech 2019 forum (Jan. 2019).

3. **H. Luo**, S. O. Macheret, and A. A. Alexeenko, “First-Principle Calculations of Collision Integrals for N₂-O System” , in 12th AIAA/ASME Joint Thermophysics and Heat Transfer Conference (June 2018).
4. **H. Luo**, S. O. Macheret, and A. A. Alexeenko, “Quasi-classical trajectory studies of N₂+O collisions: trajectory patterns and long-lived configurations” , in 47th AIAA Thermophysics Conference (June 2017).
5. I. B. Sebastião, **H. Luo**, M. F. Kulakhmetov, and A. A. Alexeenko, “DSMC implementation of compact state-specific N₂+O dissociation and exchange models” , in 55th AIAA Aerospace Sciences Meeting (Jan. 2017).

ADDITIONAL INFORMATION

Languages	Chinese (native), English (fluent)
Programming Language	Proficient: FORTRAN, MATLAB, Python; Experienced: C++ Used in the past: Lua, Javascript
Software	CATIA, Chemkin, COMSOL Multiphysics, Fluent, Mathematica, MATLAB, Tecplot, Eilmer3, LAMMPS, SPARTA, US3D
Supercomputing	OpenMP and MPI
Interdisciplinary coursework	Plasmas and Electric Discharges, Computational Quantum Chemistry, Optimization Methods for Systems and Control, Radiative Heat Transfer